

AN ABSTRACT OF THE THESIS OF

Phong T. Nguyen for the degree of Doctor of Philosophy
presented June 21, 1995. Title: Chemistry and
Characterization of Vanadium Phosphate Catalyst.

Abstract approved : Redacted for Privacy
Arthur W. Sleight

The aim of this research was to develop a better understanding for the chemistry of the vanadyl pyrophosphate catalyst $(VO)_2P_2O_7$. This catalyst is unique in its ability to convert n-butane to maleic anhydride, a precursor to many commercial products such as LycraTM. Catalyst preparation, characterization, activity, crystal structure, and defects were all investigated.

An improved synthesis of $(VO)_2P_2O_7$ was developed. This involves removal of organic residue from the $V_2P_2O_9 \cdot 2H_2O$ precursor coupled with control of the oxygen fugacity during the topotactic dehydration of $V_2P_2O_9 \cdot 2H_2O$ to $(VO)_2P_2O_7$. The range of oxygen fugacities under which $(VO)_2P_2O_7$ is stable was determined over the temperature range 580°C to 790°C. A new mixed valent $V^{3+} - V^{4+}$ phosphate was discovered while investigating the effect of low oxygen fugacity.

Single crystals of $(VO)_2P_2O_7$ devoid of streaking effects in their X-ray diffraction patterns were prepared for the

first time. This enabled the first accurate structure determination of this compound.

The defects always prominent in $(VO)_2P_2O_7$ catalysts were successfully modeled for the first time. These can be represented as extended faults perpendicular to both the a and c crystallographic axes of $(VO)_2P_2O_7$. These defects offer an explanation of the well-known nonstoichiometry of $(VO)_2P_2O_7$ prepared to be an effective catalyst. When these defects intersect the surface, they may produce the unique active sites for selective oxidation of n-butane to maleic anhydride. The shape and position of $(VO)_2P_2O_7$ diffraction peaks were found to correlate with catalyst performance.

Chemistry and Characterization of
Vanadyl Phosphate Catalysts

by

Phong T. Nguyen

A THESIS

submitted to

Oregon State University

in partial fulfillment of
the requirements for the degree of

Doctor of Philosophy

Completed June 21, 1995

Commencement June 1996

Doctor of Philosophy thesis of Phong T. Nguyen presented on
June 21, 1995.

APPROVED :

Redacted for Privacy

Major Professor, representing Chemistry _____

Redacted for Privacy

Head of Department of Chemistry _____

Redacted for Privacy

Dean of Graduate School _____

I understand that my thesis will become part of the permanent collection of Oregon State University libraries. My signature below authorizes release of my thesis to any reader upon request.

Redacted for Privacy

Phong T. Nguyen, Author

ACKNOWLEDGMENT

It is with a great pleasure and honor to say thank you to my major advisor, Professor Arthur W. Sleight. His guidance and relentless pursuit for a extensive yet simple solutions to basic chemical problems has inspired me to push the limits to resolve not only scientific questions but common everyday problems as well. For this I can only say thank you for all his help, motivation, and especially kindness.

To all the friends that I have had the pleasure to meet and share my trials and tribulations: Vincent Korthuis, Nazy Khosrovani, Sasi Kodialam, Pat Woodward, Rolf-Dieter Hoffmann, Jinfan Huang, Ruiping Wang, Laura King, Richard Mackay, Mark Kennard, John Evans, and Mary Thundathil, THANK YOU for all your help. I wish you all the best.

Finally I want to thank my mother for all her help and her efforts to keep my mind focussed. Without her, it would be impossible for me to complete this project and education.

TABLE OF CONTENTS

1. Introduction to Research.....	1
1.1 Introduction	2
1.2 References	20
2. Single Crystal Analysis of $(VO)_2P_2O_7$	22
2.1 Introduction	22
2.2 Experimental	24
2.3 Discussion	40
2.4 Conclusion	54
2.5 References	55
3. Modeling of Extended Defects in Vanadium Phosphate Catalyst.....	56
3.1 Introduction	56
3.2 Experimental	57
3.3 Results	59
3.4 Discussion	66
3.5 Conclusions	74
3.6 References	75
4. Stability Field for $(VO)_2P_2O_7$	77
4.1 Introduction	77
4.2 Experimental	78
4.3 Results and Disucssion	82
4.4 Conclusions	96
4.5 References	98

TABLE OF CONTENTS (Continued)

5. Analysis of Diffraction Patterns on Real VPO Catalysts .	100
5.1 Introduction	100
5.2 Experimental	101
5.3 Results	104
5.4 Conclusion	119
5.5 References	121
Bibliography	122

LIST OF FIGURES

<u>Figure</u>		<u>Page</u>
1.1	Breakdown of some commercially important chemicals produced from maleic anhydride	4
1.2	Schematic representation of the effects in cell edges and bond distances for an edged shared octahedra consisting of vanadium and oxygen atoms	8
1.3	Crystal structure of $V_2P_2O_9 \cdot 2H_2O$	9
1.4	Structure of $V_2P_2O_9$	10
1.5	Crystal structure of β - VPO_5 looking down the b -axis	11
1.6	Crystal structure of β - VPO_5	12
1.7	Crystal structure of VPO_4	13
2.1	Crystal structure of vanadyl pyrophosphate viewed perpendicular to the (100) face	44
2.2	View of $(VO)_2P_2O_7$ looking approximately down the (001) face	45
2.3	Difference Fourier electron density map for $Pca2_1$ space group refinement	46
2.4	Average bond lengths and bond angles for an edge-shared vanadium moiety	50
2.5	Difference Fourier electron density map for $P2_1$ space group refinement	51
3.1	X-ray powder diffraction patterns and DIFFaX simulations	61

LIST OF FIGURES (Continued)

<u>Figure</u>		<u>Page</u>
3.2	Crystal structure of $V_2P_2O_9 \cdot 2H_2O$ and $(VO)_2P_2O_7$	63
3.3	Definition of faults used in DIFFaX simulations ..	64
4.1	Schematic design of fugacity probe	80
4.2	Schematic of fugacity furnace	81
4.3	Plot of stability region for VPO	83
4.4	X-ray powder pattern of a mixture of VPO and β -VPO ₅	84
4.5	X-ray powder pattern of VPO, VPO ₄ , and unknown phase	87
4.6	X-ray powder pattern for VPO prepared at the same oxygen fugacity but different temperatures	90
5.1	X-ray powder patterns of $V_2P_2O_9 \cdot 2H_2O$ after 12 hours of reflux with benzyl alcohol	108
5.2	How strain effects alter the appearance and position of the diffraction peak	109
5.3	X-ray powder patterns of VPO	112
5.4	How lattice constants varies as a function of time in laboratory reactor for spent catalysts ...	115
5.5	The comparison between laboratory reactor samples and actual plant samples of ctalysts	116
5.6	Compilation of correct a-lattice constant data from catalyst supplied by DuPont and samples prepared at OSU	117

LIST OF TABLES

<u>Table</u>	<u>Page</u>
2.1	Crystal Data and Intensity Collection for Pca2 ₁ Space Group 26
2.2	Crystal Data and Intensity Collection for P2 ₁ Space Group 27
2.3	Atomic and Isotropic Thermal Parameters for Pca2 ₁ Space Group 28
2.4	Atomic and Isotropic Thermal Parameters for P2 ₁ Space Group 29
2.5	Anisotropic Thermal Parameters ($\times 10^{-4}\text{\AA}$) for Pca2 ₁ Space group 30
2.6	Anisotropic Thermal Parameters ($\times 10^{-4}\text{\AA}$) for P2 ₁ Space group 31
2.7	Bond Distances (\AA) for Pca2 ₁ Space Group 32
2.8	Interatomic Angles ($^{\circ}$) for Pca2 ₁ Space Group 33
2.9	Bond Angles ($^{\circ}$) for P2 ₁ Space Group 35
2.10	Bond Distances (\AA) for P2 ₁ Space Group 38
2.11	F(obs) and F(calc) for reflections not allowed in Pca2 ₁ 52
3.1	DIFFaX Simulation Data 58
4.1	Data for unknown V(III)V(IV) Phase 86
4.2	Data for samples prepared at different temperatures and constant oxygen fugacity 93

LIST OF TABLES (Continued)

<u>Figure</u>		<u>Page</u>
4.3	Data for samples prepared from low to high oxygen fugacity	94
4.4	Data for samples prepared from high to low oxygen fugacity	94
5.1	$V_2P_2O_9 \cdot 2H_2O$ Data	106
5.2	VPO Data	113
5.3	Data for DuPont VPO Samples	114

Chemistry and Characterization of Vanadium Phosphate Catalyst

Chapter 1

Introduction to Research

1.1 Introduction

Maleic anhydride is an important intermediate to several large scale industrial processes. The demand for this important chemical, primarily used in the manufacturing of unsaturated polyester resins, agriculture chemicals, food additives, lubricating oil additives, and pharmaceuticals is increasing significantly in the 1990's. Among the more significant commercial uses is the conversion to ethylene glycol, a precursor to unsaturated polyesters, commonly referred to as Spandex™ or Lycra™, Figure 1.1. Prior to 1970, large scale production of maleic anhydride was attained by the traditional fixed bed oxidation of benzene over a V_2O_5 - MoO_3 catalyst. Recently, all US production has shifted away from the established

method because of the cost and the environmental hazard associated with the use of benzene.

Using *n*-butane as a feedstock is advantageous because it is cheaper and nontoxic, and because *n*-butane oxidation produces maleic anhydride with fewer problematic by-products. The main by-products are carbon dioxide, carbon monoxide, and water. However, the maleic anhydride yield from *n*-butane is lower than that of the benzene route in typical commercial fixed bed reactors. In spite of the lower yields, low *n*-butane prices makes the *C4* route economically favored.

All catalysts used industrially for the production of maleic anhydride from butane are vanadium-phosphorous based oxides (VPO). The catalytic reaction is very complex and involves the abstraction of 8 hydrogen atoms and 14 electrons along with an insertion of three oxygens to complete the reaction.



It is a unique catalyst because it is the only compound to selectively oxidize *C4* hydrocarbons,

specifically *n*-butane, to maleic anhydride. It is also the only example of an industrially practiced selective oxidation reaction involving alkane activation.

To date, the molar selectivities for fixed-bed production of maleic anhydride from butane are around 70% under normal conditions (1). Fluid bed butane based reactors have been given serious considerations; however, the improvement is minimal. Also, the inherent problems with attrition of vanadium phosphorous oxide catalysts needs to be overcome before the fluid bed process will become economically preferred. Dupont recently introduced a recirculating solids reactor which separates the butane oxidation step from the catalyst reaction step which may be the most economically favorable route for maleic anhydride production in the future. This process operates at higher selectivity than those observed in fixed or fluid bed systems. The catalyst is protected from attrition with an amorphous silica shell in order to prolong the lifetime of the catalyst. Typically, a hydrated precursor is mixed with 10 weight percent polysilicic acid; then the slurry is spray dried into a chamber maintained at 250°C to create spherical shaped balls of catalyst roughly 45-150µm in size (2).

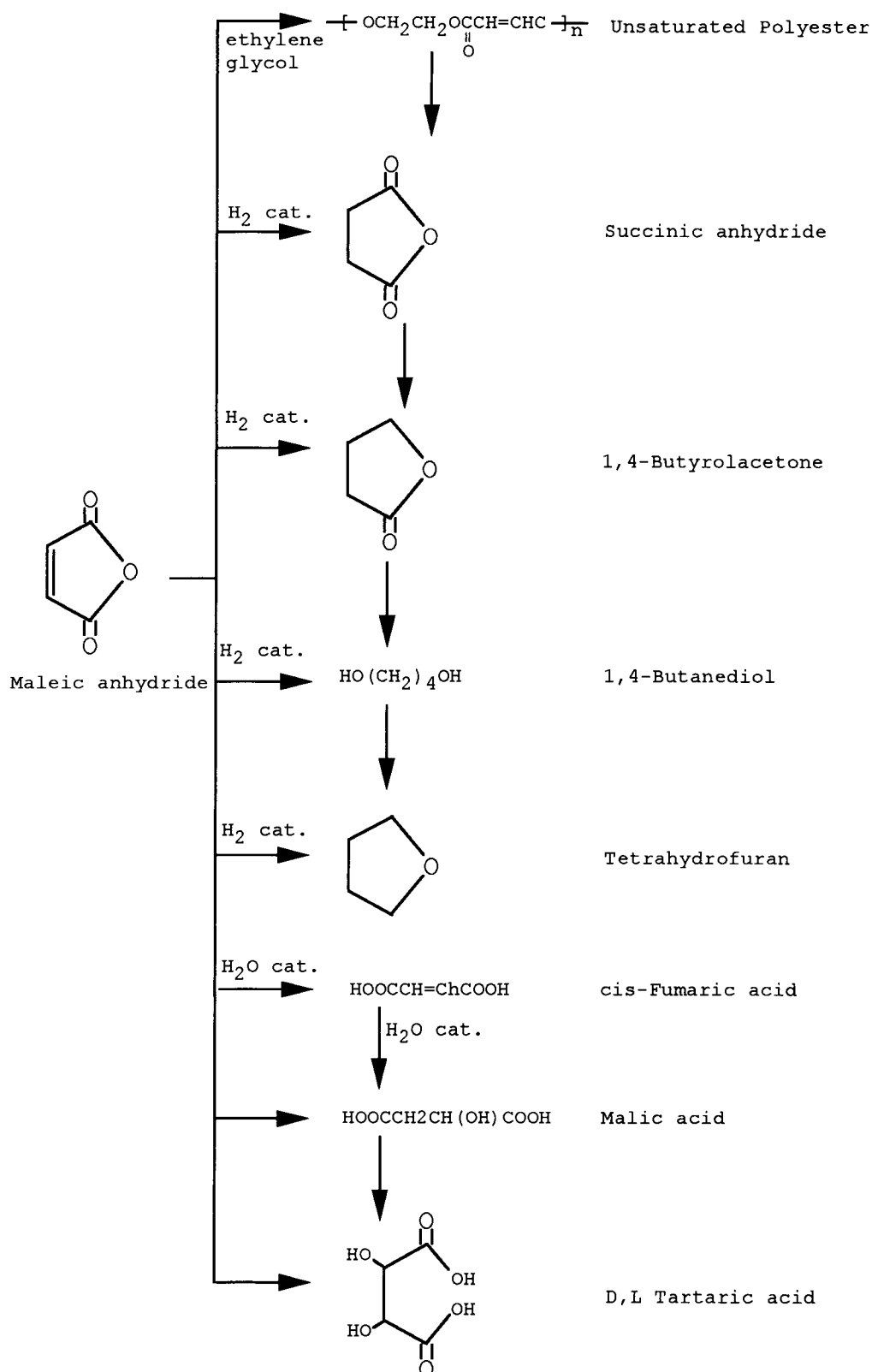


Figure 1.1. Breakdown of some commercially important chemical compounds from maleic anhydride

The preparation of vanadium phosphate catalysts, or VPO, can involve a number of crystalline vanadium(+3), vanadium(+4), and vanadium (+5) phases, and this has led to some confusion in literature as to the nature of the active phase.

The best catalysts formed are always prepared from a hydrated precursor, $V_2P_2O_9 \cdot xH_2O$. There has been much speculation, but the need for this synthesis route is still uncertain. Depending on synthesis parameters the degree of hydration can vary for the precursor ($V_2P_2O_9 \cdot xH_2O$ where $0.5 \leq x \leq 4.0$). The most important phase in this group $V_2P_2O_9 \cdot 2H_2O$ because it is the predominant product in the commercial synthesis route. The crystal structure of $V_2P_2O_9 \cdot 2H_2O$, which crystallizes in the orthorhombic space group $Pmmn$, can be best described as vanadium hydrogen phosphate layers consisting of face-sharing vanadium octahedra with a capping water molecule surrounded by corner shared phosphate tetrahedra, Figure 1.3. Although each vanadium atom has one free electron available for bonding, no V-V bond exists within this compound.

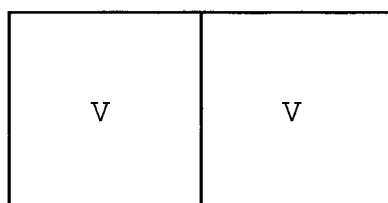
In an ideal octahedron consisting of vanadium(IV) and oxygen with a V-O distance of 1.94Å, the distances between

oxygen atoms on the edges is about 2.75Å. However, when octahedra share edges or faces, these distances are expected to change significantly, as shown schematically in Figure 1.2 for octahedra sharing an edge. If there is metal-metal bonding across a shared edge or face, then the vanadium atoms will displace toward the shared edge or face and the O-O distances across the common edge or face would be greater than 2.75Å. However, if there is no metal-metal bonding then the exact opposite would be true, i.e. the vanadium atoms would be displaced away from each other and the O-O distances across the common edge or face would be less than 2.75Å. In $V_2P_2O_9 \cdot 2H_2O$ the vanadium atoms of the face shared octahedra pair have moved away from each other and the O-O distance across the common edge is 2.57Å, suggesting a non-bonding configuration for the metal atoms. Furthermore, a V-V distance of about 2.6Å is required for the presence of a V-V single bond (18,19), which is considerably less than the observed value of 3.09Å.

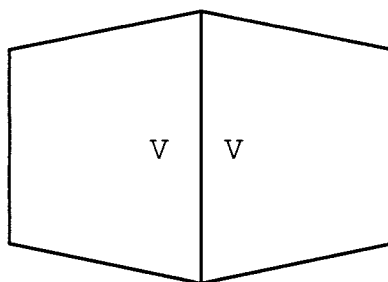
The remaining oxygens of each octahedron are corner shared with phosphate tetrahedra. These tetrahedra are oriented with a pseudo threefold axis perpendicular to the layer stacking direction. Only the basal oxygen atoms of the tetrahedra are involved in bonding with vanadium. The

apical oxygen is bound to hydrogen atoms. Each hydrogen atom of a shared water molecule is hydrogen bonded to an apical phosphate oxygen atom in the adjacent layer. Also, the covalently bonded hydrogen atoms on these apical oxygen atoms are hydrogen bonded to vanadyl oxygen atoms of a neighboring layer. These are layered materials and the incorporation of extra water as well as organic molecules between the sheets has been shown to occur (3,4).

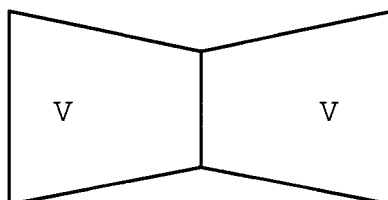
The active phase in butane oxidation is believed to be $(VO)_2P_2O_7$, the crystal structure of which is very similar to the hydrated precursor $V_2P_2O_9 \cdot 2H_2O$. The $(VO)_2P_2O_7$ structure comprises sheets of edge-shared vanadium pseudo-octahedra with neighboring pyrophosphate P_2O_7 groups. It is mainly these pyrophosphate units that unite two adjacent layers to complete the three-dimensional framework of the crystal structure, Figure 1.4. There are one short and one long vanadium-oxygen bond per vanadium atom, i.e., $V=O$ (1.56\AA) and $V \cdots O$ (2.6\AA), that runs along the a axis. Analogous to the precursor, there are no V-V bonds (5,6,7). The O-O distance across the common edge is 2.68\AA and the V-V distance is 3.23\AA . This implies that the vanadium metal atoms are pushing against one another, thus decreasing the



(a)



(b)



(c)

Figure 1.2. Schematic representation of the effects in cell edges and bond distances for an edge shared octahdra consisting of vanadium and oxygen atoms. a) an ideal unit b) V-V bonding and c) V-V non-bonding. The corners represents oxygen atoms which are not displayed for clarity.

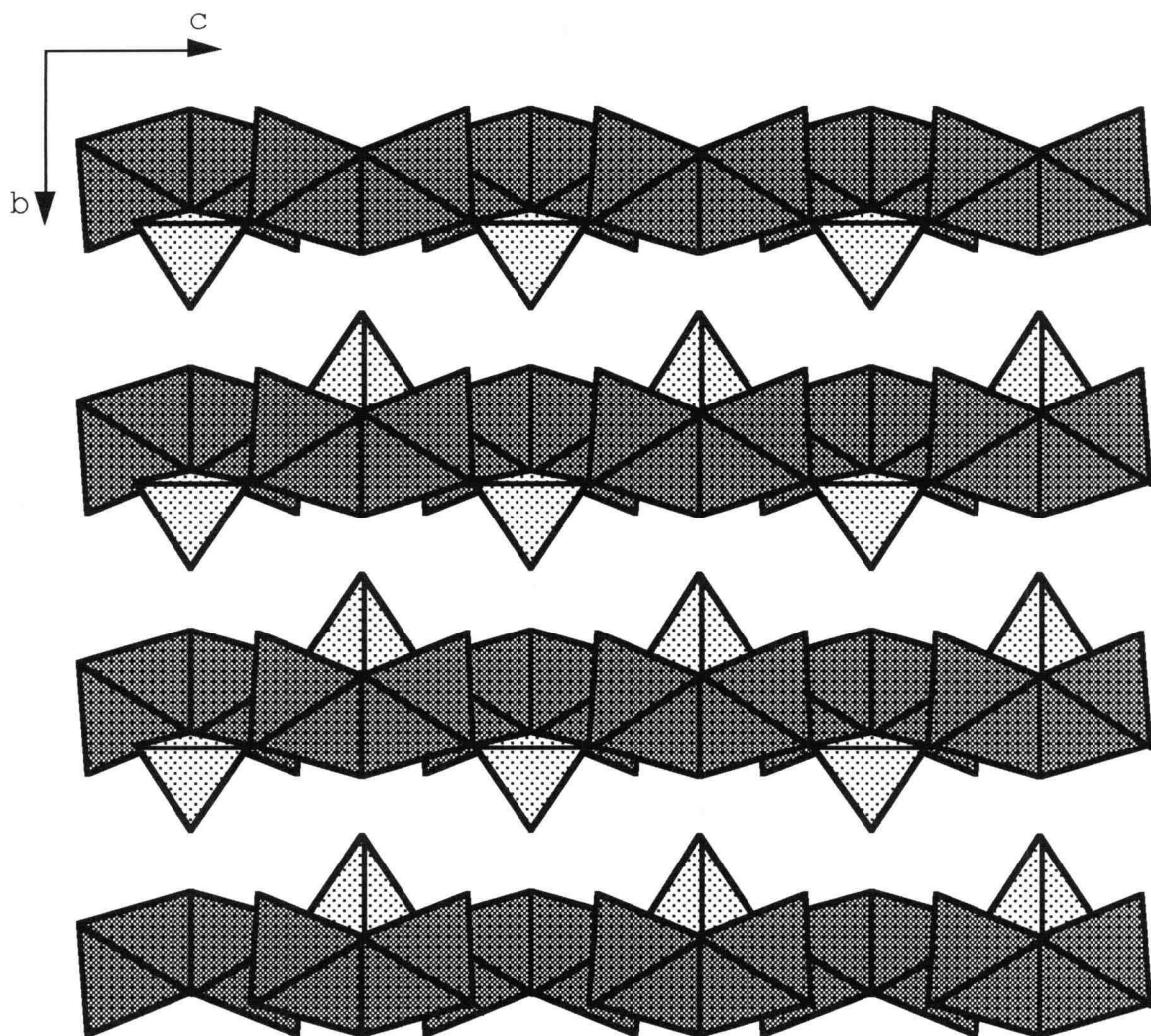


Figure 1.3. Crystal structure of $V_2P_2O_9 \cdot 2H_2O$. Sheets of face-sharing vanadium octahedra are corner sharing to phosphate tetrahedra. The gap between the sheets is approximately 2Å.

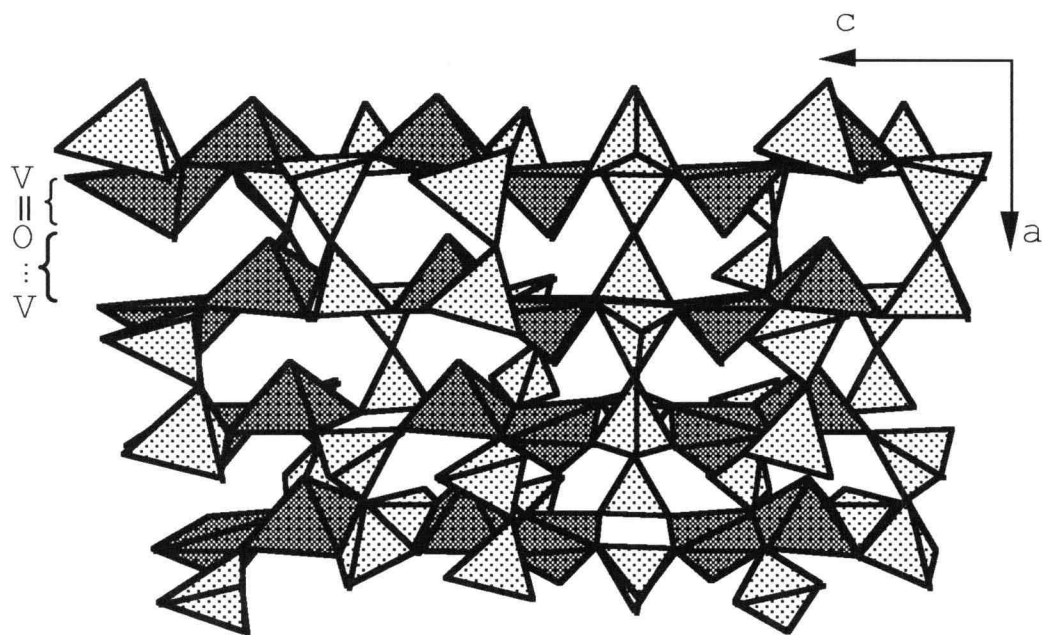


Figure 1.4. Structure of $V_2P_2O_9$. Sheets of edge sharing vanadium octahedra are corner sharing to pyrophosphate groups. The short vanadyl bonds are arranged in a trans position within each edge sharing dimer. The equatorial vanadium-to-oxygen bond lengths are approximately 2\AA .

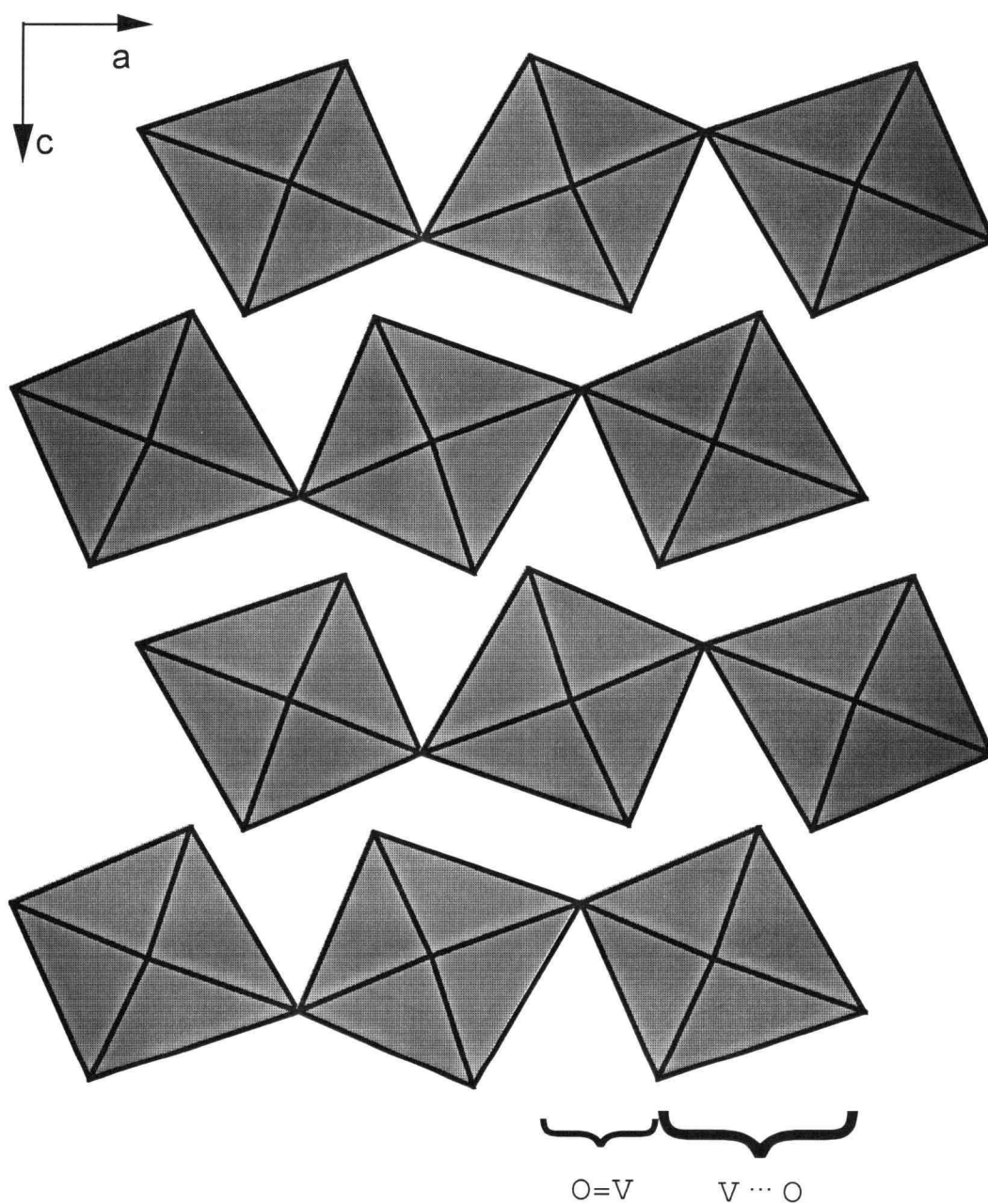


Figure 1.5. Crystal structure of β -VPO₅ looking down the b-axis. Distorted corner sharing vanadium octahedra are forming chains that runs parallel to the a-axis. The phosphorous tetrahedra are omitted for clarity. The short vanadium-oxygen bond length is 1.56Å and the long vanadium oxygen bond length is 2.56Å. The equatorial vanadium oxygen bonds are approximately 2Å in length.

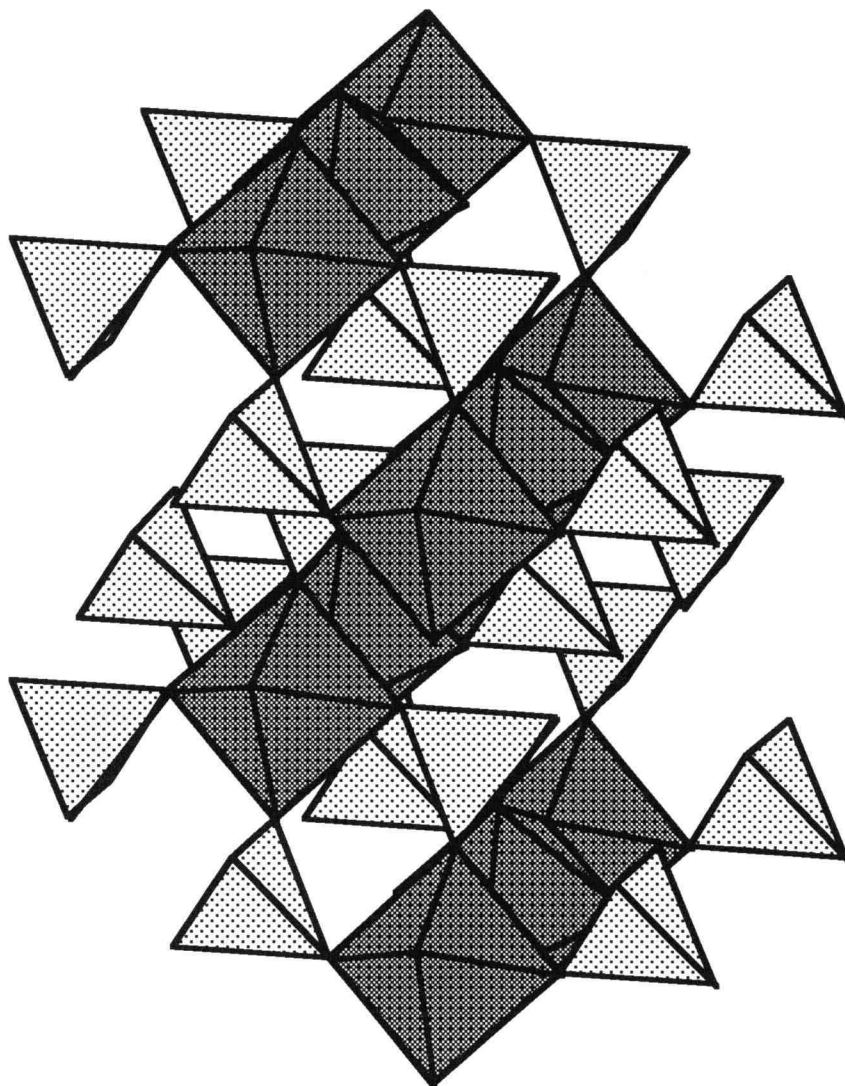


Figure 1.6. Crystal structure of β -VPO₅. Chains of corner sharing vanadium octahedra are projected to be coming in and out of the plane. Phosphorous tetrahedra are sharing corners to three different chains.

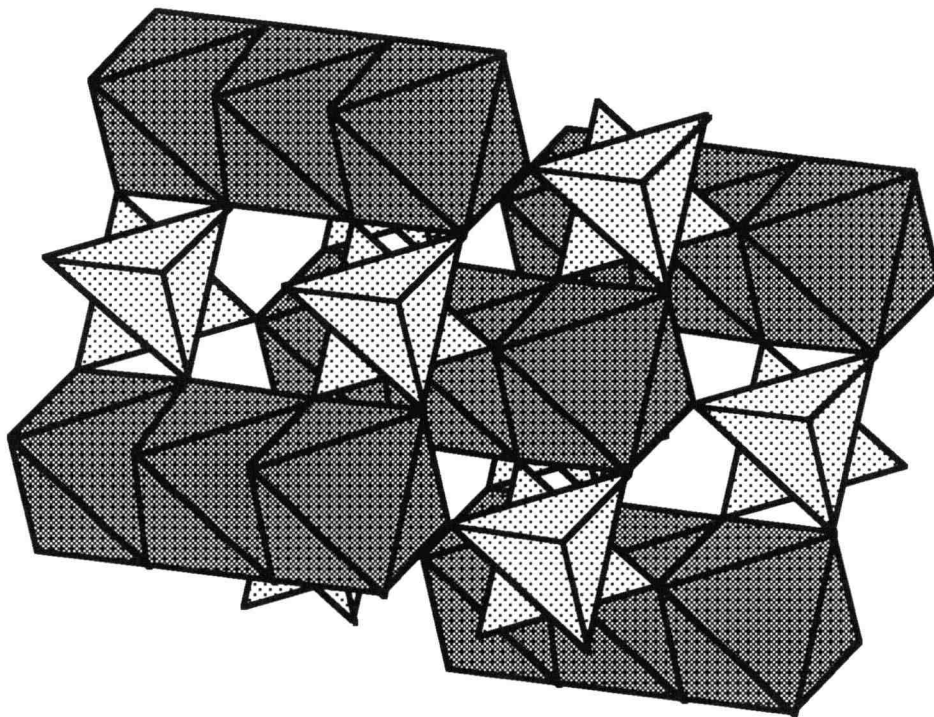


Figure 1.7. Crystal structure of VPO_4 . The structure is composed of edge sharing vanadium octahedra forming chains that propagate parallel to the c -axis. Phosphorous tetrahedra are corner sharing to the vanadium chains to complete the three-dimensional network.

O-O distance across the common edge, Figure 1.2.

Furthermore, existence of a V-V single bond requires at the very minimum a V-V bond length of 2.6Å (18,19).

Five known VOPO_4 or VPO_5 polymorphs are reported in the literature, the only difference between the structures being the orientation and symmetry of the polyhedra within the crystal lattice. $\beta\text{-VPO}_5$ is the most important compound in this family because it is the most common phase observed and because it is structurally related to $(\text{VO})_2\text{P}_2\text{O}_7$. $\beta\text{-VPO}_5$ crystallizes in the orthorhombic space group Pnma (8).

Similar to $(\text{VO})_2\text{P}_2\text{O}_7$, the crystal structure of $\beta\text{-VPO}_5$ has alternating short and long vanadium-oxygen bonds within the VO_6 distorted octahedra, Figure 1.5. The structure consists of sheets of corner sharing octahedra running parallel to the *a* axis. The short and long vanadium-oxygen bonds lie at small angles to the chain direction. The PO_4 tetrahedra link the sheets by sharing their oxygen atoms with four separate VO_6 groups in three separate chains to complete the three dimensional network, Figure 1.6.

Unlike the other three structures, the crystal structure of VPO_4 , which crystallizes in the Cmc₂m space group, is composed of edge sharing vanadium octahedra which form chains that propagate in the *c*-direction (9). The

chains are linked to one another by sharing corners with PO_4 tetrahedra to complete the three-dimensional network, Figure 1.7.

As mentioned earlier, there are many synthesis variables that affect the solid state chemistry leading to the active VPO catalyst. The performance of the catalyst is highly dependent on the details of the synthesis. Both organic solvent and aqueous solvent preparation can give catalysts with differing degree of crystallinity and defect concentration. The P:V ratio used in synthesis and found in the final catalysts is variable and has been the subject of numerous publications and debate. The P:V ratios used in synthesis are in the range 0.8 to 2.1, however, industrial catalysts always have a P:V ratio greater than one, usually 1.1 to 1.2. When excess phosphorous is present, the catalysts have been shown to be resistant to oxidation. Most of the phosphorous used during synthesis in excess over P:V of 1:1 remains in solution. However, good catalysts have a slight excess of phosphorous with respect to 1:1 and at least some of this is apparently concentrated on the catalyst surface (10,11,12).

The best catalysts are prepared by a dehydration of the precursor, $\text{V}_2\text{P}_2\text{O}_9 \cdot x\text{H}_2\text{O}$. A proposed mechanism for this

transformation taking into consideration structure and energy requirements has been proposed. This involves first the removal of the bridging water molecule with movement of the resulting square pyramids to a position where the vanadyl groups are parallel. Half of the apical oxygen atoms are then shifted giving rise to the edge-shared pseudo-octahedral arrangement where the octahedral dimers have vanadyl bonds pointing in opposite or *trans* directions relative to one another. After a proton migration, half of the phosphate tetrahedra lose an apical oxygen atom in the form of a water molecule. These unsaturated PO_3 units invert and interact with PO_4 tetrahedra above or below to form pyrophosphate groups. This mechanism leaves all vanadium-oxygen-phosphorous bonds intact and involves primarily the breaking of very weak V-OH_2 and P-OH bonds. Although a major structural change occurs on the atomic scale, there are no major differences in particle morphology and topology as observed in SEM photographs taken before and after the structural conversion. It is for this reason that some have deemed this transformation between the two phases to be a topotactic transformation (13,14).

There are many unanswered questions and conflicting results concerning the nature of the active sites in this commercially important catalyst. In some catalysts, the active sites have been shown to be where point or planar defects are known to occur (20,21), while in others there are many sites responsible for the catalytic conversion. In the selective reduction of acetic acid to acetaldehyde over iron oxide surfaces, it is believed that the catalytic reaction occurs on the oxygen vacancy sites on the surface of the catalyst (15). In the commercial oxidation of methanol to formaldehyde, the best catalyst is a mixture of $\text{Fe}_2(\text{MoO}_4)_3$ and MoO_3 . However, the catalytic reaction was shown to take place only on Mo centers (16).

The X-ray powder patterns that are presented for the active and non-active preparations of VPO are all very similar to one another with respect to line width, peak position, and peak intensity or area. It is very difficult to distinguish between the catalytically suitable and non-suitable phases just from examination of the diffraction data alone. There are no marked differences perceptible even after careful consideration of all known variables like line profile, peak shifts, or area.

For samples of VPO that are made at relatively low temperatures, less than 700°C, there is an unusual behavior in the observed powder patterns, specifically for peaks involving an h or l odd component. These peaks are extremely broad when compared to other peaks within the same two-theta region. Such broadening cannot be attributed to particle size or strain effects, but might be a characteristic of certain extended defects. To date, no description has been presented on what these defects might be or how they might relate to catalytic performance.

The crystal structure of the precursor phases has been well characterized, and there is little doubt as to what phase is present. However the three reported single crystal structures for the catalyst phase ($V_2P_2O_9$) do not describe the crystal structure adequately. The best solution reported had the vanadium atomic positions split between two crystallographic sites. This was to account for unusual observations in difference Fourier maps. Excess electron density was observed to exist above and below each vanadium atom. The solution to remove this effect was to split the vanadium atoms and assign 50% occupancy to each site (6).

Finally the redox chemistry between vanadium(iv) and vanadium(v) or vanadium(iv) and vanadium(iii) phosphates is poorly understood. There has been evidence of intermediate phases between vanadium four and vanadium five phosphates identified as $VPO_{4.75}$ where vanadium is both in the +4 and +5 oxidation state concurrently (12,17). However, questions still remain as to the route to make this phase as well as the region of stability and if this phase truly exists at all. Also, there is no evidence of studies performed in vanadium +4 and vanadium +3 phases in this system to precisely determine where the transition between the two will occur.

In this study, we try to answer most of these perplexing questions. The study of phase stability was performed in an oxygen controlled furnace capable of pressure from as low as 10^{-11} to 1 atm of oxygen. The sensor was an yttria-stabilized zirconia cell operating at $1050^{\circ}C$ with pure oxygen acting as the reference gas. X-ray powder patterns were obtained from a Siemens D5000 powder diffractometer operating at room temperature. Analysis of powder diffractogram peak widths were performed with the DIFFaX (22), Warren-Averbach(23), and Williamson-Hall (24) methods.

1.2 References

1. G. Centi, F. Trifiro, J.R. Ebner, and V.M. Franchetti, *Chem. Rev.*, **88**, 55 (1988)
2. R.M. Contractor, H.E. Bergna, H.S. Horowitz, C.M. Blackstone, B. Malone, C.C. Toradi, B. Griffiths, U. Chowdhry, and A.W. Sleight, *Catalysis Today*, **1**, 49 (1987)
3. C.C. Toradi and J.C. Calabrese, *Inorg. Chem.*, **23**, 1308 (1984)
4. J.W. Johnson, D.C. Johnston, A.J. Jacobson, and J.F. Brody, *J. Am. Chem. Soc.*, **106**, 8123 (1984)
5. J.R. Ebner and M.R. Thompson, *Studies in Surface Science and Catalysis*, ed. R.K. Grasselli and A.W. Sleight, Elsevier (1992)
6. N.E. Middlemiss, doctoral dissertation, Dept. of Chemistry, McMaster Univer. Hamilton, Ontario, Canada (1978)
7. Y.E. Gorbunova and S.A. Linde, *Sov. Phys. Dokl.*, **24**, 138 (1979)
8. R. Gopal and C. Calvo, *Journal of Solid State Chemistry*, **5**, 432 (1972)
9. B.C. Frazer and P.J. Brown, *Physical Review*, **125**, 1283 (1962)
10. L.M. Cornaglia, C. Caspani, and E.A. Lombardo, *Applied Catalysis*, **74**, 15 (1991)
11. M.L. Granados, J.C. Conesa, and M.F. Garcia, *Journal of Catalysis*, **141**, 671 (1993)
12. E. Bordes and P. Courtine, *Journal of Catalysis*, **57**, 236 (1979)
13. H.S. Horowitz, C.M. Blackstone, A.W. Sleight, and G. Teufer, *Applied Catalysis*, **38**, 193 (1988)

14. E. Bordes and P. Courtine, *Journal of Solid State Chemistry*, **55**, 270 (1984)
15. E.J. Grootendorst, R. Pestman, R.M. Koster, and V. Ponec, *Journal of Catalysis*, **148**, 261 (1994)
16. A.W. Sleight, *Solid State Chemistry Compounds*, ed. A.K. Cheetham and P. Day, Oxford Univ. Press, 166-181 (1992)
17. I. Matsuura, A. Mori, and M. Yamazaki, *Chemistry Letters*, 1897-1900 (1987)
18. Cotton and Wilkinson, *Advance Inorganic Chemistry*, 5th Ed., Wiley and Sons Publishing, pp. 677-678, (1988)
19. T. B. Rauchfuss, et. Al., *J. Am. Chem. Soc.*, **105**, 6321 (1983)
20. L. Forni, C. Oliva, A.V. Vixhniakov, A.M. Ezerets, I.E. Mukovozov, F.P. Vatti, and V.N. Zukovskaja, *J. Catalysis*, **145**, 194-203, (1994)
21. S. De Rossi, M.L. Jacono, M. Gardini, and P. Porta, *J Catalysis*, **146**, 126-135 (1994)
22. J.M.M. Treacy, J.M. Newsam, and M.W. Deen, *Proc. R. Soc. Lond. A*, **433**, 499-520 (1991)
23. B.E. Warren, B.L. Averbach, *J. Applied Physics*, **21**, 595 (1950)
24. G. Williamson and W.H. Hall, *Acta Metall.*, **1**, 22 (1953)

Chapter 2

Single Crystal Analysis of $(VO)_2P_2O_7$

2.1 Introduction

There have been three independent structure determinations reported for $(VO)_2P_2O_7$ (1,2,3). The first solution reported was by Middlemess in his thesis presented in 1978 (2). The R-value was unusually high, 19.8%. A year later, in 1979, Linde and Gorbunova attempted to obtain an improved structure (1). Their solution still had many flaws and high residuals ($R = 8.1\%$ and $R_w = 9.1\%$) as well as atypically short bond lengths for both V and P, 1.55Å and 1.48Å respectively. To remove these discrepancies, Thompson and Ebner (3) undertook a venture to reevaluate the crystal solution in 1993. Their results were also peculiar because of observations of a disordered arrangement of the V atoms in the lattice and a variable color of their crystals.

Depending on the method of precursor preparation, Thompson and Ebner obtained either red-brown or emerald green crystals from the melt. Red-brown crystals were the

predominant product if an aqueous method was used to prepare the precursor $V_2P_2O_9 \cdot 2H_2O$, and emerald green crystals were the only product if the precursor was made with an organic solvent. A difference Fourier analysis using data from either crystal showed significant electron density peaks only around the V atoms. These peaks were on both sides of V along the direction parallel to the a-axis. The electron density was in a dumbbell shape approximate 0.65Å above and below the metal atom. By splitting the vanadium equally between these two positions, the investigators were able to obtain very good residuals, $R = 3.4\%$, $R_w = 3.5\%$ for the emerald green crystal and $R = 5.4\%$, $R_w = 5.6\%$ for red brown crystals. A model was presented to rationalize the difference in the apparent structure of the crystals, but no reasons were given for the differences in color.

In this study, we will give some possible explanations for the disorder that was observed by Ebner and Thompson and for the differences in the color of their crystals.

2.2 Experimental

Single phase powder of $(VO)_2P_2O_7$ was prepared by the method outlined in chapter 4. Approximately 5g of sample was pressed into a pellet approximately 10mm in diameter and placed into a Pt crucible. The sample was placed in an oxygen controlled furnace for crystal growth. The sample was first heated to 500°C rapidly followed by an ascent to 910°C at a rate of 50 degrees/hour where it was held constant for 15 hours. A slow descent to 890°C at a rate of 2 degrees/hour followed by another descent to 855°C at a rate of 4 degrees/hour was initiated. The oxygen fugacity was controlled between 0.001 atm and 0.003 atm of oxygen.

The crystals collected from the melt were all green in color for the sample prepared at the lower oxygen partial pressure, but as the oxygen partial pressure was increased, there was evidence of red-brown crystals appearing. If the oxygen partial pressure was raised above 0.003 atm, the sample would completely melt. Since VPO_5 melts near 815°C in air, the observation of melting for samples prepared at relatively high concentrations of oxygen can be explained by the presence of VPO_5 in the samples.

Very few crystals of the red-brown origin were available for analysis. Usually 5-10 crystals were found for one sample, and they were of very poor quality for single crystal determination. Only emerald green crystals were used in our analysis. A crystal of the dimensions 0.635mm x 0.5mm x 0.4375mm was mounted on a glass fiber and secured with a small amount of wax for single crystal determination. Zero-level precession photographs were taken at a current of 20A and 30kV with Mo K_{α} radiation. Titration experiments were done as described in chapter 5.

Single crystal data were collected on a Rigaku AFC6R diffractometer. The intensities of three standard reflections measured every 300 reflections throughout the data collection exhibited no significant excursions. Absorption corrections were performed with DIFABS software routine (11). The structure was solved and refined with programs from the TEXAN crystallographic software package (5). Three different space groups were investigated, Pc_{2m} , $Pca2_1$ and its subgroup $P2_1$ (7). The vanadium atoms were located by direct methods using SHELXS86 for all three space groups (6). The phosphorous and oxygen atoms were found in subsequent analysis of difference electron density maps. The collection parameters are given Table 2.1 and 2.2. Isotropic

Table 2.1

Crystal Data and Intensity collection for $Pca2_1$ Space Group

Empirical Formula	$(VO)_2P_2O_7$
Formula weight (g/mol)	307.82
Crystal system	Orthorhombic
Space Group	$Pca2_1$ (no. 29)
Lattice parameter from single crystal	
a (Å)	7.7276 (3)
b (Å)	9.5796 (5)
c (Å)	16.5885 (4)
V (Å ³)	1228.00 (1.09)
Z	4
Diffractometer	Rigaku AFC6R
Radiation	MoK α ($\lambda = 0.71069$ Å) Graphite-monochromated
Temperature	23°C
Maximum 2θ	70°
Data collected	-9<h<9, -12<k<12, -21<l<21
Scan speed (degrees/min)	16.0 in ω and 32.0 in 2θ
No. of unique data with $F_o^2 > 3\sigma (F_o^2)$	2320
Data/parameter ratio	16
R	0.041
R _w	0.052
R _{merge}	0.0645

Table 2.2

Crystal Data and Intensity collection for $P2_1$ Space Group

Empirical Formula	$(VO)_2P_2O_7$
Formula weight (g/mol)	307.82
Crystal system	Monoclinic
Space Group	$P2_1$ (no. 4)
Lattice parameter from single crystal	
a (Å)	7.7276 (3)
b (Å)	16.5885 (4)
c (Å)	9.5796 (5)
V (Å ³)	1228.00 (1.09)
β	89.975 (3)
Z	4
Diffractionmeter	Rigaku AFC6R
Radiation	MoK α ($\lambda = 0.71069$ Å) Graphite-monochromated
Temperature	23°C
Maximum 2θ	70°
Data collected	$-9 < h < 9$, $-21 < k < 21$, $-12 < l < 12$
Scan speed (degrees/min)	16.0 in ω and 32.0 in 2θ
No. of unique data with $F_o^2 > 3\sigma (F_o^2)$	4254
Data/parameter ratio	14.72
R	0.044
R_w	0.066
R_{merge}	0.038

Table 2.3

Atomic and Isotropic Thermal Parameters for Pca2₁ Space Group

Atom	x	y	z	Beq (Å ²)*
V1	0.2968 (1)	0.49077 (8)	0.0958	0.37 (4)
V2	0.2081 (1)	0.50197 (7)	-0.09439 (5)	0.29 (4)
V3	0.2061 (1)	-0.00028 (7)	-0.15475 (6)	0.38 (4)
V4	0.2084 (1)	-0.00165 (7)	0.15615 (5)	0.33 (4)
P1	0.2968 (2)	0.7924 (1)	-0.0004 (1)	0.27 (5)
P2	0.1967 (2)	0.2010 (1)	0.0006 (1)	0.37 (6)
P3	0.1902 (2)	0.7063 (1)	-0.2447 (1)	0.29 (5)
P4	0.3001 (2)	0.2908 (1)	-0.2437 (1)	0.36 (5)
O1	0.5005 (5)	0.5402 (4)	0.5924 (2)	0.73 (6)
O2	0.0029 (6)	0.5320 (3)	-0.0891 (2)	0.48 (5)
O3	0.0006 (7)	0.0121 (4)	-0.1582 (2)	0.66 (5)
O4	0.0013 (6)	0.0113 (3)	0.1596 (2)	0.71 (5)
O5	0.4959 (5)	0.8261 (4)	-0.0020 (2)	1.32 (6)
O6	0.4952 (4)	0.2869 (3)	-0.2155 (2)	0.64 (5)
O7	0.2996 (5)	0.6424 (4)	0.1728 (2)	0.85 (6)
O8	0.2098 (5)	0.3605 (4)	0.1761 (2)	0.76 (6)
O9	0.2786 (5)	0.6304 (4)	0.0007 (2)	0.57 (7)
O10	0.2224 (5)	0.3615 (4)	0.0019 (2)	0.68 (7)
O11	0.2857 (5)	0.6299 (3)	-0.1792 (2)	0.57 (6)
O12	0.1991 (5)	0.3567 (3)	-0.1769 (2)	0.51 (6)
O13	0.2646 (6)	0.1395 (3)	0.0772 (2)	0.83 (6)
O14	0.2234 (6)	-0.1467 (3)	0.0745 (2)	1.00 (6)
O15	0.2703 (6)	0.1387 (4)	-0.0755 (2)	0.75 (6)
O16	0.2215 (6)	-0.1524 (4)	-0.0773 (2)	0.87 (6)
O17	0.2494 (7)	0.1343 (3)	-0.2508 (2)	0.69 (6)
O18	0.2486 (7)	-0.1385 (3)	-0.2482 (2)	0.43 (6)

$$*Beq = (8\pi^2/3) \sum_i \sum_j U_{ij} a_i^* a_j^* a_i a_j$$

Table 2.4

Atomic and Isotropic Thermal Parameters for $P2_1$ Space Group

Atom	x	y	z	Beq (\AA^2) [*]
V1	0.2973 (2)	0.0958	0.4912 (1)	0.47 (5)
V1'	0.2039 (2)	0.5960 (1)	0.4909 (1)	0.36 (5)
V2	0.2087 (2)	-0.09442 (9)	0.5023 (1)	0.33 (5)
V2'	0.2923 (2)	0.4057 (1)	0.5017 (1)	0.25 (5)
V3	0.2055 (2)	-0.1548 (1)	-0.0005 (2)	0.45 (6)
V3'	0.2935 (2)	0.3453 (1)	-0.0002 (1)	0.43 (6)
V4	0.2081 (2)	0.1561 (1)	-0.0014 (1)	0.34 (5)
V4'	0.2914 (2)	0.65607 (7)	-0.0021 (1)	0.33 (5)
P1	0.2952 (3)	-0.0003 (1)	0.7924 (2)	0.3 (1)
P1'	0.2026 (4)	0.4997 (2)	0.7925 (2)	0.39 (8)
P2	0.1948 (3)	0.0005 (2)	0.2012 (2)	0.3 (1)
P2'	0.3031 (4)	0.5008 (1)	0.2012 (2)	0.24 (8)
P3	0.1920 (4)	-0.2447 (2)	0.7064 (2)	0.4 (1)
P3'	0.3106 (4)	0.2556 (1)	0.7061 (2)	0.37 (9)
P4	0.3020 (3)	-0.2436 (1)	0.2907 (2)	0.4 (1)
P4'	0.2008 (4)	0.2562 (1)	0.2906 (2)	0.27 (8)
O1	0.5014 (8)	0.5914 (3)	0.5399 (4)	0.59 (8)
O1'	-0.0024 (8)	0.0933 (3)	0.5397 (4)	0.76 (8)
O2	0.005 (1)	-0.0904 (3)	0.5313 (5)	0.8 (1)
O2'	0.496 (1)	0.4121 (3)	0.5320 (4)	0.41 (9)
O3	-0.001 (1)	-0.1597 (3)	0.0131 (6)	0.59 (8)
O3'	0.500 (1)	0.3435 (4)	0.0115 (7)	0.9 (1)
O4	-0.0002 (9)	0.1599 (3)	0.0125 (6)	0.67 (8)
O4'	0.500 (1)	0.6595 (3)	0.0108 (6)	0.88 (8)
O5	0.4975 (8)	-0.0014 (3)	0.8272 (6)	1.55 (9)
O5'	0.0044 (8)	0.4983 (3)	0.8252 (6)	1.41 (9)
O6	0.4960 (7)	-0.2162 (3)	0.2871 (4)	0.59 (7)
O6'	0.0066 (8)	0.2846 (3)	0.2862 (5)	0.79 (8)
O7	0.3007 (9)	0.1734 (3)	0.6421 (5)	1.0 (1)
O7'	0.2017 (8)	0.6734 (3)	0.6410 (5)	0.71 (9)
O8	0.2133 (8)	0.1761 (3)	0.3613 (5)	0.44 (8)
O8'	0.2943 (9)	0.6756 (3)	0.3600 (5)	0.9 (1)
O9	0.281 (1)	0.0010 (4)	0.6307 (6)	0.9 (1)
O9'	0.2200 (8)	0.5007 (3)	0.6300 (5)	0.3 (1)
O10	0.2221 (9)	0.0017 (4)	0.3639 (5)	0.4 (1)
O10'	0.276 (1)	0.5012 (4)	0.3619 (6)	0.7 (1)
O11	0.2860 (9)	-0.1795 (3)	0.6294 (6)	0.7 (1)
O11'	0.2117 (9)	0.3207 (3)	0.6287 (5)	0.6 (1)

Table 2.4 (continued)

O12	0.199(1)	-0.1772(3)	0.3578(5)	0.8(1)
O12'	0.298(1)	0.3230(3)	0.3572(5)	0.7(1)
O13	0.2659(9)	0.0775(3)	0.1395(5)	1.0(1)
O13'	0.2355(8)	0.5768(3)	0.1390(5)	0.67(9)
O14	0.2274(8)	0.0749(3)	-0.1455(5)	0.79(9)
O14'	0.2809(9)	0.5743(3)	-0.1465(5)	1.05(9)
O15	0.2727(8)	-0.0754(3)	0.1391(6)	0.6(1)
O15'	0.2329(9)	0.4247(3)	0.1390(6)	0.7(1)
O16	0.2234(9)	-0.0768(3)	-0.1513(5)	0.7(1)
O16'	0.2823(9)	0.4233(3)	-0.1514(6)	0.8(1)
O17	0.2510(8)	-0.2504(3)	0.1328(6)	0.3(1)
O17'	0.255(1)	0.2497(4)	0.1352(6)	0.8(1)
O18	0.2496(9)	-0.2482(4)	-0.1394(6)	0.6(1)
O18'	0.2535(9)	0.2517(4)	-0.1382(6)	0.5(1)

$$*Beq = (8\pi^2/3) \sum_i \sum_j U_{ij} a_i^* a_j^* a_i a_j$$

Table 2.5

Anisotropic Thermal Parameters ($\times 10^{-4}\text{\AA}$) for $Pca2_1$ Space Group

Atom	U11	U22	U33	U12	U13	U23
V1	69(7)	34(4)	39(4)	-8(4)	-5(4)	5(4)
V2	47(6)	21(4)	44(4)	-2(4)	14(4)	1(3)
V3	71(7)	43(5)	31(4)	2(3)	7(4)	10(4)
V4	71(6)	18(4)	38(4)	6(4)	14(4)	2(3)
P1	27(9)	25(4)	51(7)	5(5)	12(6)	15(4)
P2	6(1)	20(5)	59(7)	8(5)	-15(6)	-4(4)
P3	53(9)	16(4)	42(7)	-2(5)	-16(5)	7(4)
P4	8(1)	1(4)	55(7)	8(5)	7(6)	-1(4)

Table 2.6

Anisotropic Thermal Parameters ($\times 10^{-4}\text{\AA}$) for $P2_1$ Space Group

Atom	U11	U22	U33	U12	U13	U23
V1	7(1)	59(6)	53(5)	-15(5)	16(7)	21(6)
V1'	37(9)	56(6)	45(5)	10(5)	1(7)	-26(5)
V2	3(1)	60(6)	36(5)	29(5)	1(7)	-17(5)
V2'	6(9)	43(6)	45(5)	-2(4)	6(7)	27(5)
V3	8(1)	40(6)	47(5)	21(5)	4(7)	-16(6)
V3'	7(1)	52(6)	46(5)	-4(5)	-18(7)	32(6)
V4	6(1)	38(5)	33(5)	15(5)	12(7)	-20(5)
V4'	5(1)	40(5)	37(5)	-20(5)	-6(6)	16(5)
P1	1(1)	8(1)	17(8)	8(8)	1(1)	6(6)
P1'	6(1)	5(1)	33(8)	11(9)	-20(1)	-6(6)
P2	2(1)	7(1)	37(9)	-19(8)	-1(1)	-1(6)
P2'	1(1)	6(1)	17(8)	14(8)	-10(9)	-4(6)
P3	9(2)	6(1)	2(1)	-26(9)	1(1)	7(6)
P3'	5(1)	4(1)	48(9)	6(9)	-1(1)	5(6)
P4	6(2)	5(1)	4(1)	-4(9)	10(1)	6(6)
P4'	3(1)	5(1)	23(8)	10(8)	1(1)	-11(6)

Table 2.7Bond Distances (Å) for Pca2₁ Space Group

V1	O1	1.597(5)	P1	O5	1.574(4)
	O7	1.932(3)		O9	1.556(3)
	O8	1.944(3)		O14	1.480(3)
	O9	2.074(3)		O16	1.494(3)
	O10	2.070(3)			
V2	O2	1.615(6)	P2	O5	1.568(4)
	O2	2.300(6)		O10	1.564(3)
	O9	2.079(3)		O13	1.496(3)
	O10	2.076(3)		O15	1.513(3)
	O11	1.964(3)			
	O12	1.950(3)			
V3	O3	1.591(8)	P3	O6	1.584(4)
	O3	2.283(8)		O7	1.500(3)
	O15	1.936(3)		O11	1.498(3)
	O16	1.948(3)		O18	1.551(4)
	O17	2.075(3)			
	O18	2.066(3)			
V4	O4	1.604(5)	P4	O6	1.580(4)
	O4	2.268(5)		O8	1.496(3)
	O13	1.937(3)		O12	1.498(3)
	O14	1.942(3)		O17	1.555(3)
	O17	2.054(3)			
	O18	2.086(3)			

Table 2.8

Interatomic Angles ($^{\circ}$) for Pca2₁ Space Group

O1-V1-O7	99.0(2)	O3-V3-O15	103.0(2)
O1-V1-O8	104.2(2)	O3-V3-O16	98.1(2)
O1-V1-O9	98.5(2)	O3-V3-O17	94.5(2)
O1-V1-O10	97.2(2)	O3-V3-O18	100.3(3)
O7-V1-O8	91.6(1)	O3-V3-O15	78.2(2)
O7-V1-O9	91.5(1)	O3-V3-O16	85.2(2)
O7-V1-O10	161.8(2)	O3-V3-O17	82.0(2)
O8-V1-O9	156.3(2)	O3-V3-O18	78.2(2)
O8-V1-O10	92.5(1)	O15-V3-O16	92.5(1)
O9-V1-O10	77.8(1)	O15-V3-O17	93.1(1)
O2-V2-O2	174.2(1)	O15-V3-O18	155.8(2)
O2-V2-O9	97.1(2)	O16-V3-O17	164.6(2)
O2-V2-O10	97.5(2)	O16-V3-O18	90.8(1)
O2-V2-O11	103.4(2)	O17-V3-O18	78.4(1)
O2-V2-O12	97.5(1)	O4-V4-O4	175.6(2)
O2-V2-O9	77.5(2)	O4-V4-O13	101.4(2)
O2-V2-O10	79.6(2)	O4-V4-O14	98.5(2)
O2-V2-O11	79.2(1)	O4-V4-O17	95.0(2)
O2-V2-O12	87.8(1)	O4-V4-O18	100.6(3)
O9-V2-O10	77.6(1)	O4-V4-O13	79.7(2)
O9-V2-O11	95.3(1)	O4-V4-O14	85.8(2)
O9-V2-O12	164.2(2)	O4-V4-O17	80.7(2)
O10-V2-O11	158.6(2)	O4-V4-O18	77.8(2)
O10-V2-O12	94.4(1)	O13-V4-O14	90.7(1)
O11-V2-O12	87.3(1)	O13-V4-O17	91.7(1)
O3-V3-O3	176.4(2)	O13-V4-O18	156.6(2)
O14-V4-O17	165.6(2)	O12-P4-O17	109.1(2)
O14-V4-O18	94.0(1)	V2-O2-V2	161.1(2)
O17-V4-O18	78.4(1)	V3-O3-V3	171.9(2)

Table 2.8 (continued)

O5-P1-O9	105.8 (3)	V4-O4-V4	172.2 (2)
O5-P1-O14	107.2 (2)	P1-O5-P2	158.7 (2)
O5-P1-O16	107.3 (2)	P3-O6-P4	145.1 (2)
O9-P1-O14	111.1 (2)	V1-O7-P3	156.2 (2)
O9-P1-O16	109.7 (2)	V1-O8-P4	156.2 (2)
O14-P1-O16	115.2 (2)	V1-O9-V2	102.2 (1)
O5-P2-O10	107.7 (3)	V1-O9-P1	130.2 (2)
O5-P2-O13	107.7 (2)	V2-O9-P1	127.1 (2)
O5-P2-O15	106.9 (2)	V1-O10-V2	102.4 (1)
O10-P2-O13	109.7 (2)	V1-O10-P2	129.0 (2)
O10-P2-O15	110.2 (2)	V2-O10-P2	128.6 (2)
O13-P2-O15	114.3 (2)	V2-O11-P3	132.2 (3)
O6-P3-O7	110.1 (2)	V2-O12-P4	143.6 (2)
O6-P3-O11	105.8 (2)	V4-O13-P2	140.3 (3)
O6-P3-O18	103.9 (3)	V4-O14-P1	153.0 (3)
O7-P3-O11	115.1 (2)	V3-O15-P2	138.2 (3)
O7-P3-O18	110.2 (2)	V3-O16-P1	148.8 (2)
O11-P3-O18	111.1 (3)	V3-O17-V4	102.0 (1)
O6-P4-O8	108.7 (2)	V3-O17-P4	125.6 (2)
O6-P4-O12	106.7 (2)	V4-O17-P4	128.6 (3)
O6-P4-O17	104.5 (3)	V3-O18-V4	101.2 (1)
O8-P4-O12	116.6 (2)	V3-O18-P3	122.7 (3)
O8-P4-O17	110.5 (2)	V4-O18-P3	132.9 (2)

Table 2.9

Bond Angles ($^{\circ}$) for $P2_1$ Space Group

01-V1-07	99.0(3)	02'-V2-010	79.9(2)
01-V1-08	103.9(2)	02'-V2-011	79.7(2)
01-V1-09	98.3(3)	02'-V2-012	88.4(2)
01-V1-010	97.5(3)	09-V2-010	77.3(2)
07-V1-08	91.6(2)	09-V2-011	95.7(2)
07-V1-09	91.4(2)	09-V2-012	164.8(3)
07-V1-010	161.4(2)	010-V2-011	159.4(3)
08-V1-09	156.8(3)	010-V2-012	95.1(2)
08-V1-010	92.6(2)	011-V2-012	86.9(2)
09-V1-010	77.9(2)	02-V2'-02'	174.0(2)
01'-V1'-07'	98.5(3)	02-V2'-09'	78.0(2)
01'-V1'-08'	104.6(3)	02-V2'-010'	80.3(2)
01'-V1'-09'	99.0(3)	02-V2'-011'	77.9(2)
01'-V1'-010'	97.6(3)	02-V2'-012'	86.9(2)
07'-V1'-08'	91.8(2)	02'-V2'-09'	96.1(2)
07'-V1'-09'	91.6(2)	02'-V2'-010'	97.2(3)
07'-V1'-010'	161.9(2)	02'-V2'-011'	104.3(3)
08'-V1'-09'	155.3(3)	02'-V2'-012'	98.8(3)
08'-V1'-010'	92.0(2)	09'-V2'-010'	77.7(2)
09'-V1'-010'	77.8(2)	09'-V2'-011'	95.3(2)
02-V2-02'	174.6(2)	09'-V2'-012'	163.9(3)
02-V2-09	97.5(3)	010'-V2'-011'	158.1(3)
02-V2-010	97.3(3)	010'-V2'-012'	94.6(2)
02-V2-011	102.9(3)	011'-V2'-012'	86.7(2)
02-V2-012	96.5(3)	03-V3-03'	175.9(2)
02'-V2-09	77.4(2)	03-V3-015	104.2(3)
03-V3-016	99.5(3)	016'-V3'-018'	91.0(2)
03-V3-017	94.6(3)	017'-V3'-018'	78.6(2)
03-V3-018	100.3(3)	04-V4-04'	175.6(2)
03'-V3-015	76.9(2)	04-V4-013	101.5(3)
03'-V3-016	84.4(2)	04-V4-014	99.3(3)
03'-V3-017	81.3(2)	04-V4-017'	95.3(3)
03'-V3-018	78.2(2)	04-V4-018'	100.9(3)
015-V3-016	92.4(2)	04'-V4-013	79.3(2)
015-V3-017	92.8(2)	04'-V4-014	85.0(2)
015-V3-018	154.6(3)	04'-V4-017'	80.3(2)
016-V3-017	163.3(2)	04'-V4-018'	77.8(2)
016-V3-018	90.5(2)	013-V4-014	90.6(2)
017-V3-018	78.2(2)	013-V4-017'	91.4(2)
03-V3'-03'	176.7(2)	013-V4-018'	156.1(3)
03-V3'-015'	79.7(2)	014-V4-017'	164.5(3)

Table 2.9 (continued)

03-V3'-016'	86.5(3)	014-V4-018'	93.9(2)
03-V3'-017'	82.0(2)	017'-V4-018'	78.3(2)
03-V3'-018'	77.7(2)	04-V4'-04'	175.9(2)
03'-V3'-015'	101.9(3)	04-V4'-013'	80.1(2)
03'-V3'-016'	96.3(3)	04-V4'-014'	86.9(2)
03'-V3'-017'	94.9(3)	04-V4'-017	81.6(2)
03'-V3'-018'	100.4(3)	04-V4'-018	78.2(2)
015'-V3'-016'	92.9(2)	04'-V4'-013'	101.1(3)
015'-V3'-017'	93.1(2)	04'-V4'-014'	97.0(3)
015'-V3'-018'	156.8(3)	04'-V4'-017	94.4(3)
016'-V3'-017'	165.9(3)	04'-V4'-018	100.1(3)
013'-V4'-014'	90.8(2)	05-P2'-015'	105.5(3)
013'-V4'-017	92.3(2)	010'-P2'-013'	110.2(4)
013'-V4'-018	157.3(3)	010'-P2'-015'	110.4(3)
014'-V4'-017	167.4(3)	013'-P2'-015'	115.3(3)
014'-V4'-018	94.3(2)	06'-P3-07'	109.9(3)
017-V4'-018	78.3(2)	06'-P3-011	105.4(3)
05-P1-09	106.0(4)	06'-P3-018	104.1(3)
05-P1-014	105.8(3)	07'-P3-011	115.1(3)
05-P1-016	106.2(3)	07'-P3-018	110.6(3)
09-P1-014	111.4(4)	011-P3-018	111.0(3)
09-P1-016	110.3(3)	06-P3'-07	109.8(4)
014-P1-016	116.3(3)	06-P3'-011'	106.7(3)
05'-P1'-09'	106.5(4)	06-P3'-018'	104.0(3)
05'-P1'-014'	109.3(4)	07-P3'-011'	115.0(3)
05'-P1'-016'	108.4(3)	07-P3'-018'	109.9(3)
09'-P1'-014'	110.2(3)	011'-P3'-018'	110.8(4)
09'-P1'-016'	109.2(3)	06-P4-08'	108.0(3)
014'-P1'-016'	113.0(4)	06-P4-012	107.7(3)
05'-P2-010	107.1(3)	06-P4-017	103.9(3)
05'-P2-013	108.4(3)	08'-P4-012	116.4(3)
05'-P2-015	107.9(3)	08'-P4-017	110.7(3)
010-P2-013	109.2(3)	012-P4-017	109.3(3)
010-P2-015	110.2(3)	06'-P4'-08	109.9(3)
013-P2-015	113.8(3)	06'-P4'-012'	105.7(3)
05-P2'-010'	107.6(4)	06'-P4'-017'	104.5(3)
05-P2'-013'	107.2(3)	08-P4'-012'	115.9(3)
08-P4'-017'	110.9(3)	V1'-010'-P2'	129.0(4)
012'-P4'-017'	109.2(3)	V2'-010'-P2'	128.8(4)
V2-O2-V2'	161.7(3)	V2-O11-P3	132.8(4)
V2-O2'-V2'	160.2(3)	V2'-011'-P3'	130.9(4)
V3-O3-V3'	170.8(3)	V2-O12-P4	142.8(4)
V3-O3'-V3'	173.1(4)	V2'-012'-P4'	145.1(4)
V4-O4-V4'	171.8(3)	V4-O13-P2	139.5(4)

Table 2.9 (continued)

V4-04'-V4'	172.5 (3)	V4'-013'-P2'	140.9 (4)
P1-05-P2'	157.9 (4)	V4-014-P1	154.4 (4)
P1'-05'-P2	159.0 (4)	V4'-014'-P1'	150.9 (4)
P3'-06-P4	145.5 (3)	V3-015-P2	136.4 (4)
P3-06'-P4'	144.7 (3)	V3'-015'-P2'	139.6 (4)
V1-07-P3'	155.8 (3)	V3-016-P1	149.8 (4)
V1'-07'-P3	156.4 (3)	V3'-016'-P1'	147.5 (4)
V1-08-P4'	157.7 (4)	V3-017-V4'	102.6 (2)
V1'-08'-P4	154.9 (4)	V3-017-P4	125.8 (3)
V1-09-V2	102.3 (3)	V4'-017-P4	128.8 (3)
V1-09-P1	130.6 (4)	V3'-017'-V4	101.8 (3)
V2-09-P1	126.7 (4)	V3'-017'-P4'	126.0 (4)
V1'-09'-V2'	102.4 (2)	V4-017'-P4'	128.0 (4)
V1'-09'-P1'	130.1 (3)	V3-018-V4'	100.9 (3)
V2'-09'-P1'	127.3 (3)	V3-018-P3	122.7 (4)
V1-010-V2	102.6 (2)	V4'-018-P3	132.5 (4)
V1-010-P2	129.2 (4)	V3'-018'-V4	101.2 (2)
V2-010-P2	128.1 (3)	V3'-018'-P3'	122.7 (3)
V1'-010'-V2'	102.1 (3)	V4-018'-P3'	132.9 (4)

Table 2.10
Bond Distances for $P2_1$ Space Group

V1	O1	1.585 (6)	V3	O3	1.602 (8)
	O1'	2.337 (6)		O3'	2.277 (9)
	O7	1.936 (5)		O15	1.948 (6)
	O8	1.935 (5)		O16	1.945 (5)
	O9	2.067 (6)		O17	2.066 (6)
	O10	2.065 (6)		O18	2.070 (6)
V1'	O1	2.307 (6)	V3'	O3	2.266 (8)
	O1'	1.585 (6)		O3'	1.601 (9)
	O7'	1.929 (5)		O15'	1.932 (6)
	O8'	1.951 (6)		O16'	1.943 (5)
	O9'	2.071 (6)		O17'	2.071 (6)
	O10'	2.075 (7)		O18'	2.062 (6)
V2	O2	1.597 (8)	V4	O4	1.617 (7)
	O2'	2.307 (7)		O4'	2.257 (7)
	O9	2.081 (7)		O13	1.930 (5)
	O10	2.076 (6)		O14	1.935 (5)
	O11	1.957 (6)		O17'	2.062 (6)
	O12	1.951 (5)		O18'	2.087 (6)
V2'	O2	2.323 (8)	V4'	O4	2.253 (7)
	O2'	1.606 (7)		O4'	1.619 (7)
	O9'	2.075 (6)		O13'	1.934 (5)
	O10'	2.079 (6)		O14'	1.939 (5)
	O11'	1.964 (6)		O17	2.043 (6)
	O12'	1.949 (5)		O18	2.088 (6)

Table 2.10 (continued)

P1	O5	1.599 (7)	P2	O5'	1.560 (7)
	O9	1.554 (6)		O10	1.573 (5)
	O14	1.478 (5)		O13	1.510 (6)
	O16	1.486 (6)		O15	1.518 (6)
P1'	O5'	1.564 (7)	P2'	O5	1.565 (7)
	O9'	1.563 (5)		O10'	1.554 (6)
	O14'	1.497 (6)		O13'	1.489 (6)
	O16'	1.509 (6)		O15'	1.497 (6)
P3	O6'	1.612 (6)	P4	O6	1.567 (6)
	O7'	1.498 (5)		O8'	1.496 (5)
	O11	1.498 (6)		O12	1.506 (6)
	O18	1.544 (6)		O17	1.568 (6)
P3'	O6	1.568 (6)	P4'	O6'	1.574 (6)
	O7	1.497 (6)		O8	1.495 (5)
	O11'	1.516 (6)		O12'	1.484 (6)
	O18'	1.557 (6)		O17'	1.549 (6)

thermal parameters and final atomic positions are given in Tables 2.3 and 2.4, anisotropic thermal parameters are given Tables 2.5 and 2.6, and interatomic distances and bond angles are given in Tables 2.7 to 2.10.

2.3 Discussion

Titration data, measuring average vanadium oxidation state, for emerald green crystals and mixtures of emerald green and red-brown crystals were consistently 4.00 and 4.01 respectively. The mechanism for the incorporation of the extra oxygen in the red-brown crystals is presumably related to the defect described in detail in the next chapter.

Data collected using Mo-K α radiation and standard $\theta/2\theta$ scan technique indicates good orthorhombic mmm symmetry with space group extinctions consistent with the choice of centrosymmetric Pcam or non-centrosymmetric Pca2 $_1$. However, there were a number of very weak reflections that violated the extinction conditions for both of these space groups, Table 2.11. The only space group consistent with the symmetry and reflection conditions was the monoclinic group P2 $_1$, no. 4.

Refinement in the centrosymmetric space group Pc_{2m} consistently resulted in a large amount of electron density remaining in the difference Fourier analysis, and relatively high R-values, $R = 9.6\%$. We concluded that using this space group could not produce a good solution to the structure.

Refinement in the non-centrosymmetric space group, $Pca2_1$, gave very good preliminary results for the solution to the crystal structure. The final R-value was refined to 4.1% . All the bond lengths and bond angles were consistent to what is observed for other vanadium-phosphorous-oxide structures (8,9). However, a flaw with using this space group, similar to what was observed for the centrosymmetric space group Pc_{2m} , was that significant residual electron density was still evident in difference Fourier analyses, Figure 2.3. Even when all atoms were allowed to refine with anisotropic thermal parameters, the excess electron density could not be adequately removed. A refinement based on disordering the vanadium atoms between the two sites found in the difference Fourier also failed to remove the extra electron density.

The next step in the refinement process was to refine the structure in the monoclinic space group, $P2_1$. Similar to the previous two space groups, the vanadium atoms were

located by direct methods. The phosphorous and oxygen atoms were located on subsequent least-squares refinement and difference Fourier electron density maps. The results of the refinements are summarized in Tables 2.4, 2.6, and 2.9. The final refined R-value of 4.4%, with all the metal atoms allowed to refine with isotropic thermal parameters, is slightly higher than that observed for the orthorhombic case. If all atoms were allowed to refine with anisotropic thermal parameters, all but 3 oxygen atoms could be refined with positive U_{ij} components. When the extra reflections that were not allowed in the orthorhombic symmetry were removed from the refinement cycles, the R-value dropped to 4.1% with only the metal atoms refined with anisotropic thermal parameters.

A major advantage of the refinement in the monoclinic space group is that the residual electron densities that were observed for the orthorhombic model were essentially absent, Figure 2.5. Furthermore, the presence of reflections forbidden in the orthorhombic space group necessitates using a lower symmetry space group.

The crystal structure of $(VO)_2P_2O_7$ can best be described as layers of edge-sharing vanadium pseudo-octahedra, $V_2O_2^{4+}$ encompassed by pyrophosphate tetrahedra, $P_2O_7^{-4}$ units, Figure 2.1. It is these pyrophosphate units as well as the strong

vanadium to oxygen interactions that are responsible for uniting the layers and extending the structure into a three-dimensional network, Figure 2.2.

In $(VO)_2P_2O_7$, each vanadium atom forms one short V-O bond ($\sim 1.6\text{\AA}$) and one long V-O bond ($\sim 2.3\text{\AA}$), Figure 2.2. When viewing in a direction perpendicular to the layer direction, along the ab plane, the arrangement of the edge-sharing pairs of octahedra units is to have the two short V=O bonds arranged across one another, 'trans', and not in a side-by-side order, 'cis'. Having a 'trans' type of ordering will maximize the distance between regions of high of electron density. The unit will repeat throughout the crystal in a $O\cdots V=O\cdots V=O\cdots V=O\cdots V$ type of fashion, Figure 2.2, which can be described as chains of alternating short-long vanadium oxygen bonds. The chains run in a direction parallel to the a-axis.

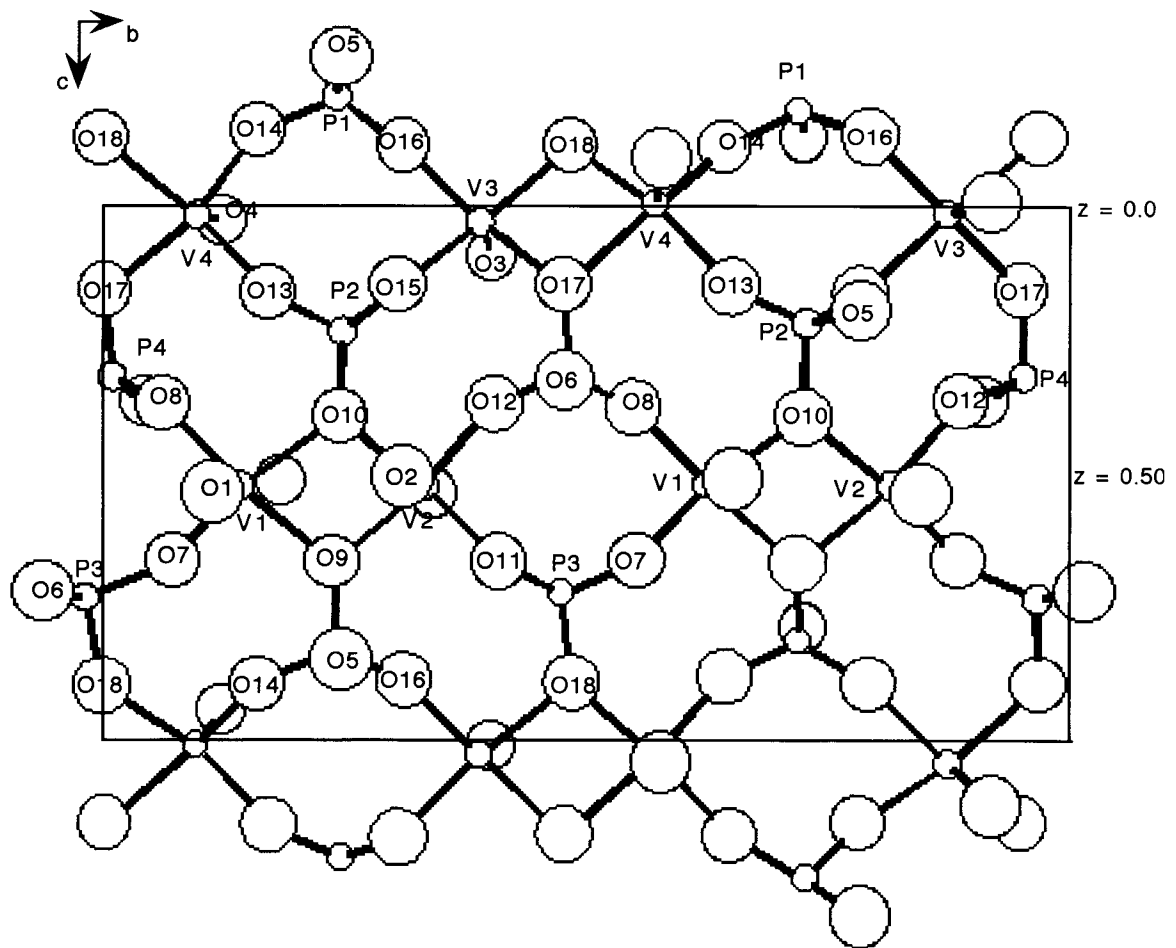


Figure 2.1. Crystal structure of vanadyl pyrophosphate viewed perpendicular to the (100) face. Only one layer is shown for clarity. Atoms with prime components are not shown but are on the next layer above the one shown. The vanadium chains are approximately at $z = 0$ and $z = 1/2$.

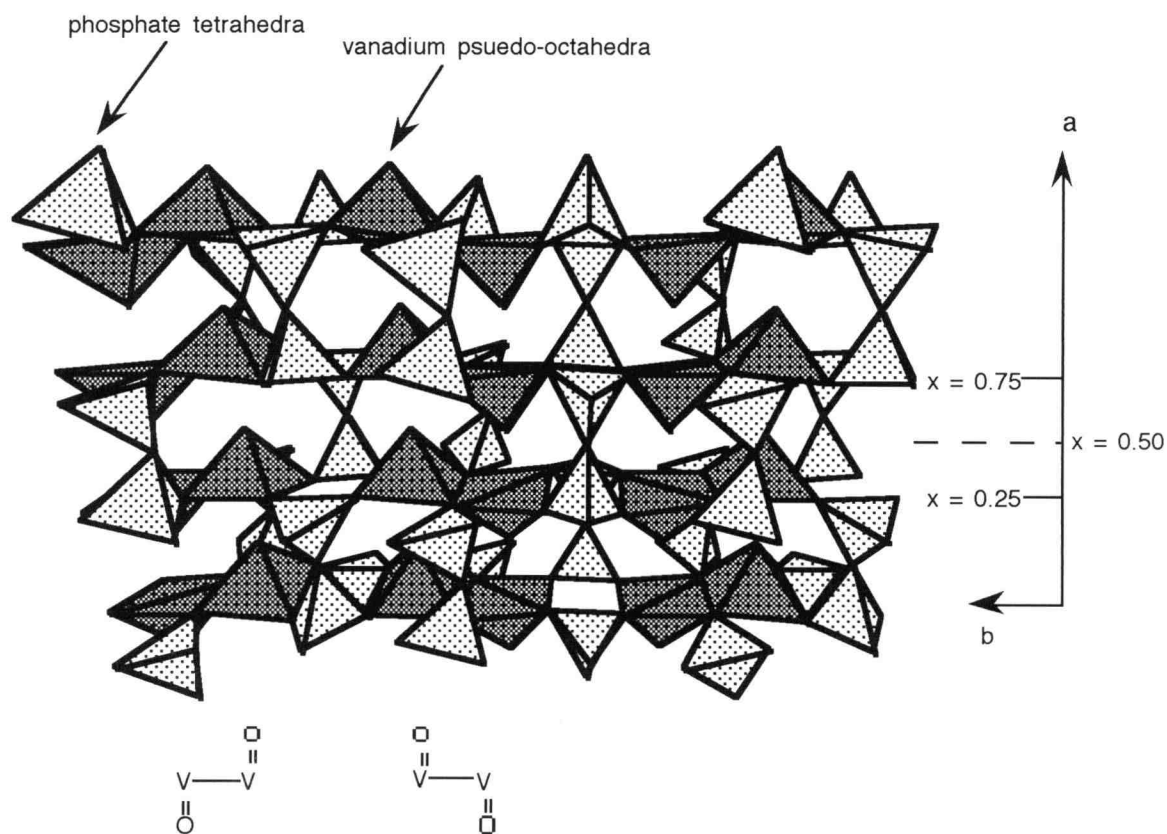


Figure 2.2. View of $(VO)_2P_2O_7$ looking approximately down the (001) face. The layers of edge-shared vanadium pseudo-octahedra are situated at $x = 1/4$ and $x = 3/4$. The 'trans' relative position of the short V=O bond between the edge-shared moiety is clearly evident.

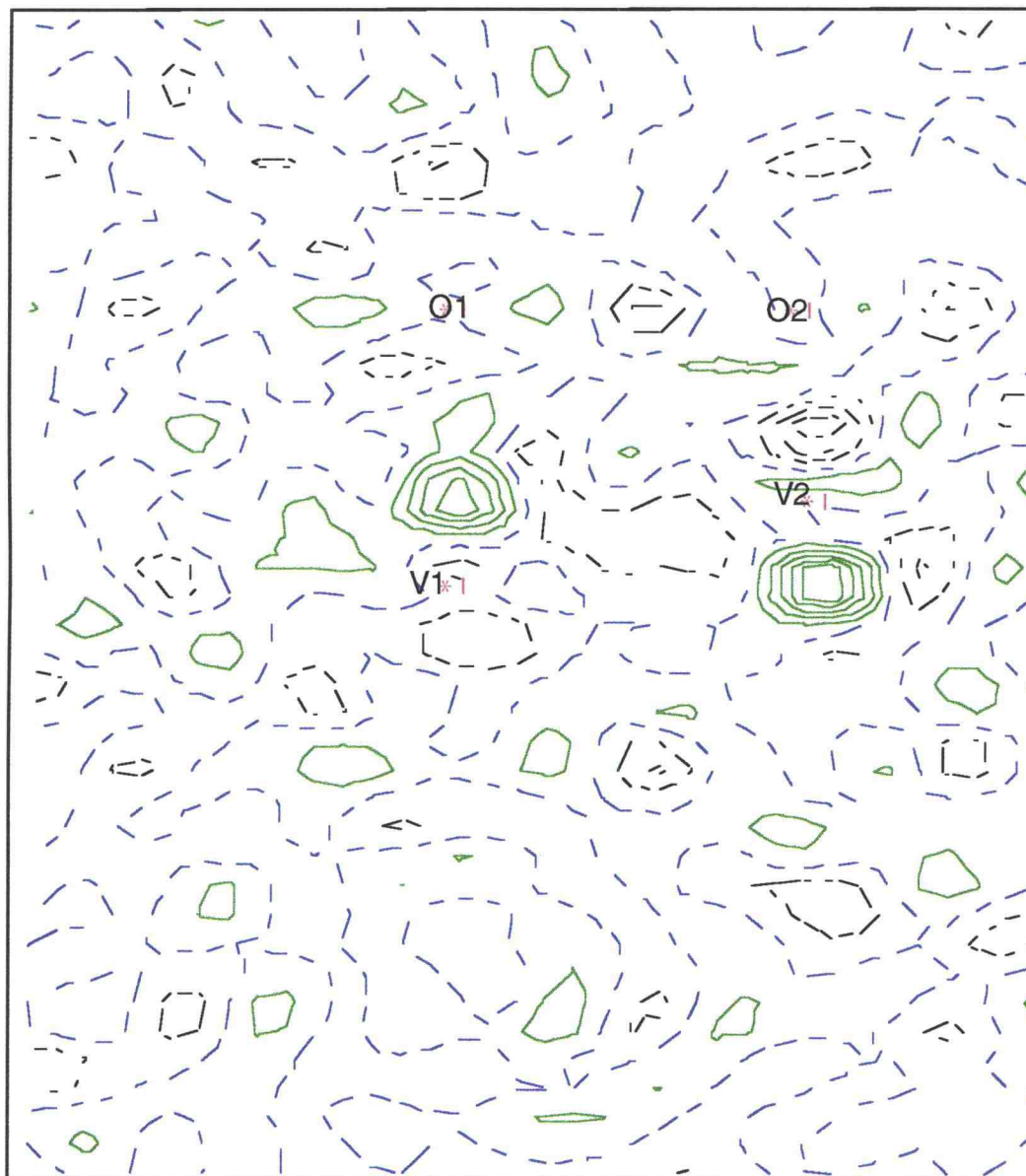


Figure 2.3. Difference Fourier electron density map for $Pca2_1$ space group refinement. The direction of the vanadium-oxygen chains are parallel to the length of the page. The solid line is positive electron density, the faint dashed line is neutral, and the dark dash line is negative electron density. The figure eight configuration is clearly evident around each vanadium atom. Each line represents 0.5 electron unit.

There are two distinct chains which lie perpendicular to the bc-plane at approximately $z = 0$ and $z = 0.5$, Figure 2.1. The layers of edge-sharing vanadium octahedra are arranged parallel to the bc-plane and are situated at approximately $x = 1/4$ and $x = 3/4$ of the unit cell, Figure 2.2. The best previous solution of the crystal structure concluded that the vanadium positions within the crystal were randomly disordered within the lattice. This was the only way which Thompson and Ebner found to deal with their difference Fourier electron density maps. The vanadium atoms were observed to have extra electron density residues in a figure eight configuration in the direction of the chains. This behavior was also observed by our analysis, Figure 2.3. Thompson and Ebner observed residuals for all vanadium atoms in the sample prepared with aqueous solvents (red-brown color crystals) but only for one-half of the vanadium atoms for samples prepared with organic solvents (emerald green crystals). We, however, observed the effect for all vanadium atoms from our refinements for three green crystals.

The solution of Thompson and Ebner to remove these residuals was to split the vanadium occupancy equally between the two sites. The final reported refinement had an R-value of 3.5% with little or no excess electron density from

difference Fourier maps. The explanation was that within the crystal isomerism could occur where the order of the short V=O bond could change in direction from $O \cdots V=O \cdots V=O \cdots V=O \cdots V$ to a configuration similar to $O \cdots V=O \cdots V=O=V \cdots O=V \cdots O$. When we tried to repeat the strategy of Thompson and Ebner, our refinement diverged.

The crystal analyzed by Thompson and Ebner contained a high concentration of defects relative to the samples prepared in this work. Thompson and Ebner observed streaking effects for the parity groups $h = \text{even}, k = \text{even}, l = \text{odd}$ and $h = \text{even}, k = \text{odd}, l = \text{odd}$. We did not observe any streaking in our single crystal diffractometer scans or precession photographs.

A major difference between our results and previous reports is the observation of extra reflections for our single crystal. Some of these reflections were confirmed with zero-level precession photographs. A total of 38 reflections were observed that are not allowed in the space group $Pca2_1$. As alluded to earlier, the space group $P2_1$ satisfies all the symmetry conditions as well allowing for the extra reflections.

For both space groups, the vanadium to oxygen bond distances and angles were consistent with results from other

structure determinations. The average V-O bond length measured was 2.0Å neglecting the short V=O of 1.6Å and the long V···O bond of 2.3Å. The distance for a vanadium to oxygen double bond is ~1.56Å and for a long vanadium to oxygen single bond ~2.25Å. In an ideal octahedra, bond angles of 90° and 180° are expected. The values measured, Figure 2.4, were consistent with the expected value (9,10). Deviations from the ideal can be attributed to the edge-shared arrangement. Visually the vanadium atoms are pushing against one another to maximize their distance, thus narrowing the O-V-O angle at the common edge and increasing the other three O-V-O angles within the moiety.

As with the vanadate groups, the bond lengths and bond angles for the phosphate tetrahedra are similar to what is known in literature. The average phosphorous to oxygen bond length is 1.56Å. All the O-P-O bond angles are consistently close to the ideal 109.5°, ranging from 104° to 111°.

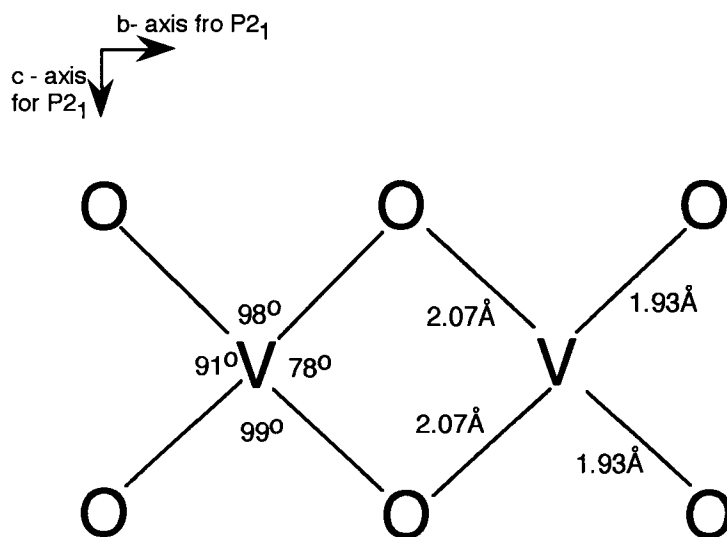


Figure 2.4. Average bond lengths and bond angles for an edge-shared vanadium moiety. The short V=O and long V···O bonds are neglected. The direction of view is along the vanadium chains, looking down the bc-plane.

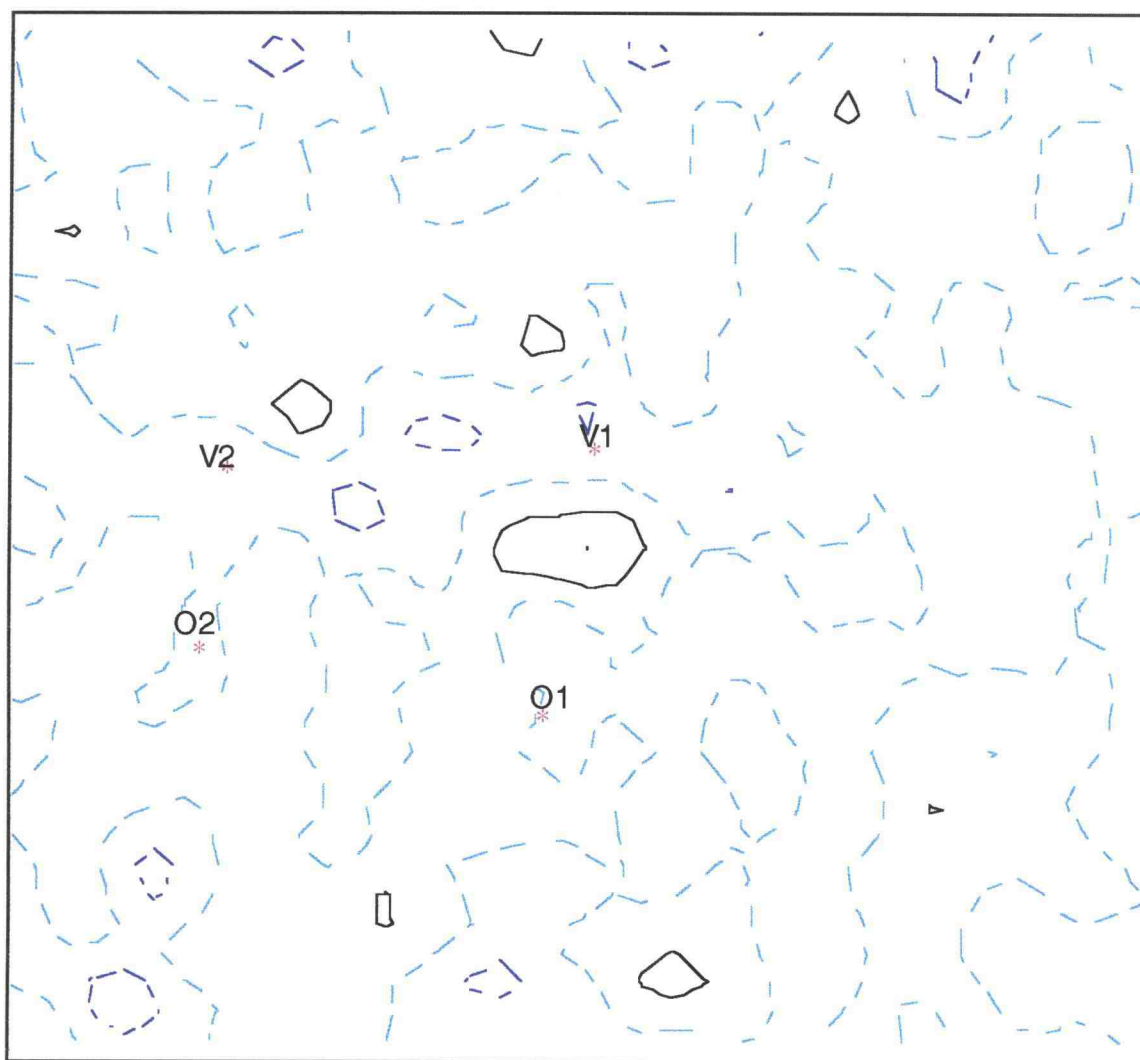


Figure 2.5. Difference Fourier electron density map for $P2_1$ space group refinement. The a-axis is running parallel to the length of the picture. The solid line is positive electron density, the faint dashed line is neutral, and the dark dash line is negative electron density. Each line represents 0.5 electron unit.

Table 2.11
F(obs) and F(calc) for reflections not allowed in Pca2₁

hkl (P2 ₁)	F (obs)	F(calc)	Sigma	Relative Error (F _{obs} -F _{calc})/Sigma
0 9 11	52	51	1	1.0
0 13 9	39	43	2	-2.0
0 5 11	55	33	3	-11.0
0 19 2	56	54	1	2.0
3 18 0	39	33	3	2.0
0 1 12	52	42	3	3.33
5 16 0	52	17	7	5.0
1 11 0	53	21	3	10.7
0 15 6	34	52	5	-3.6
0 7 9	44	33	2	5.5
0 13 6	38	43	3	-1.7
0 5 10	35	34	5	0.2
0 13 5	74	41	11	3.0
0 7 8	51	42	2	4.5
1 14 0	61	35	2	13.0
0 9 6	48	50	2	-1.0
5 8 0	31	19	3	4.0
1 13 0	38	29	3	-3.0
1 16 0	34	18	4	4.0
0 7 8	51	42	2	4.5
5 7 0	42	19	3	4.33
5 3 0	44	15	6	4.83
0 9 3	42	41	6	0.17
3 8 0	34	15	2	9.5
0 9 2	33	39	4	-0.67
0 3 7	39	33	5	1.2
0 9 4	42	21	7	3.0
0 3 6	41	40	1	1.0
0 1 5	31	27	4	1.0
0 5 4	40	19	7	3.0
0 5 3	56	30	6	4.3
0 3 3	43	25	7	2.6
0 5 6	44	15	6	3.2
1 6 0	86	35	4	12.75
5 0 0	55	45	2	5.0
3 0 0	64	60	2	2.0
1 0 0	63	35	1	28.0

Least square refinements of the final crystal structure solution for both orthorhombic and monoclinic space groups are presented in Tables 2.3 - 2.10. The monoclinic structure contains twice as many atoms in the asymmetric unit as the orthorhombic structure due to symmetry. The atoms labeled with primes in the monoclinic space group are related to the atoms without the prime designation by a glide plane.

A close examination of the two solutions shows very little disparity in the bond lengths and bond angles between the two space groups. This is expected since the extra reflections themselves are very weak and will most likely not significantly alter the final structure. Table 2.11 is the list of the final refinements for the extra reflections. The difference between the $F(\text{calculated})$ and the $F(\text{observed})$ are quite good for some cases like the 036, 093, and the 300 reflections but extremely different for the 100, 033, and the 054 reflections. Some of this effect might be attributed to the extremely low $F(\text{obs})$ for these reflections and thus a better refinement could be performed with better statistics. There is no trend readily observed from the list.

2.4 Conclusion

The structure solution for single crystals of $(VO)_2P_2O_7$ is best described in the monoclinic space group $P2_1$ which led to an R-value of 4.4%. This solution does not contain any unusual electron densities in a difference Fourier analysis and does not have atom disordering. Crystal color varies with oxygen content and ranges from emerald green to red-brown. The red-brown color is probably a result of excess oxygen trapped within the crystal lattice.

2.5 References

1. Yu.E. Gorbunova and S.A. Linde, *Sov. Phys. Dokl.*, **24**, 138 (1979)
2. N.E. Middlemiss, doctoral dissertation, Dept. of Chemistry, McMaster Univer. Hamilton, Ontario, Canada (1978)
3. J.R. Ebner and M.R. Thompson, *Studies in Surface Science and Catalysis*, ed. R.K. Grasselli and A.W. Sleight, Elsevier (1992)
4. M. Nakamura, K. Kawai, and Y. Fujiwara, *J. Catalysis*, **34**, 345-355, (1974)
5. TEXSAN, Molecular Structure Corporation, The Woodlands, TX, USA, (1988)
6. *Crystallographic Computing 3rd Ed.*, G. M. Sheldrick, C. Kruger, and R. Goddard, Oxford University Press, 1985, pp. 175-189.
7. *International Tables for Crystallography*, Vol A, ed. T.Hahn, D.Reidel Publ, Boston, (1983)
8. C.C. Toradi and J.C. Calabrese, *Inorg. Chem.*, **23**, 1308 (1984)
9. R. Gopal and C. Calvo, *J. Solid State Chemistry*, **5**, 432 (1972)
10. B.C. Frazer and P.J. Brown, *Physical Review*, **125**, 1283 (1962)
11. N. Walker and A. Stuart, *Acta Cryst.*, **A39**, 158-166, (1983)

Chapter 3

Modeling of Extended Defects in Vanadium Phosphate Catalyst

3.1 Introduction

X-ray and electron diffraction analyses of VPO catalysts indicate unusual behavior. In powder X-ray diffraction while some reflections are relatively sharp and intense, others are very weak or essentially absent even when the intensities calculated based on the ideal structure are significantly higher than background levels (1). In electron microscopy, streaking is observed (2). Finally, from single crystal X-ray data, unusual broadening for two classes of reflections was detected (3). There has been previous speculation that these diffraction effects were related to unknown stacking faults or antiphase boundaries, but to date there has been no description of these defects or their origin (2,4). In an effort to understand this unusual behavior, an investigation was undertaken to furnish a possible explanation for the observations. Models for the possible defects and defect formation in VPO samples were sought.

3.2 Experimental

Similar to the preparation conditions as described in chapter four, the catalyst precursor, $V_2P_2O_9 \cdot xH_2O$, was synthesized by refluxing V_2O_5 with 85% H_3PO_4 in a mixture of isobutanol and benzyl alcohol using a P-to-V ratio of 1.2. A typical reaction used 24.7g of H_3PO_4 , 15.6g V_2O_5 , 250 ml of isobutanol, and 18 ml of benzyl alcohol. After refluxing for 24 hours, the solid $V_2P_2O_9 \cdot 2H_2O$ was separated by vacuum filtration. This product was washed thoroughly with acetone to remove organic residue from the solid. X-ray diffraction showed single phase $V_2P_2O_9 \cdot 2H_2O$.

Conversion of $V_2P_2O_9 \cdot xH_2O$ to VPO was carried out under a variety of conditions, Table 3.1. The oxygen fugacity, $f(O_2)$, during calcination was fixed so that the only product obtained regardless of heating time was VPO. X-ray powder diffraction data were obtained at room temperature with a Siemens D-5000 diffractometer using CuK_α radiation. Strain and crystallite size data given in Table 3.1 are based on both the Williamson-Hall and Warren-Averbach approaches (5,6).

Table 3.1
DIFFaX Simulation Data

Calcination Conditions		% bc fault	Fault probability	Number of layers	Oxidation state	Size a	Strain		Strain	
Temp.	Time						a	⊥ a	a	⊥ a
400°C	7 days	90	9.5%	7	4.10	197Å	495Å	3.3	1.8	
645°C	3 days	80	7%	65	4.06	409Å	1181Å	2.3	1.5	
705°C	24 hrs	75	3%	500	4.03	928Å	1020Å	0.9	0.5	
790°C	12 hrs	70	1%	500	4.01	1367Å	1394Å	0.9	0.5	
Xtal	12 hrs	no faults	0%	600	4.00	>1500Å	>1500Å	<0.1	<0.1	

The average vanadium oxidation state measured by a method similar to the one introduced by Nakamura (24) is shown in Table 3.1. There is a direct, but subtle, correlation between the observed oxidation state to the fault probability for all five samples. With the approximate error of 1% for the fault probability, this observed relationship is significant.

3.3 Results

Depending on the synthesis conditions used for VPO, very different X-ray diffraction patterns can be obtained, Figure 3.1. Peak positions, relative to one another, shift by small amounts from sample to sample, but this is a small effect not readily observable in Figure 3.1. There are, however, major differences in both peak shapes and the integrated relative intensities of some peaks. Much of the variation in peak shape can be accounted for based on strain and crystallite size effects, after due consideration for the very anisotropic nature of these crystallites, Table 3.1. In fact, we assume that the broadening of peaks where h and l are both even is due entirely to these strain and size effects. The convention

of $a = 7.728\text{\AA}$, $b = 9.58\text{\AA}$, and $c = 16.588\text{\AA}$ is used for comparison with data in literature. These effects can be estimated along the a and b axes by using the 200, 400, 020, and 040 reflections. Reflections of the type 001 are too weak to conduct a similar analysis along the c axis. However, reflections of the type $0kl$ with l even fall into the same pattern as $0k0$ reflections, indicating similar parameters along b and c . Thus, these $0kl$ reflections are used to estimate strain and crystallite size perpendicular to a . The sharper peaks in the upper pattern of Figure 3.1 are all $0kl$ reflections. This should be taken as an indication that the crystallites are considerably larger perpendicular to the a direction, Table 3.1, consistent with their known platy character. The pronounced broadening of the 200 and 400 is an indication of very small crystallite dimensions along the a direction.

The extreme broadening of reflections with h or l odd cannot be related to strain or crystallite size effects. The broadening of these reflection can, however, be explained by assuming particular stacking faults perpendicular to the a axis (bc faults) or perpendicular to the c axis (ab faults) as shown in Figure 3.3. The software DIFFaX (7) was used to calculate the effect of

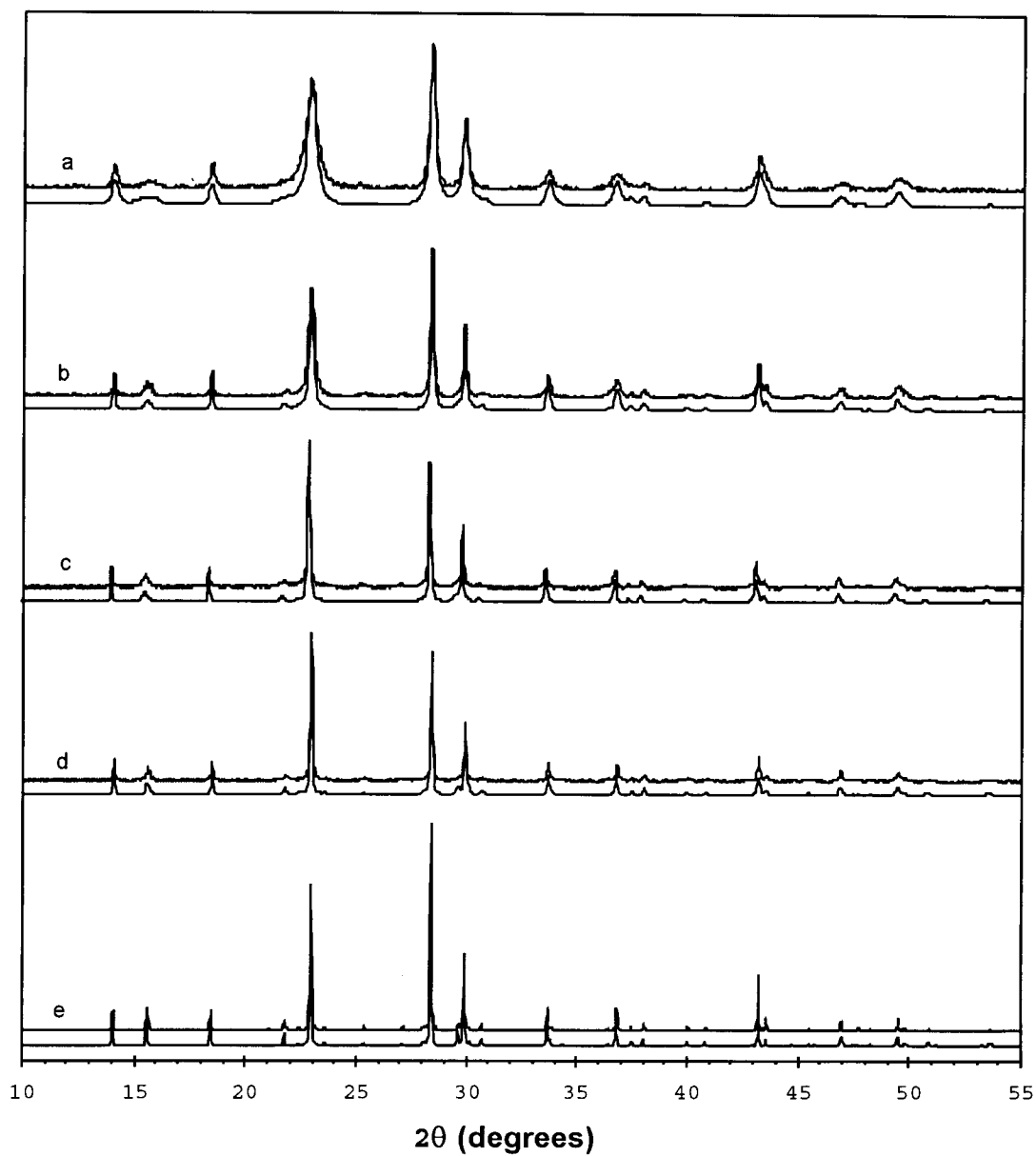
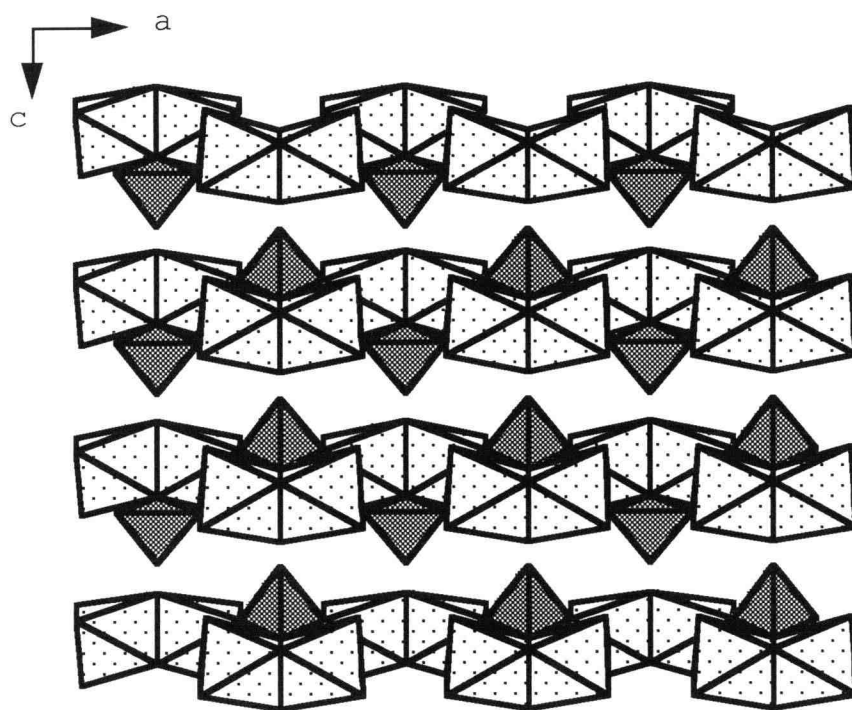


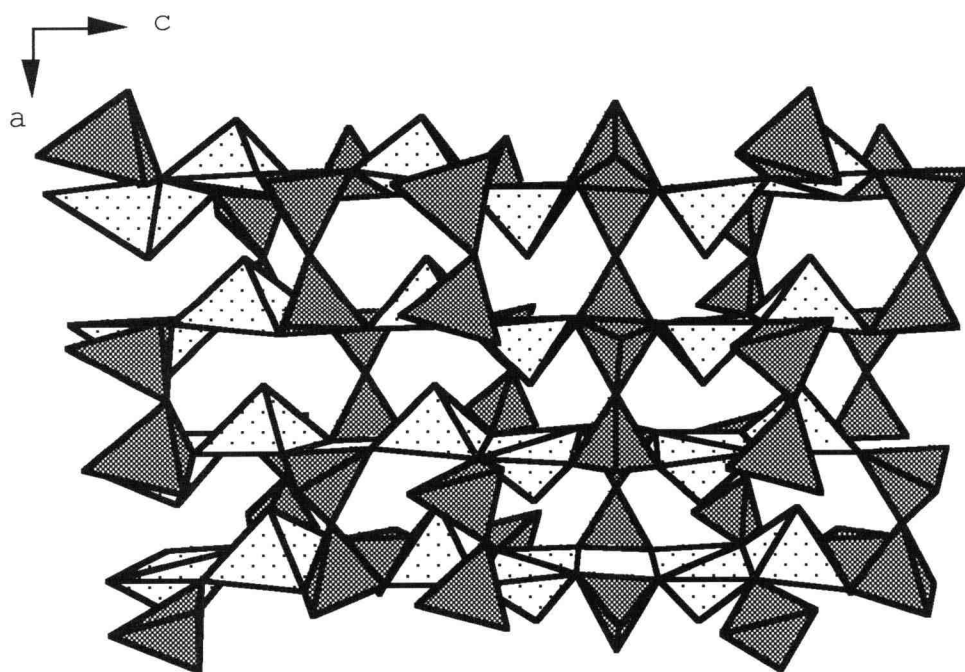
Figure 3.1. X-ray powder diffraction patterns and DIFFaX simulations of samples at a) 400°C b) 645°C c) 705°C d) 790°C and e) crystals of $(VO)_2P_2O_7$. The top pattern in each sample is the measured data.

these stacking faults on the X-ray diffraction patterns. Fault ab causes broadening of reflections where l is odd whereas fault bc causes broadening of peaks where h is odd. It was found that a good fit to the observed peak broadening required both ab and bc faults, although the bc fault predominates.

The calculated patterns are compared to observed patterns in Figure 3.1. The fitting parameters used to calculate these patterns are given in Table 3.1. The number of layers is defined as the number of unit cells along the a or c axes. All layers are identical, but the layers are shifted with respect to each other. For a given sample, both faults are calculated with the same stacking fault probability. The broadening and the disappearance of the hkl reflections with h or l odd relates primarily to an increase in the stacking fault density. For the sample prepared at 400°C , an expansion factor of 1.02 was used at the stacking fault. This is necessary to account for the small but significant shifts of peak positions relative to each other. This effect is only noticeable when the stacking fault density is very high. As might be expected, strain parallel and perpendicular to the a axis increases, Table 3.1, as the stacking fault density increases.



(a)



(b)

Figure 3.2. Crystal structure of a) $V_2P_2O_9 \cdot 2H_2O$ looking down the b axis and b) $(VO)_2P_2O_7$ looking down the b axis.

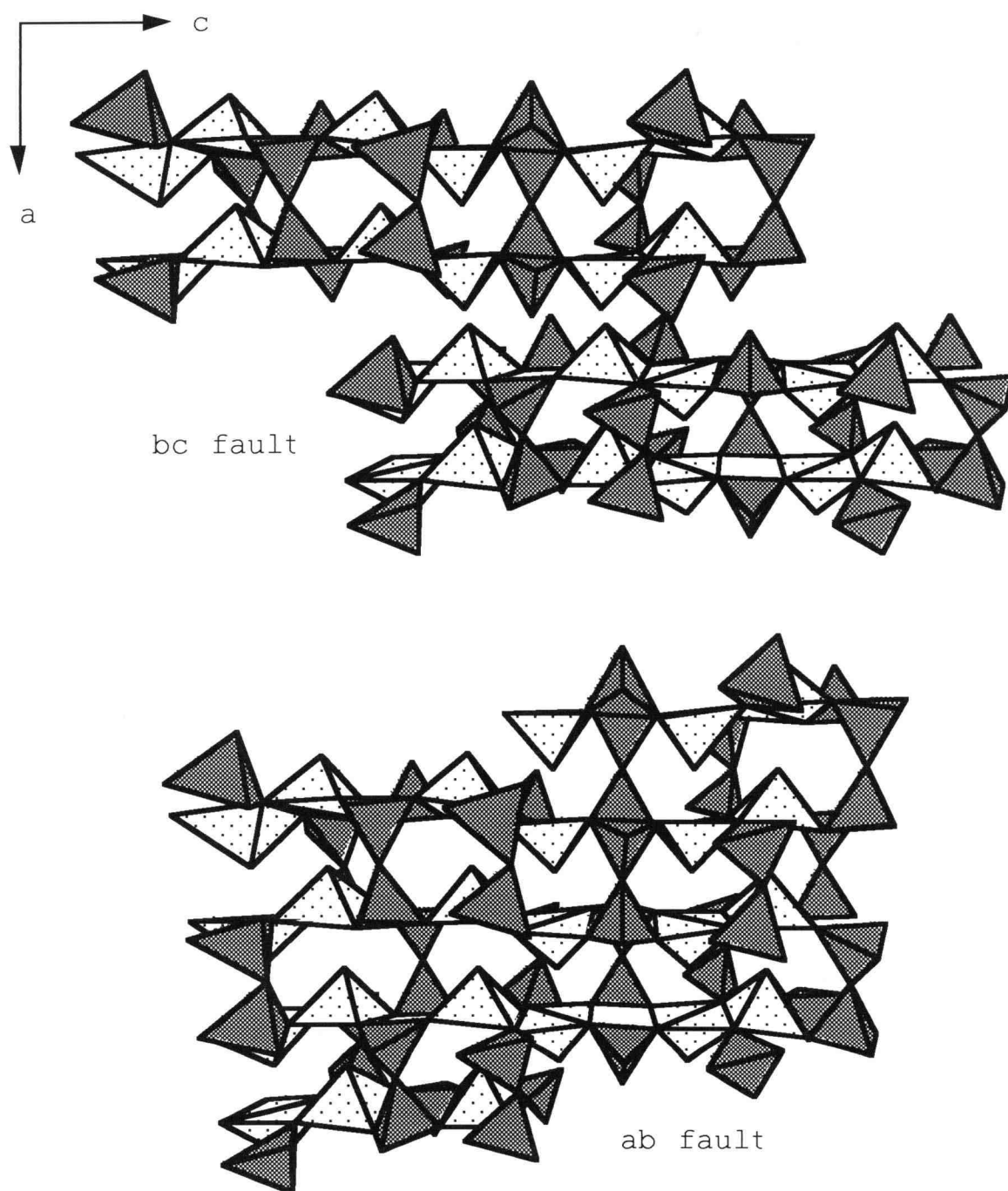


Figure 3.3. Definitions of faults used in DIFFaX simulations.

Ebner and Thompson (3) recently reported streaking involving hkl reflections where the indices are even-even-odd or even-odd-odd. We find that DIFFaX calculations can simulate these streaks based on our conclusion of a dominant bc fault. Bordes and Courtine (2), on the other hand, report streaking along $00l$ as well as streaking along 100 . The streaking along $00l$ cannot be simulated with bc faults but can be simulated with ab faults. This may be taken as confirmation that both types of faults are present.

Recently, another type of extended defect was reported to be present in VPO catalysts (8). We have simulated the effect that this defect would have on an X-ray diffraction pattern. We find that this defect cannot produce the observed line broadening and that the line broadening produced by this type of defect is not observed in actual VPO catalysts. This does not indicate the absence of such a defect, but it does show that such defects are present in concentrations much lower than the defects we find.

3.4 Discussion

We have taken special care to produce homogeneous VPO catalysts. Typical VPO catalysts which have been studied are clearly inhomogeneous. This inhomogeneity could cause peak broadening features which we wished to avoid because they would greatly complicate our already complex analysis. Inhomogeneities of VPO catalyst could result either from the way it is used in a reactor or from the way the precursor is transformed to catalyst. A VPO catalyst from a plug-flow, fixed-bed reactor will be exposed to a different temperature and a different gas phase mixture at different regions in the bed. This then could lead to, for example, a different average vanadium oxidation state for catalyst taken from different regions of the reactor. This in turn might have some small, but significant, impact on X-ray peak shapes.

Freshly prepared VPO catalysts are also inhomogeneous when prepared by standard methods. This is caused primarily by the fact that the vanadium oxidation state is not well controlled during the conversion of the precursor to the catalyst. Literature reports nearly always describe this conversion being carried out under air (1-2,9-17). At this condition, $V_2P_2O_9$ will eventually be converted

completely to VPO_5 . Limiting the calcination time can lead to a product where the oxidation state of vanadium is close to four, but the average oxidation state of vanadium is very likely to be significantly different from particle to particle, with some variation within a particle as well. The most common method of preparing VPO catalysts involves the use of organic chemicals. Normally, these chemicals are not completely removed before calcination. During calcination there are then competing redox processes. Reduction of the vanadium oxidation state to values below four may occur by reaction with the organic residue. On the other hand, the vanadium in VPO may be oxidized to values greater than four by oxidation with air. Thus, it is likely that during normal precursor conversion, the center of a sample may be initially reduced at the same time that the exterior regions are being oxidized. Recent NMR studies have (1,18-20), in fact, confirmed that different regions of a converted precursor have different oxidation states for vanadium.

The usual uncontrolled conversion of precursor $V_2P_2O_9 \cdot xH_2O$ to VPO can apparently diminish the crystallinity of the intermediates in this conversion. Several groups have reported an amorphous intermediate when the

crystalline precursor is transformed to crystalline catalyst. We find that this generally occurs if the organic residue is not washed from the catalyst. In our procedure, the organic residue is removed before dehydration of the precursor, and the oxygen partial pressure is controlled throughout the dehydration process. Thus, at no time during the precursor to catalyst conversion is there significant reduction or oxidation of vanadium. X-ray diffraction of partially converted VPO shows no indication of an amorphous phase at any step. Partially converted materials instead always show a mixture of crystalline $V_2P_2O_9 \cdot xH_2O$ and $V_2P_2O_9$. Thus, we believe that the transformation is truly topotactic and that our samples are highly homogeneous. It should be emphasized that some line broadening during a topotactic reaction is expected. As a particular crystallite transforms, it will contain domains of both precursor and product. These domains will necessarily be smaller than the original crystallite. Thus, line broadening will result from both the smaller domains and the strain produced in such mixed particle. In the extreme, such effects will cause a disappearance of an X-ray diffraction pattern during the intermediate stage of

a topotactic reaction, but such a disappearance is not evidence that the reaction is not topotactic in nature.

Despite the uniqueness and importance of the vanadium phosphate catalyst for butane oxidation, this catalyst remains poorly understood. Part of the problem is due to the nature of any alkane oxidation reaction. The first step of activating butane is the step that is rate limiting in the overall oxidation reaction. This then precludes studying butane chemisorption or examining reaction intermediates on the surface of the catalyst. However, aside from the difficulty of understanding the mechanism of butane oxidation, there has been a problem of defining the bulk and surface structures and compositions of the catalyst. This catalyst is routinely prepared with a considerable excess of phosphorous, yet there is only a slight excess of phosphorous in the final catalyst. This excess phosphorous is likely at the surface (16). The vanadium oxidation state in a catalyst that has come to steady state in a catalytic reactor is always slightly greater than four. Furthermore, if a VPO catalyst is used to oxidize n-butane in the absence of oxygen, the oxidation state of vanadium is not noticeably lowered by the time at

which selective oxidation ceases (21). This suggests that most of the V^{5+} is not concentrated at the surface.

A discussion of the defects in VPO must first start with a description of the ideal, defect-free structure. Two independent reports of this structure were given in 1979 (22,23). The basic structural features, Figure 3.1, are double V-O chains along the *a*-axis with P_2O_7 groups linking the chains together. Vanadium may be described as octahedrally coordinated to oxygen, but with a strong vanadyl-type distortion. Thus, V-O distances along the *a*-axis alternate long ($\sim 2.36\text{\AA}$) or short ($\sim 1.60\text{\AA}$) with four intermediate equatorial V-O distances ($\sim 1.95\text{\AA}$). The long V-O bond is not shown in Figure 3.1. Thus in Figure 3.1, square pyramidal polyhedra are used to describe the environment around vanadium. These pyramids point either up or down along the *a*-axis. These units share edges in pairs; the apexes of these two pyramids of this pair point opposite directions. The original refinements of the $(VO)_2P_2O_7$ structure did not give completely satisfactory agreement between observed and calculated structure factors, $R \approx 0.09$. Thompson and Ebner (3) have achieved better agreement between observed and calculated structure factors, $R \approx 0.035$, by distributing each vanadium atom over

two different crystallographic sites only 0.2Å apart. Problems with typical $(VO)_2P_2O_7$ crystals have been attributed to defects or disorder. Diffuse spots and streaks have been reported in both electron diffraction and single crystal X-ray diffraction patterns (2,3). We have obtained $(VO)_2P_2O_7$ crystals which give diffraction patterns devoid of streaking effects. This has allowed us to refine the structure to a low R value (4.4%) without introducing any disorder or defects, Chapter 2. We find that the actual space group is monoclinic rather than one of the orthorhombic space groups, $Pcam$, $Pcaa$ or $Pca2_1$, that had been considered previously. Our more precise definition of the ideal structure does not, however, alter the basic structural features of $(VO)_2P_2O_7$ as shown in Figure 3.1.

During the topotactic transformation of $V_2P_2O_9 \cdot xH_2O$ to VPO, there is ample opportunity for stacking faults to occur. The precursor crystal structure is a layered structure with no V-O or P-O bonds bridging the layers. These layers, Figure 3.1, are held together only by van der Waals and hydrogen bonding. As the water is removed during the topotactic reaction, both V-O and P-O bonds form across the layers where there were previously no such bonds. Mistakes can be made as these layers become strongly bound

to each other. The lower the temperature of calcination, the more likely it is that stacking faults occur. This is demonstrated by our DIFFaX calculations, Table 3.1 and Figure 3.1. The *bc* stacking fault can be described as a change in orientation of the vanadyl distortion resulting in a switch from $-V=O-V=O-V=$ chains to $=V-O-V-O=V-$ chains at the stacking fault boundary. At the *ab* fault boundary, the arrangement of edge-shared vanadium octahedra is maintained, however. The major difference being the arrangement of P_2O_7 units. In the ideal unit cell, two adjacent pyrophosphate are oriented in the same direction (Figure 3.2). However, with the addition of the *ab* fault there are now four pyrophosphate neighbors that are aligned in the same direction (Figure 3.3).

The observed vanadium oxidation state increases with decreasing calcination temperature, Table 3.1. This might be attributed either to a higher surface area or to a higher defect concentration. However, the vanadium oxidation state in a VPO catalyst is always higher than 4.00 even after precautions have been taken to avoid an oxidized surface. For example, a VPO catalyst which has been reacted with pure butane until selective oxidation ceases still shows a vanadium oxidation state higher than

4.00. In fact, the oxidation state of vanadium has not changed within the accuracy of the titrations.

Furthermore, we find that the vanadium oxidation state of a given VPO catalyst does not change significantly after equilibration at oxygen fugacities differing by several orders of magnitude. Thus, it seems likely that the amount of V^{5+} in a VPO catalyst is primarily associated with some defect in the bulk, rather than being mainly associated with the surface.

A possible explanation for the presence of some V^{5+} in VPO is that not all $(PO_4)^{4-}$ groups dimerize during the topotatic transformation. This could lead then to a formula of the type $(V_{1-2x}^{4+}V_{2x}^{5+}O)_2(P_2O_7)_{1-x}(PO_4)_{2x}$ at the bc stacking fault. This stacking fault, Figure 3.3, does not allow for the formation of pyrophosphate groups across the fault. If the apical oxygens of the VO_5 square pyramids are not shared between two such units, there is even more excess oxygen and thus more V^{5+} . This stacking fault therefore can readily rationalize all or a substantial fraction of the V^{5+} found in VPO catalysts. Some of the V^{5+} may, of course, be at the surface.

The extended defects found in VPO catalysts may be directly related to its catalytic properties. The best

catalysts are those where this defect is most prominent. This suggests the possibility that the active sites for selective n-butane oxidation are associated with regions where the extended defects meet the surface. Since there is currently no accurate way to determine the number of active sites at the surface, this hypothesis cannot be checked at this time.

3.5 Conclusion

A mechanism shows a possible description of the defects inherent for most VPO catalysts prepared in the laboratory. The two type of faults simulates the observed powder X-ray diffraction, electron diffraction, and single X-ray diffraction data with effectively little or no residuals. The faults themselves could be responsible for the catalytic reactions in converting n-butane to maleic anhydride.

3.6 References

1. G. Centi, F. Trifiro, J.R. Ebner, V.M. Franchetti, *Chemical Reviews*, **88**, 55-80 (1988)
2. E. Bordes, P. Courtine, *J. Catal.*, **57**, 236 (1979)
3. J.R. Ebner and M.R. Thompson, *Studies in Surface Science and Catalysis*, ed. R.K. Grasselli and A.W. Sleight, Elsevier (1992)
4. E. Bordes, Dissertation, Comiegne, France (1979)
5. G. Williamson and W.H. Hall, *Acta Metall.*, **1**, 22 (1953)
6. B.E. Warren and B.L. Averbach, *J. Applied Physics*, **21**, 595 (1950)
7. J.M.M. Treacy, J.M. Newsam, and M.W. Deen, *Proc. R. Soc. Lond. A*, **433**, 499-520 (1991)
8. P.L. Gai and K. Kourtakis, *Science*, **267**, 661 (1995)
9. P.N. Rylander and W.J. Zimmerscheid, U.S. Patent 2,773,921 (1956)
10. A.W. Sleight, *Catal. Today*, **1**, 237-350 (1987)
12. R.M. Contractor, H.E. Bergna, H.S. Horowitz, C.M. Blackstone, U. Chowdhry, and A.W. Sleight, *Catalysis 1987*, Elsevier, 645-654 (1988)
13. R.M. Contractor, H.E. Bergna, H.S. Horowitz, C.M. Blackstone, B. Malone, C.C. Torardi, B. Griffiths, U. Chowdhry, and A.W. Sleight, *Catal. Today* **1**, 49-58 (1987)
14. H.S. Horowitz, C.M. Blackstone, A.W. Sleight, and G. Teufer, *Appl. Catal.*, **38**, 193-210 (1988)
16. G. Bergeret, J.P. Broyer, M. David, P. Gallezot, J.C. Volta, and G.J. Hecquet, *Chem. Soc. Chem. Commune*, 825 (1986)

17. B.K. Hodnett, *Catal. Rev. Sci. Eng.*, **27**, 373 (1985)
18. P. Amoros, R. Ibanez, A. Beltran, D. Beltran, A. Fuertes, P. Gomez-Romero, E. Hernandez, and J. Rodriguez-Carvajal, *Chem. Mater.*, **3**, 407-413 (1991)
19. F. Cavani and F. Trifiro, *Chemtech*, April 1994
20. M.T. Sananes, A. Tuel, G.J. Hutchings, and J.C. Volta, *J. Catalysis*, **148**, 395-398 (1994)
21. R.M. Contractor and A.W. Sleight, *Catal. Today*, **3**, 175-184 (1988)
22. Yu.E. Gorbunova and S.A. Linde, *Sov. Phys. Dokl.*, **24**, 138 (1979)
23. N.E. Middlemiss, doctoral dissertation, Dept. of Chemistry, McMaster Univ., Hamilton, Ontario, Canada (1978)
24. Nakamura, K. Kawai, Y. Fujiwara, *Journal of Catalysis*, **34**, 345 (1974)

Chapter 4

Stability Field for $(VO)_2P_2O_7$

4.1 Introduction

The compound $(VO)_2P_2O_7$ exists at equilibrium only under a certain range of temperature and oxygen fugacity. At higher oxygen fugacity, it will oxidize to $VOPO_4$; at lower oxygen fugacity, it will reduce to VPO_4 . One reason for determining the stability field for $(VO)_2P_2O_7$ is that this then defines equilibrium conditions under which precursor $V_2P_2O_9 \cdot xH_2O$ may be converted to $(VO)_2P_2O_7$. This has more than scientific interest because it relates directly to the commercial production of VPO catalyst. Another reason for determining this stability field is that it then allows us to determine the range of stoichiometry of $(VO)_2P_2O_7$ under equilibrium conditions. The catalytic properties of this phase may well depend on its precise stoichiometry and on any mixed valency or defects related to deviations from ideal stoichiometry.

Over the range of conditions over which the $(VO)_2P_2O_7$ phase is thermodynamically stable, there can be some slight variation in the oxidation state of vanadium, a variation which must be coupled with defects. In this chapter, the

results of our study of the stability field of $(VO)_2P_2O_7$ are presented. We did not observe a phase intermediate between $(VO)_2P_2O_7$ and $VOPO_4$ which had been previously reported, but we did observe a phase intermediate between $(VO)_2P_2O_7$ and VPO_4 .

4.2 Experimental

Samples of $V_2P_2O_9 \cdot xH_2O$ were synthesized by refluxing V_2O_5 with 85% H_3PO_4 (reagent) in a mixture of isobutanol and benzyl alcohol using a P-to-V ratio of 1.2. A typical reaction used 24.7g of H_3PO_4 , 15.6g V_2O_5 , 250ml of isobutanol, and 18ml of benzyl alcohol. After refluxing for 24 hours, the solid $V_2P_2O_9 \cdot 2H_2O$ was separated by vacuum filtration. This product was washed thoroughly with acetone to remove organic residue.

Conversion to VPO was conducted in an oxygen atmosphere controlled furnace at temperatures ranging from 580°C to 800°C. A fugacity probe, composed of 5% yttria-stabilized zirconia, was placed in the reaction chamber but maintained at 1050°C to detect the oxygen fugacity. The probe was calibrated with the Fe/FeO system at the operating temperature of the probe. The fugacity, f , is defined as the effective pressure of the gas at pressure, p . Also by

definition, as $p \rightarrow 0$, then $f \rightarrow p$. The mathematical relationship between f and p is defined by

$$f = \gamma p \quad (4.1)$$

where γ is the fugacity coefficient. γ depends on the identity of the gas, the pressure, and the temperature.

Qualitatively, γ describes the molecular interactions of the gas molecules. If $\gamma > 1$, then $f > p$ so that the repulsive forces between gas molecules contribute to the effective pressure. If $\gamma < 1$, the attractive forces between gas molecules are dominant thus decreasing the real pressure, p . For an ideal gas, $\gamma = 1$. In our experiments, samples were heated until the readings from the fugacity probe were constant and this is our definition of "apparent" equilibrium.

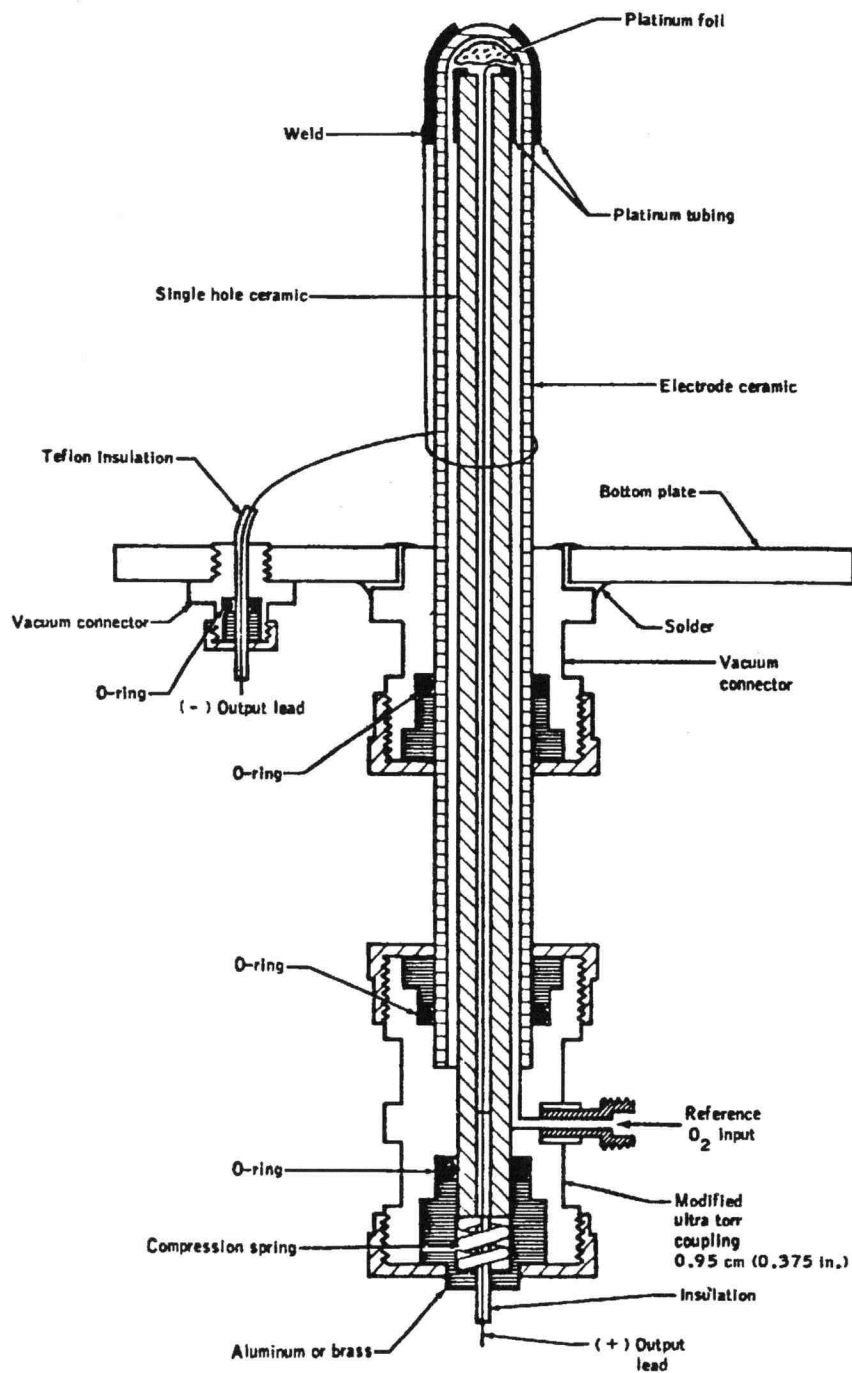


Figure 4.1. Schematic design of fugacity probe

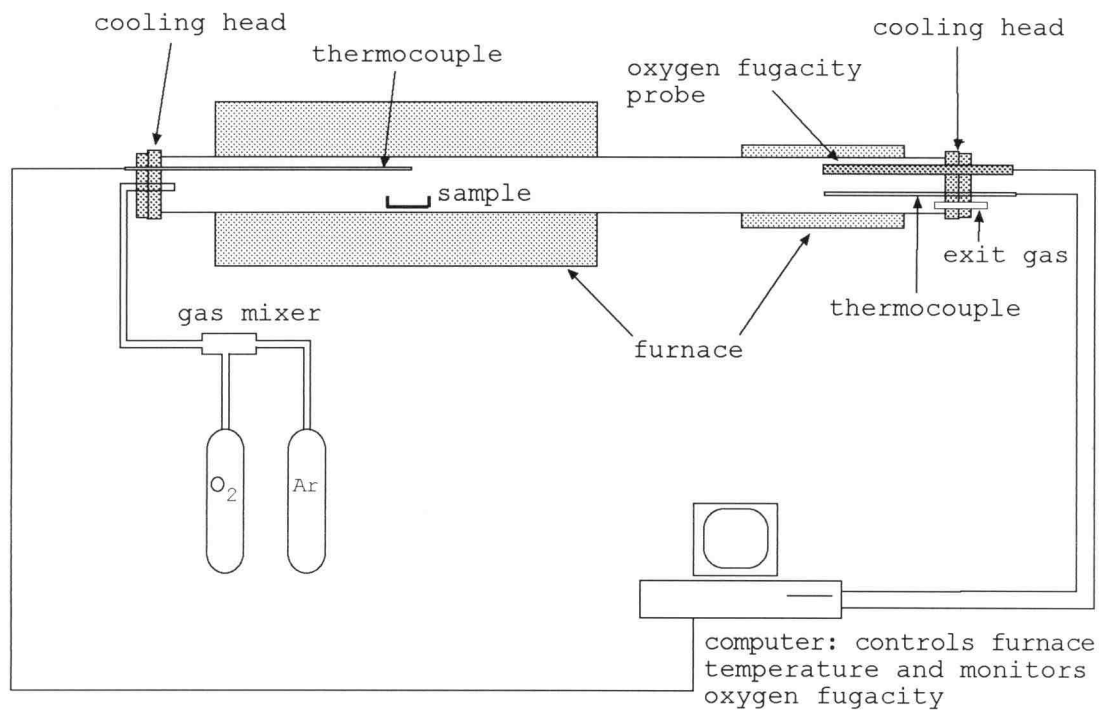


Figure 4.2. Schematic of fugacity furnace design

The oxygen partial pressure was controlled with mixtures of Ar and O₂ or with Ar mixed with Ar/10%H₂ gas. For a typical cylinder of "pure Ar", a measured oxygen fugacity is 1.26×10^{-3} atm; with the Ar/10%H₂ mixture, a representative fugacity measured is 1.0×10^{-11} atm. The design of the furnace is similar to the one presented by Williams and Mullins of NASA (16). Figure 4.1 is an outline of the fugacity probe, and Figure 4.2 is the diagram of the actual setup used in this work. Vanadium oxidation states were determined by a method similar to the one introduced by Nakamura (17), chapter 5.

4.3 Results and Discussion

Apparent equilibrium was achieved in as quickly as 12 hours for samples prepared at relatively high temperature (790°C and 705°C) and as slow as 6-7 days for the samples prepared at lower temperatures (580°C). For samples prepared at 645°C, apparent equilibrium was achieved after 3-4 days. The average vanadium oxidation state is plotted against the log of the oxygen partial pressure for various temperatures in Figure 4.3.

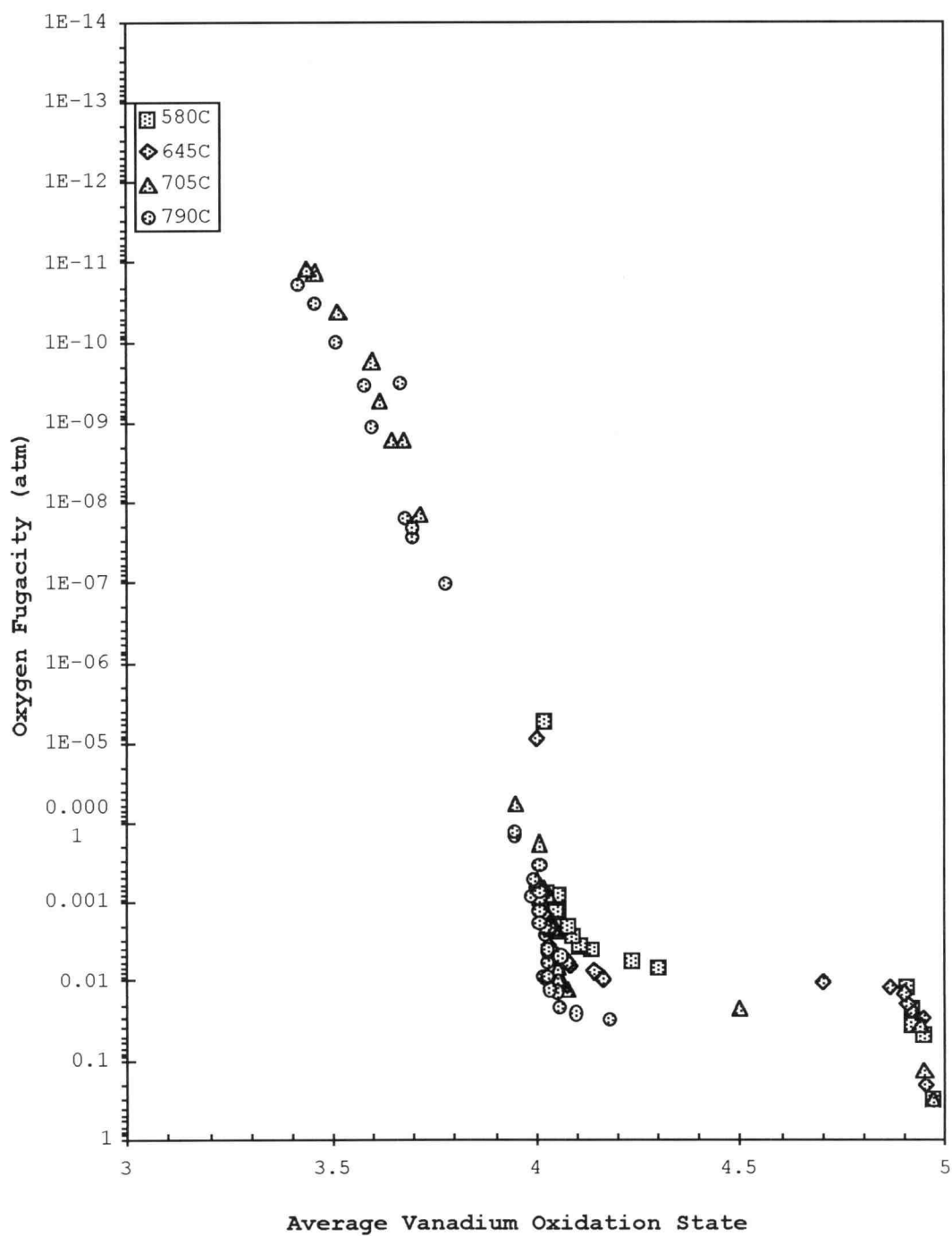


Figure 4.3. Plot of stability region for VPO as a function of the log of the oxygen fugacity and temperature.

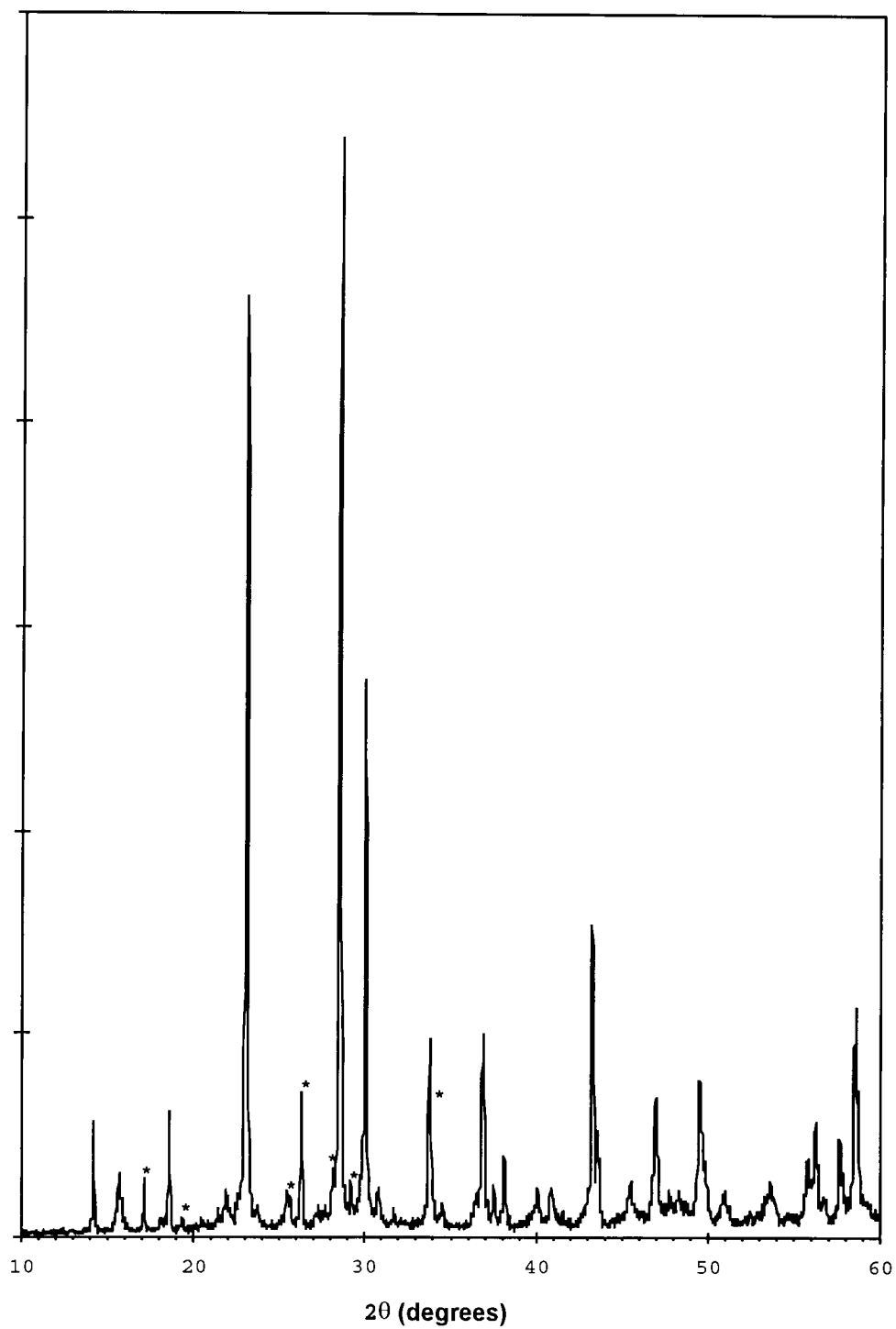


Figure 4.4. X-ray powder pattern of a mixture of VPO and β -VPO₅ for a sample prepared at 705°

For samples prepared at 790°C, single phase VPO was observed from 6.48×10^{-4} atm to 2.09×10^{-2} atm. Above the latter value, β -VPO₅ phase was observed in X-ray powder patterns, Figure 4.4. Samples prepared at 790°C and with an oxygen fugacity greater than 3.1×10^{-2} atm melted. This is presumably due to melting of β -VPO₅ which is known to occur at that temperature.

For samples prepared at 705°C, single phase VPO was observed from 6.31×10^{-4} to 1.26×10^{-2} atm of oxygen. For samples prepared at 645°C, the stability region for single phase VPO was from 1.31×10^{-3} to 4.79×10^{-3} atm of oxygen. For samples prepared at 580°C, the stability region for single phase VPO was from 1.91×10^{-3} to 5.01×10^{-3} atm of oxygen. Similar to results at 790°C, if these samples were prepared at a higher oxygen fugacity, a mixture of VPO and β -VPO₅ was observed in the X-ray powder patterns, Figure 4.4. No melts were ever observed for samples prepared at these lower temperatures. For samples prepared at 705°C with an oxygen fugacity value of 3.80×10^{-2} atm or more, single phase β -VPO₅ samples were observed. For samples prepared at 645°C,

Table 4.1
Data for unknown V(III)/V(IV) Phase

hkl	Calc. d-value (Å)	d-value of unknown phase (Å)
0 1 0	7.120	7.126
2 0 0	6.501	6.503
-2 0 1	6.135	6.132
1 0 2	5.354	5.337
2 1 0	4.800	4.800
2 0 2	4.222	4.221
-1 0 3	4.148	4.145
-2 0 3	3.762	3.768
2 1 2	3.631	3.630
-3 0 3	3.244	3.237
-2 2 1	3.079	3.077
2 1 3	2.999	3.003
2 2 1	2.983	2.987
-1 0 5	2.526	2.522

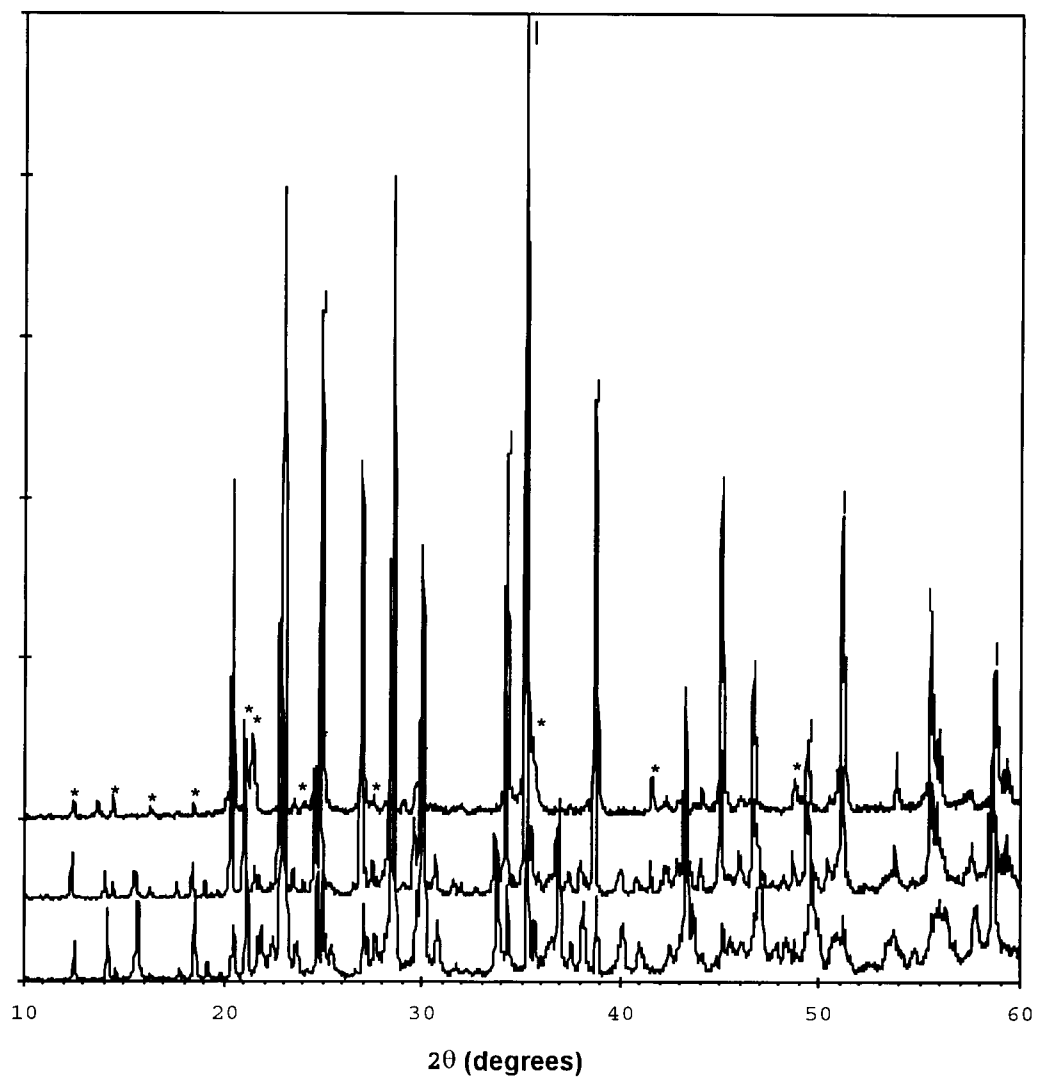


Figure 4.5. a) X-ray powder pattern of VPO, VPO_4 (|), and unknown phase (*). b) Same as a except there is less of VPO. c) X-ray powder pattern of VPO_4 and unknown phase.

anything above 2.75×10^{-2} atm of oxygen resulted in single phase β -VPO₅ as the product. This boundary for single phase β -VPO₅ changed to 1.26×10^{-2} atm or more for samples prepared at 580°C.

For the conversion of VPO \rightarrow VPO₄, an interesting phenomenon was noticed. Below 1.0×10^{-4} atm of oxygen for samples prepared at 790°C and 5.01×10^{-5} atm of oxygen for samples prepared at 705°C, a new intermediate phase was observed to exist in apparent equilibrium between VPO and VPO₄, Figure 4.5. This phase was present to as low as 1.0×10^{-11} atm of oxygen. Preparation of single phase samples of this new compound was never successful. The unknown compound always existed in the presence of VPO and/or VPO₄. There were 14 distinguishable peaks, Table 4.1, in the X-ray diffraction pattern that could not be matched to any known compounds in the V-P-O system. However, the unknown peaks could be indexed as monoclinic with lattice constants of $a = 13.1332\text{\AA}$, $b = 7.1201\text{\AA}$, $c = 12.6249\text{\AA}$, and $\beta = 98.115^\circ$. At relatively high oxygen partial pressures, the new phase was present with both VPO and VPO₄, but as the oxygen fugacity was decreased only VPO₄ and the new phase were evident in the X-ray powder patterns. The new phase is believed to be composed of mixed V³⁺ and V⁴⁺ because titrations of samples

containing this phase always showed an oxidation state for vanadium somewhat higher than three.

The transition from VPO to VPO_4 does not occur as sharp as the transition from VPO to β - VPO_5 . The time to achieve apparent equilibrium was very lengthy, ranging from 36 hours to as much as 70 hours. The lower the oxygen fugacity, the longer it took to achieve apparent equilibrium.

If our samples were at true equilibrium, then from the phase rule only one phase with P/V ratio equal to one should be present at a particular temperature and oxygen fugacity. However, some of our samples showed two phases at apparent equilibrium. There are several possible explanations of this behavior. At one precisely fixed temperature and oxygen fugacity, two phases can be present in equilibrium, but this argument can be rejected because we observed the presence of more than one phase over a variation of oxygen fugacity. However, if our apparent equilibrium is not true equilibrium, violations of the phase rule could occur. In our experiments, apparent equilibrium was defined as fugacity readings reaching constant values. This does not necessarily mean we are at true chemical equilibrium. However, because no hysteresis was observed on transforming back and forth between VPO and β - VPO_5 , apparent equilibrium would seem to be

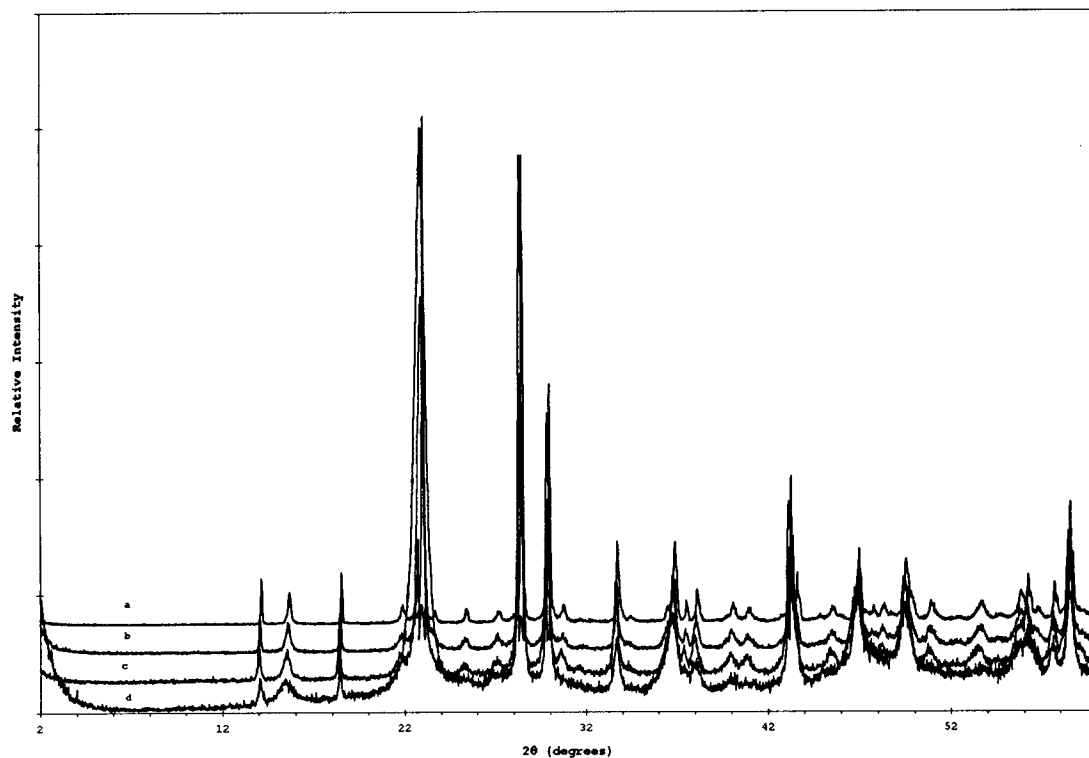


Figure 4.6. X-ray powder patterns for VPO prepared at the same oxygen fugacity but different temperatures: a) 790°C, b) 705°C, c) 645°C, and d) 585°C.

close to true equilibrium. Samples and phases were assumed to have a 1:1 ratio of V to P. If this ratio is not fixed at 1:1, two phases could coexist at true equilibrium, but the P/V ratio would not be exactly one in at least one of the phases. Relevant to this explanation is the fact that VPO catalyst and the VPO samples prepared in this work have a P to V ratio slightly greater than 1.0.

Some of the trends observed are in agreement with those reported by Bordes et al. (15) in a study of the conversion between β -VPO₅ and VPO above 700°C. In their work, hysteresis was observed for the reoxidation of VPO to β -VPO₅ and a single phase intermediate compound identified as VPO_{4.75} was observed. We observed no significant hysteresis nor an intermediate compound, we see only a steep plateau separating the two different compounds of V⁺⁴ and V⁺⁵ phases. At intermediate oxygen fugacities, mixtures of vanadium(IV) and vanadium(V) compounds were present in their X-ray powder patterns. Also, in their work there was evidence of mixed phases consisting of VPO and VO(PO₃)₂ which suggests that they were not operating at a P/V ratio of one.

Figure 4.6 presents the XRD patterns of four samples prepared at different temperatures but the same oxygen fugacity, 2.51×10^{-3} atm. There is a definite decrease in

peak widths as the temperature is increased. This is most noticeable for the peak around 16° two theta, indexed as the (111) reflection. The average vanadium oxidation states also shows a decreasing trend from 4.082 for the samples prepared at the lowest temperatures to 4.025 for the sample prepared at 790°C . This suggests that the defect causing the broadening of the 111 peak incorporates extra oxygen.

The highest value we found for the vanadium oxidation state in $\beta\text{-VPO}_5$ was 4.97, not 5.00 as expected. It may be relevant that $\beta\text{-VPO}_5$ is isostructural with $\beta\text{-VSO}_5$. In the former case, vanadium is in an oxidation state of +5 but in the latter case it is in an oxidation state of +4. This suggests that our samples of $\beta\text{-VPO}_5$ could have some sites, 5% on average, where vanadium is in an oxidation state of +4 which could be compensated for with oxygen vacancies.

The degree of crystallinity trend also follows predictions since higher temperatures promotes greater amount of crystal growth, i.e. the sharpening of peaks. Table 4.2 illustrates this fact based on measurements with the peak at 23° two-theta, the (200) reflection, for samples prepared at different temperatures and oxygen fugacities.

Table 4.2

Data for samples prepared at different temperatures and constant oxygen fugacity

Temperature (°C)	FWHM of 200 peak(2 θ)	Crystallite Size (nm)	Strain
580	.4743	18.6	1.09×10^{-2}
645	.3050	31.2	8.48×10^{-3}
705	.1016	119.7	2.57×10^{-3}
790	.0963	122.8	2.20×10^{-3}

Table 4.3

Data for samples prepared from low to high oxygen fugacity

Oxygen Fugacity (atm)	Average V Oxidation state	FWHM(111) 2θ	*Particle Size (nm)	Strain
2.70×10^{-3}	4.025	.1674	45.6	1.47×10^{-3}
4.30×10^{-3}	4.023	.1494	52.4	1.27×10^{-3}
9.10×10^{-3}	4.018	.1352	60.4	1.43×10^{-3}
3.20×10^{-2}	4.023	.1335	61.1	1.35×10^{-3}

*All samples prepared for 14 hours in the furnace

Table 4.4

Data for samples prepared from high to low oxygen fugacity

Oxygen Fugacity (atm)	Average V Oxidation state	FWHM(111) 2θ	*Particle Size (nm)	Strain
1.45×10^{-2}	4.037	.2331	35.6	4.76×10^{-3}
1.00×10^{-2}	4.026	.1990	37.6	2.01×10^{-3}
6.00×10^{-3}	4.023	.1999	38.8	2.80×10^{-3}
2.20×10^{-3}	4.023	.1945	40.7	2.97×10^{-3}

*All samples prepared for 14 hours in the furnace

When one sample was equilibrated at a low oxygen fugacity, Table 4.3, and then calcined with increasing oxygen fugacities, the vanadium oxidation state did not change but was rather constant throughout the range of 0.0027-0.032 atm. The average oxidation state of vanadium measured was 4.022. The average crystallite size increase observed going down the Table 4.3 is presumably due to the increased time of calcination. The strain measured with the Warren-Averbach (18) method shows little variation. When starting with a sample at high oxygen fugacity, Table 4.4, at 3.23×10^{-2} atm the average vanadium oxidation state measured was 4.037 with a low particle size and high strain, 356Å and 4.76×10^{-3} respectively. However as the oxygen atmosphere is reduced, the vanadium oxidation state stabilized along with the size and strain.

The main differences between Table 4.3 and Table 4.4 is not in the oxidation state but in the size and the strain of crystallites in the sample. The average crystallite sizes for high-to-low oxygen content samples, Table 4.4, are always smaller for the low-to-high oxygen content samples, Table 4.3. This effect is clearly seen for the strain measurements as well as the breadth (FWHM) of the 111 peak. When samples are first prepared with low oxygen partial pressures, the

breadth of the 111 peak and strain is smaller and the changes are negligible from sample to sample. However when the samples are first equilibrated at a high oxygen partial pressure, the immediate product has the highest strain which then slowly decreases when the oxygen content is decreased. This behavior can be attributed to two effects, length of calcination as well as oxygen fugacity. From analysis of data in Table 4.3, it seems that the calcination time is the most important factor since the vanadium oxidation state varies only slightly with differing oxygen fugacity.

4.4 Conclusions

Single phase VPO samples showed a significant variation of average vanadium oxidation state at apparent equilibrium in controlled oxygen firing conditions. Values from as high as 4.10 at 580°C to as low as 4.00 are present for apparent single phase products. No intermediate phase between VPO and β -VPO₅ was found that could account for this effect.

Therefore, some defect must be present at the atomic level to account for the increase in oxygen content and explain this unusual behavior, chapter 3.

The appearance of a new phase containing both V^{3+} and V^{4+} is very interesting and deserves closer examination. A single phase sample of this material should be prepared and characterized. Attempts with varying partial pressures of oxygen and temperatures have failed to give a single phase product. Varying the ratio of V:P along with the variables stated above could be promising.

One aspect of this research that could have important practical applications is that removal of organic residue prior to dehydration of $V_2P_2O_9 \cdot xH_2O$ leads to a much faster and better controlled conversion to catalyst. Any organic matter not removed can serve to reduce some V^{4+} to V^{3+} leading to two phase products.

Single phase VPO was the equilibrium phase under oxygen fugacities close to 10^{-2} atm of oxygen for a wide range of temperatures. Commercial applications using pure CO_2 or H_2O at $400^\circ C$ could be a convenient way to achieve this desired fugacity. No hysteresis was observed on cycling between $(VO)_2P_2O_7$ and $VOPO_4$, and no phase intermediate between these two phases was observed.

4.5 References

1. *Chemical and Engineering News*, November 4 1994
2. G. Centi, F. Trifiro, J.R. Ebner, and V.M. Franchetti, *Chem. Rev.*, **88**, 55, (1988)
3. B.S Schiott, K.A. Jorgensen, and R. Hoffmann, *J. Phys. Chem.*, **95**, 2297, (1991)
4. F. Rouvet, J.M. Herrmann, and J.C. Volta, *J. Chem. Soc. Faraday. Trans.*, **90**, 1441, (1994)
5. E. Bordes, P. Courtine, and J.W. Johnson, *J. Solid State Chem.*, **55**, 270, (1984)
6. H.S. Horowitz, C.M. Blackstone, A.W. Sleight, and G. Teufer, *Applied Catalysis*, **38**, 193, (1988)
7. L.M. Cornaglia, C. Caspani, and E.A. Lombardo, *Applied Catalysis*, **74**, 15, (1991)
8. B.K. Hodnett, Ph. Permann, and B. Delmon, *Applied Catalysis*, **6**, 231, (1983)
9. D. Ye, A. Satsuma, T. Hattori, and Y. Murakami, *Applied Catalysis*, **69**, L1, (1991)
10. M.L. Granados, J.C. Conesa, and F. Garcia, *Journal of Catalysis*, **141**, 671, (1993)
11. D.B. Porter, A.B. Porter, P. Amoros, R. Ibanez, and E. Martinez, *Eur. J. Solid State Inorg. Chem.*, **28**, 131, (1991)
12. P. Amoros, R. Ibanez, A. Beltran, D. Beltran, A. Fuertes, P.G. Romero, E. Hernandez, and J.R. Carvajal, *Chem. Mater.*, **3**, 407, (1991)
13. C.C. Torardi, J.C. Calabrese, *Inorg. Chem.*, **23**, 1308, (1984)
14. F. Cavani, F. Trifiro, *Chemtech*, April 1984

15. E. Bordes, P. Courtine, and J.W. Johnson, *J. of Solid State Chem.* , **55**, 270 (1984)
16. R.J. Williams and O. Mullins, *NASA Technical Memorandum 58234*, (1981)
17. M. Nakamura, K. Kawai, Y. Fujiwara, *J. Catalysis*, **34**, 345 (1974)
18. B.E. Warren, B.L. Averbach *J. Applied Physics*, **21**, 595 (1950)

Chapter 5

Analysis of Diffraction Patterns on Real VPO Catalysts

5.1 Introduction

The VPO materials discussed in the earlier chapters of this thesis were not prepared according to the conditions normally used to prepare VPO catalysts. We added two features to the synthesis in order to obtain higher reproducibility and more homogeneous products. One feature was to wash organic residue from the precursor before its dehydration. The other feature was to conduct the topotactic dehydration under controlled oxygen fugacity. Samples described in this chapter were prepared by dehydration of the precursor in air. For the samples prepared at OSU, there was still a wash of the precursor to remove organics. However, some VPO catalysts were prepared at DuPont and there was no precursor wash to remove organics for such samples. Furthermore, the VPO samples obtained from DuPont had generally been in a catalytic reactor for several days. The focus of this chapter is then to examine "real" VPO

catalysts, catalysts prepared in a more traditional, uncontrolled manner and actually used as catalysts.

In this chapter, we evaluate only X-ray diffraction powder patterns. The effects of the extended defects described in chapter 3 are ignored, and the peaks most effected by these extended defects are ignored. Instead, we focus on the effects of particle size and especially strain on selected strong peaks. The primary objective of this analysis is to define a method to distinguish between good and bad catalysts. Such catalysts were obtained from DuPont, and the "good" or "bad" label is based on their evaluations in catalytic reactors.

5.2 Experimental

For samples described in this particular chapter, finely ground V_2O_5 (99.99% Aesar) was refluxed for 8-24 hours with H_3PO_4 (FMC, reagent) in isobutanol or *t*-butanol and benzyl alcohol mixture at 80°C to 100°C depending on the starting alcohol used. If *t*-butanol was used, then the reaction was maintained at the boiling point of *t*-butanol, 80°C. The starting P-to-V ratio was kept at 1.45 because it has been shown that excess phosphorous gives products with better catalytic activity (1). Three concentrations of phosphoric

acid that were used: 85%, 105%, and 117%. For samples where the concentration of acid was above 100%, *t*-butanol was used as the solvent. (If prepared with isobutanol, the product formed was identified as vanadyl phosphonate with a small fraction of the desired precursor phase.) After separation of the solid from the solution by vacuum filtration, the precursor was vacuum dried at 100°C for at least 12 hours.

The conversion from precursor to catalyst was performed by taking the light blue solid precursor and calcining in air at temperatures between 380°C to 500°C in a muffle furnace for times ranging from one hour to a maximum of 16 hours. The product after calcination was predominantly VPO with β -VPO₅ impurities appearing if the time of calcination was long (usually greater than 14 hours) or the temperature was high (greater than 500°C).

Precursors were washed with acetone to remove organic residues that might remain within the sheets or adhered to surface of the powder. GC-MS experiments were performed on a HP 5890 Series II GC and a HP 5971 MS spectrometer with the washed solution in order to determine the quantity and type of organics associated with the precursor solid.

Approximate water solubility for the precursor was determined by stirring a known amount of sample in a fixed

volume of water for one hour followed by a filtration and drying. The difference in weight before and after filtration was taken as the amount of soluble material.

X-ray powder patterns were taken on a Siemens D5000 diffractometer using $\text{CuK}\alpha$ radiation. Average vanadium oxidation states were determined by a method similar to the one introduced by Nakamura (2). Usually 0.5-1.0g samples of VPO were dissolved in 50ml 18N H_2SO_4 at 150°C . Then the solution was removed from the heat source, and an additional 150ml $\text{HBO}_3/\text{H}_2\text{SO}_4$ solution was then added to dilute the sample volume to 200ml. The oxidation of all vanadium species to +5 was carried out by titrating with a 0.100N KMnO_4 standard solution, the volume used is directly related to the amount of vanadium in a reduced state either V^{+3} or V^{+4} . Then a reduction to vanadium +4 was performed with a 0.100N $\text{Fe}(\text{NH}_4)_2(\text{SO}_4)_2$ standard solution with the volume used being equal to the total amount of vanadium +5 in solution. The average vanadium oxidation state can be calculated by the following equation:

$$\text{Ave. V oxid. state} = 5 - [\text{vol. of KMnO}_4/\text{vol. of Fe(II)}] \quad (5.1)$$

Evaluation of strain and crystallite was accomplished with the Siemens software based on the Warren-Averbach method (3).

5.3 Results

There were appreciable differences in the X-ray powder pattern of the precursors when varying the reflux time. For samples prepared with 85% phosphoric acid, obtaining the final product was much faster than when using 105% and 117% H_3PO_4 . The temperature of the reaction was the most likely source of this effect, 100°C for 85% H_3PO_4 versus 80°C for samples prepared with a phosphoric acid concentration greater than 100%. Precursors were easily obtained after only 3 hours of reflux for samples prepared with 85% H_3PO_4 but required at least 9 hours for samples prepared with 105% and 117% H_3PO_4 . X-ray powder patterns of precursor samples prepared at a refluxing time of 12 hours are shown in Figure 5.1 for different starting phosphoric acid concentrations. The products are predominantly single phase $\text{V}_2\text{P}_2\text{O}_9 \cdot 2\text{H}_2\text{O}$ with some minor impurities of $\text{VO}(\text{H}_2\text{PO}_4)_2$, identified by (*). The progression from samples prepared with low concentration

phosphoric acid to samples prepared with more concentrated acid shows systematic changes in the diffraction patterns. Peaks with *l*-components are significantly broader than *hk0* peaks for samples prepared with 105% and 117% H_3PO_4 samples. This can be ascribed to the highly anisotropic dimensions of the crystallites. A comparison between the samples prepared with 85% H_3PO_4 made with isobutanol or *t*-butanol shows that the two samples are similar in particle size and full width at half maximum (FWHM) for the 001 peak, Table 5.1. GC-MS measurements performed on the washed precursors showed only the solvent peaks, isobutanol or *t*-butanol, plus benzaldehyde. There was no indication of other compounds in the washed solution.

Table 5.1

 $V_2P_2O_9 \cdot 2H_2O$ Data

Sample	Percent Organic residue	Percent Water Solubility	FWHM of 001 Peak (2θ)	Crystallite Size (nm)	Strain
85% H_3PO_4 , isobutanol	5.8%	9%	.1130	75.7	.00104
85% H_3PO_4 , <i>t</i> -butanol	8.8%	20%	.1369	75.3	.00351
105% H_3PO_4 , <i>t</i> -butanol	6.8%	12%	.2790	33.4	.00768
117% H_3PO_4 , <i>t</i> -butanol	4.2%	17%	.3179	24.6	.00671

One-dimensional strain in solids is defined as $\Delta d/d_0$, where Δd is the amount of amount of change from the original lattice constant, d_0 . The effects of strain on the overall X-ray peak can be seen in Figure 5.2. For uniform strain, the only observed difference is the shift in peak position from the original 2θ value to a lower one if the strain were to increase the lattice constant or a larger 2θ value if the strain were to decrease the lattice constant. For nonuniform strain, the major difference from the original peak is the increase in peak breadth. If a combination of uniform and nonuniform strain were to occur in solid samples, the expected outcome would be a peak shift and peak broadening to compensate for strain (4). Therefore, for these precursors, if any organic molecules were to be trapped within the sheets, one would expect to see either a peak shift or a combined peak shift and peak broadening. This is clearly evident for the 001 peak, the direction of layer stacking, in Figure 5.1. A comparison for samples prepared with 85% H_3PO_4 and those of higher acid concentrations shows that for samples of lower acid concentrations, the 001 peak is relatively sharp and intense, showing a minimal amount of

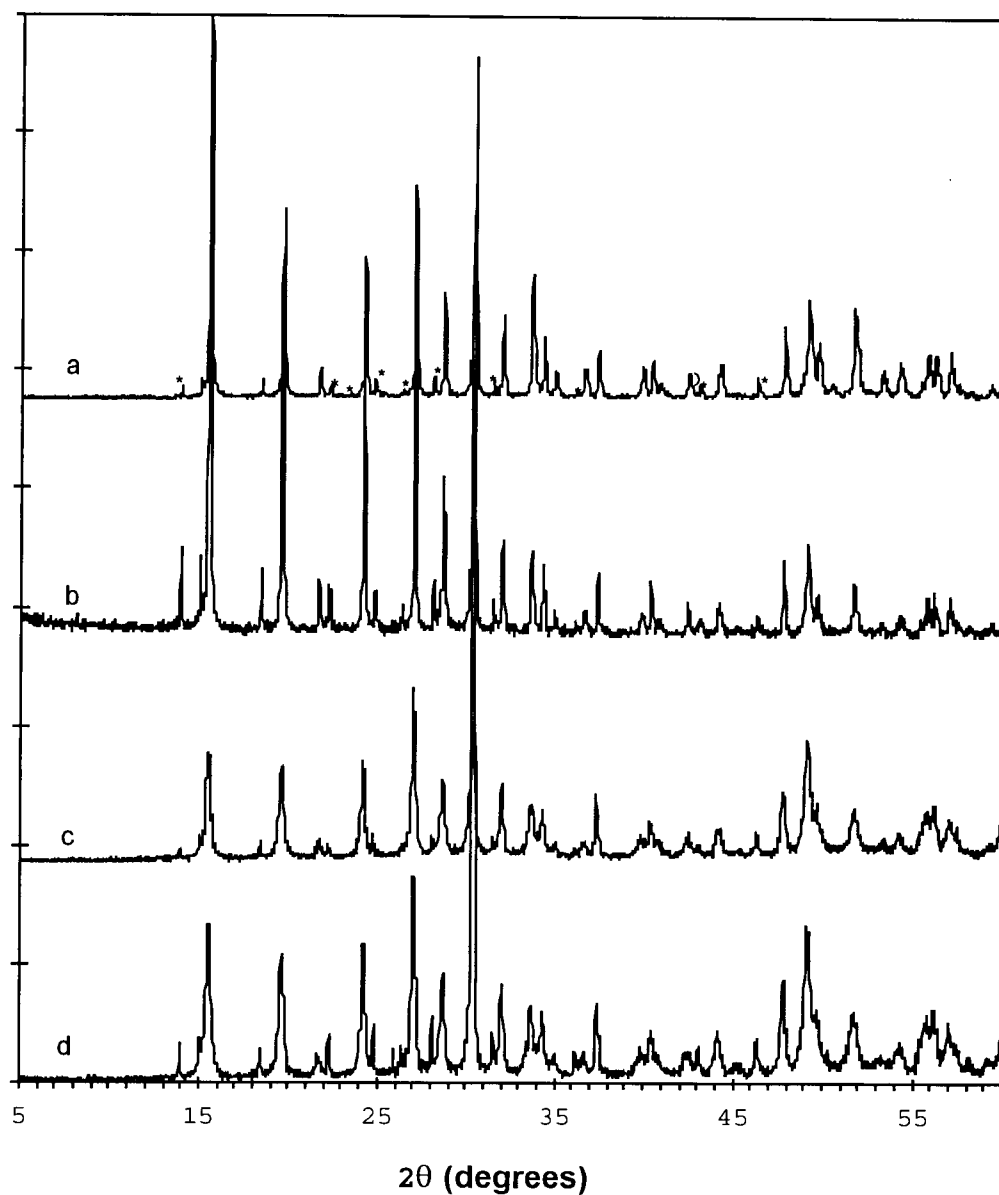


Figure 5.1. X-ray powder patterns of $V_2P_2O_9 \cdot 2H_2O$ after 12 hours of reflux with benzyl alcohol. a) prepared with 85% H_3PO_4 and isobutanol. b) prepared with 85% H_3PO_4 and *t*-butanol. c) prepared with 105% H_3PO_4 and *t*-butanol. d) prepared with 117% H_3PO_4 and *t*-butanol.

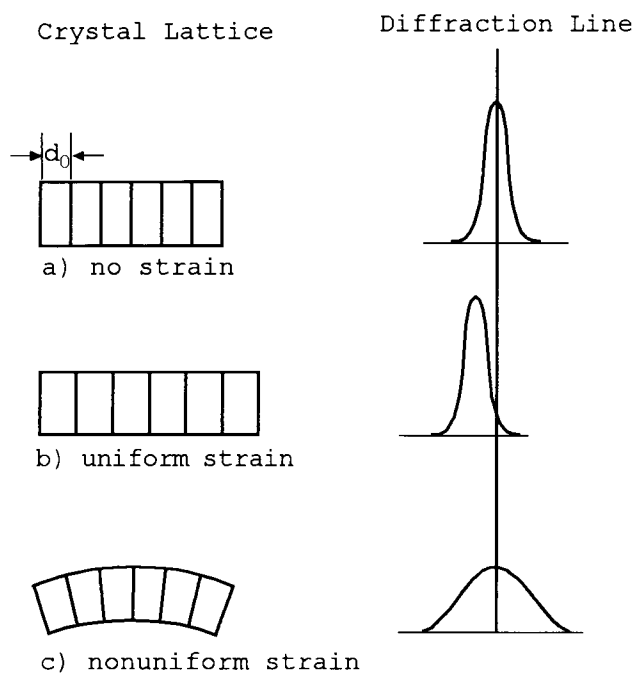


Figure 5.2. How strain affects the appearance and position of the diffraction peak.

variance between *t*-butanol and isobutanol prepared samples. However, as the concentration of acid increases, the 001 peak slowly broadens. This would suggest that there might be some source of organic residues trapped between the sheets of the sample. A comparison of samples prepared with *t*-butanol but with different starting phosphoric acid concentrations shows that when using higher acid concentration, the product crystallite sizes are much smaller relative to the samples prepared with lower acid concentration. The strain also increases as the acid concentration is increased but stabilizes on going from 105% to 117% H₃PO₄. The amount of organic residue is decreasing from 8.8% for 85% H₃PO₄ prepared samples to 4.2% for 117% H₃PO₄ prepared samples, Table 5.1. Water solubility of the precursors is lowest for the 85% H₃PO₄ prepared samples made with isobutanol, and the highest organic amount is for the 85% H₃PO₄ samples prepared from *t*-butanol solvent. These results along with X-ray powder diffraction data seem to confirm the idea of the organic solvent being trapped in between the precursor layers.

The X-ray diffraction patterns of the catalysts converted from precursor at 400°C are shown in Figure 5.3. All the peaks can be indexed as belonging to VPO. A small impurity phase identified as VOPO₄·xH₂O is evident for pattern

b. Peaks with h-components are significantly broader than 0kl peaks. However, similar to the precursors, the peak widths broaden for samples prepared with increasing concentration of phosphoric acid. The data shown in Figure 5.3 indicate that using *t*-butanol as the solvent gives samples showing a broader h00 reflection, Table 5.2. This is presumably related to an enhancement exposure of the crystallographic face considered by some to be most desired for selective oxidation of n-butane. Similar to the respective precursors, the strain increases with increasing acid concentrations used in synthesis, Table 5.2.

X-ray diffraction patterns were obtained with Si in order to obtain high absolute accuracy for the unit cell dimensions. The primary focus was on the 200 peak because this is a strong peak which shows both line broadening and shifts in position. Figure 5.4 shows a plot of the corrected a lattice constant for catalysts removed from the reactor at different times. These samples were supplied by DuPont. There is a trend toward decreasing a lattice constant as the time in the reactor increases. The strain in the catalysts appears first very high for day 0, 0.0255, but then approach an average value of 0.0155 as the catalyst ages in the reactor, Table 1.5. The crystallite size of the samples

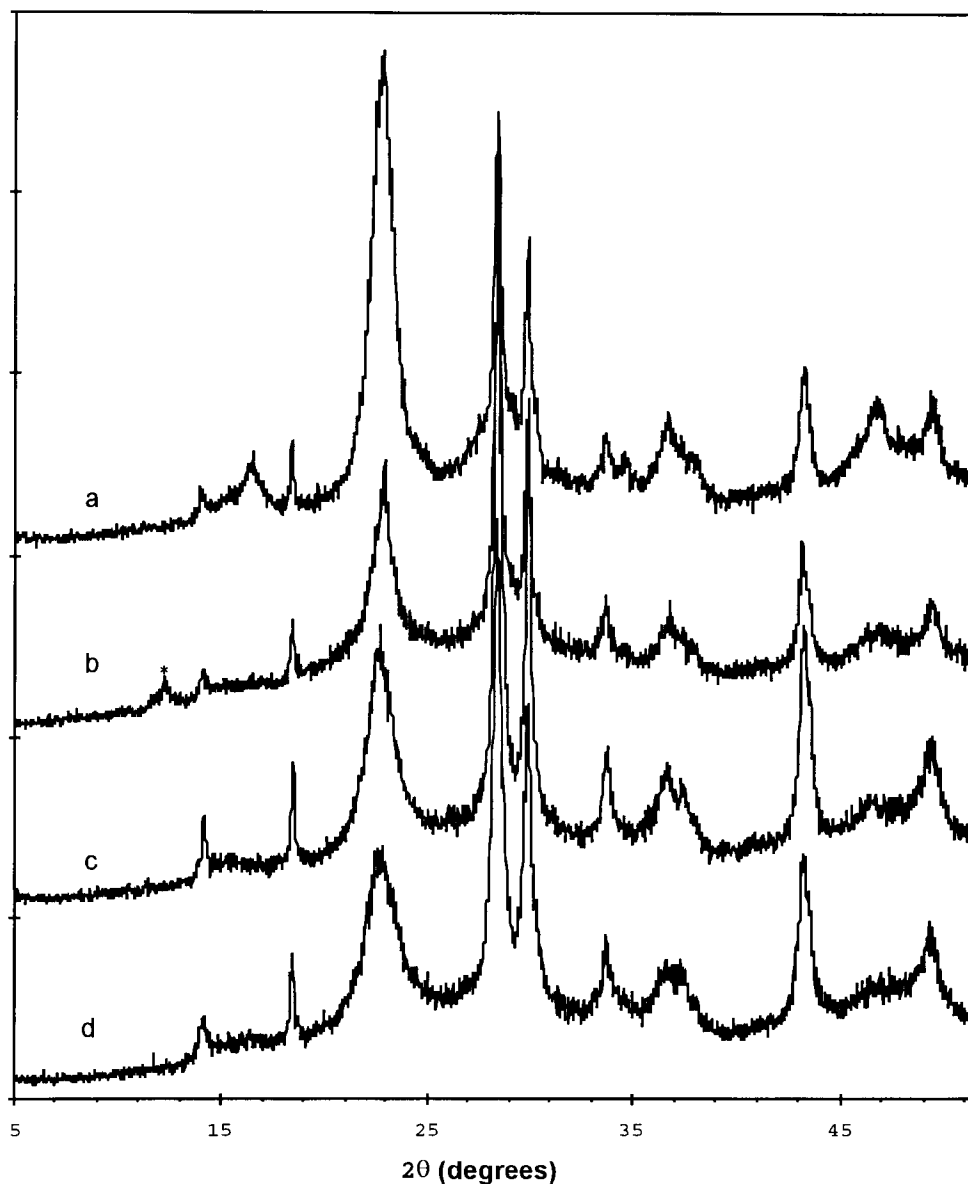


Figure 5.3. X-ray powder patterns of VPO from calcination of precursors in air at 400°C for one hour. a) precursor prepared with 85% H_3PO_4 and isobutanol, b) precursor prepared with 85% H_3PO_4 and *t*-butanol, c) precursor prepared with 105% H_3PO_4 and *t*-butanol, and d) precursor prepared with 117% H_3PO_4 and *t*-butanol. (*) $\text{VOPO}_4 \cdot x\text{H}_2\text{O}$ impurity from extended exposure to air.

Table 5.2

VPO Data

Sample	FWHM for 200 peak (2θ)	Particle Size (nm)	Strain
85% H_3PO_4 , isobutanol	1.1652	15.5	.04600
85% H_3PO_4 , <i>t</i> -butanol	1.4070	10.7	.04620
105% H_3PO_4 , <i>t</i> -butanol	1.4603	14.5	.05777
117% H_3PO_4 , <i>t</i> -butanol	1.7018	26.1	.07800

Table 5.3
Data for DuPont VPO Samples

Sample	FWHM for 200 peak (2θ)	Particle Size (nm)	Strain
day 0	.7673	15.8	.02555
day 10	.6721	13.5	.0143
day 29	.6230	15.0	.0149
day 43	.5793	18.4	.0177
day 50	.6247	14.1	.01289
day 60	.5615	19.5	.0179
good	.9992	12.1	.03048
medium	.7459	12.8	.0173
bad	.6497	16.0	.0188

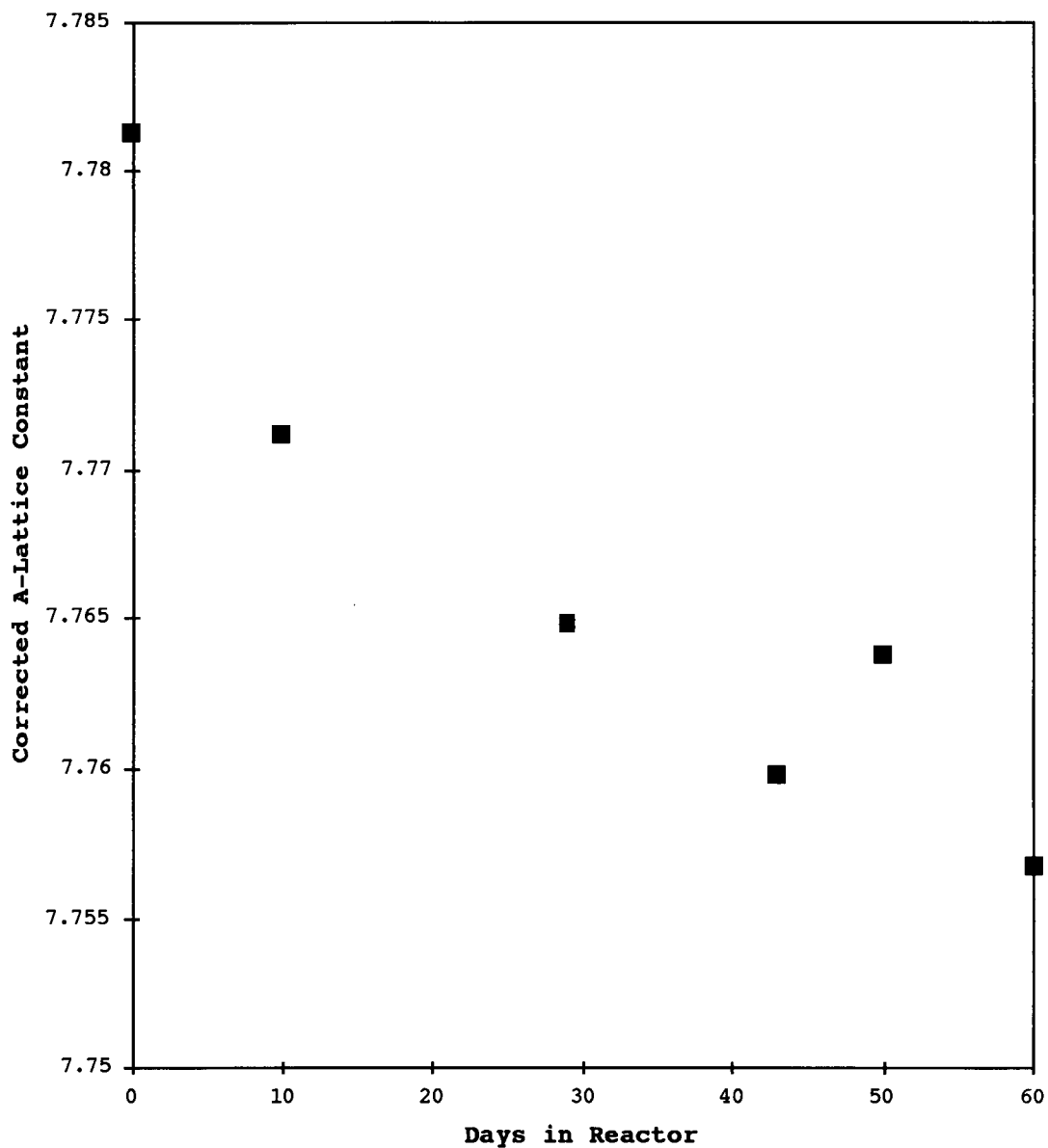


Figure 5.4. How lattice constants varies as a function of time in laboratory reactor for spent catalysts. Samples were supplied from DuPont.

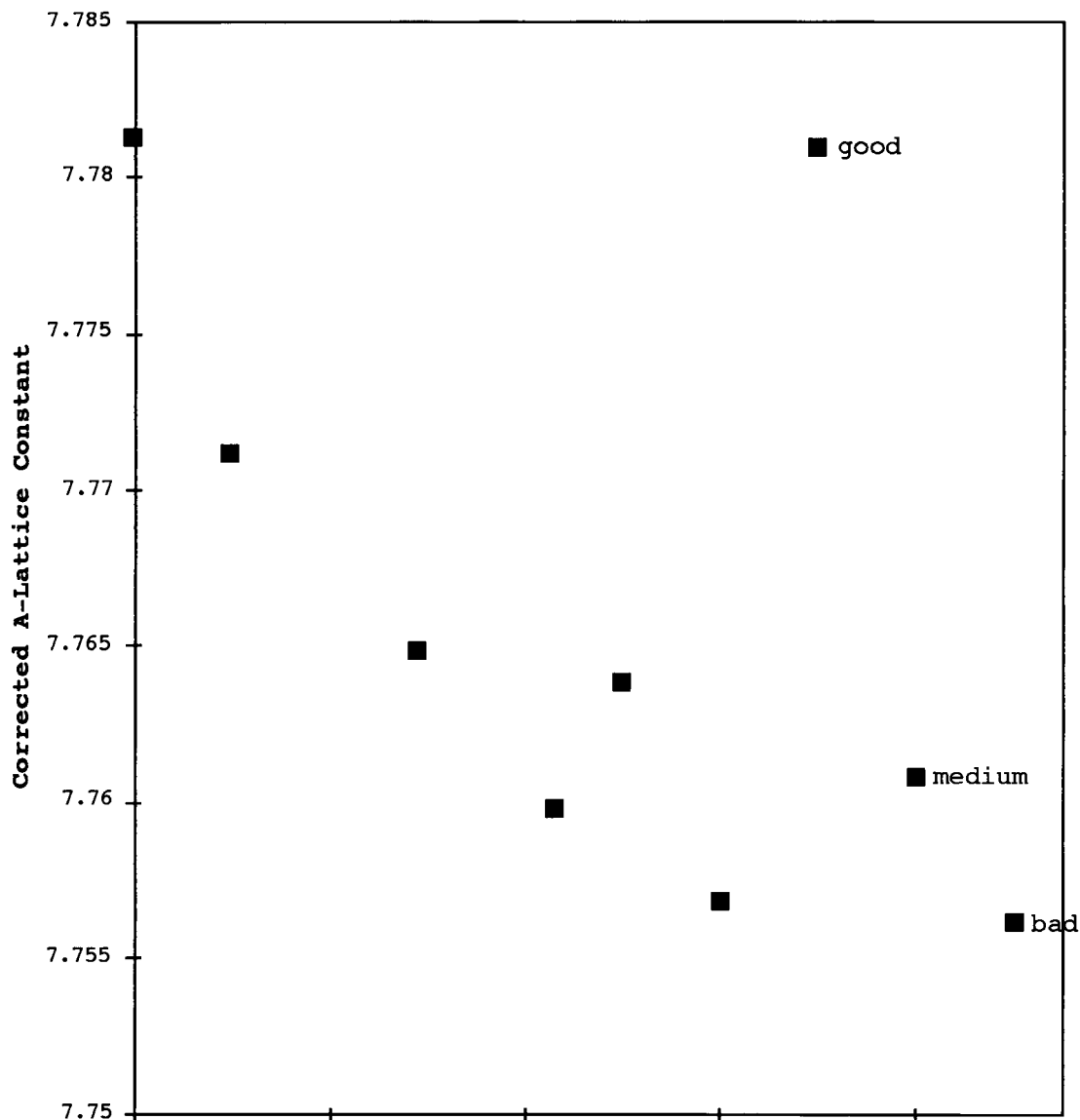


Figure 5.5. The comparison between laboratory reactor samples and actual plant samples of catalysts VPO. A correlation between the lattice constant and the catalyst performance. The larger the lattice constant, the better the catalyst.

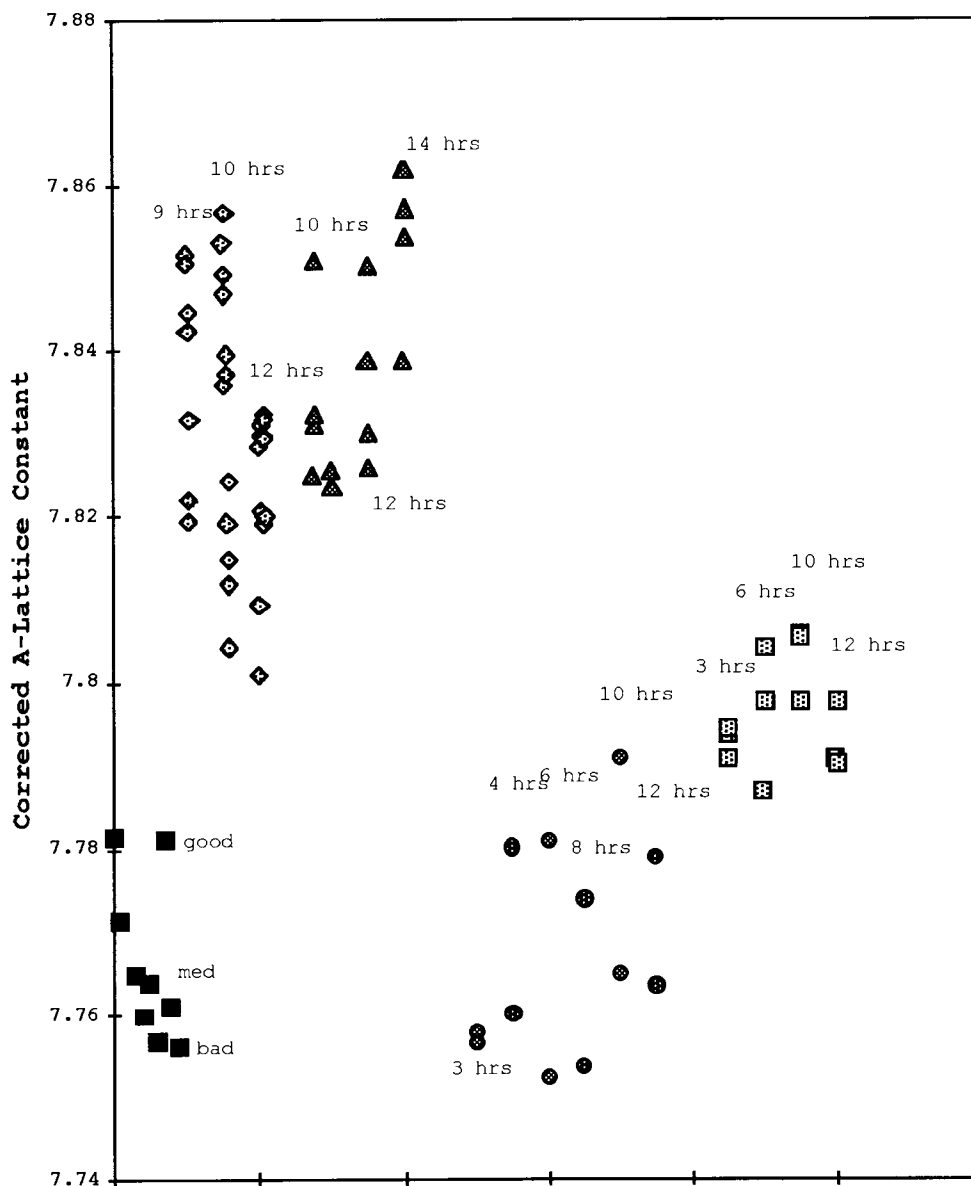


Figure 5.6. Compilation of corrected a-lattice constant data from catalyst supplied by DuPont and samples prepared at OSU. \blacksquare are samples from DuPont, \blacklozenge are samples prepared with 105% H_3PO_4 , \blacktriangle are samples prepared with 117% H_3PO_4 and t-butanol, \bullet are samples prepared with 85% H_3PO_4 and isobutanol, and \square are samples prepared with 85% H_3PO_4 and t-butanol.

seems to undergo first a reduction and then an increase as the time in the reactor increases. The immediate jump at 50 days cannot be explained, but it should be noted that this is where the minimum of the strain and size occurs. This study is greatly complicated by the fact that fine particles are continually being lost from the reactor and fresh catalyst was added to make up for this loss.

Three samples were obtained from DuPont identified as "good", "medium", and "bad" catalysts based on performance in their reactors. These were analyzed for strain effects, and the results are shown with our other results in Figure 5.5. Better catalysts have a smaller a-cell edge, and the cell edge of good catalysts tend to decrease with time in the reactor. The two trends seem compatible because there is some decrease in catalyst performance as the catalyst ages in the large reactor.

Another plot was made with our own samples and is shown in Figure 5.6. The reflux time for a particular set of sample is highlighted on the plot. The difference between each data point for a particular set of samples is the calcination time for the conversion between precursor to catalyst. For all samples, the shorter the calcination time, the larger the a-cell edge. There is a trend observed

similar to samples supplied from DuPont where the lattice constants are decreasing with increasing calcination time. The corrected lattice constant has a range of 0.06\AA for each sample batch except for the samples prepared with 85% H_3PO_4 plus *t*-butanol where the lattice constant ranges from 7.78\AA to 7.81\AA .

Our 85% H_3PO_4 prepared samples were very similar to the day 0 sample from DuPont. However, our 105% and 117% H_3PO_4 prepared samples showed extremely high strain relative to the "good" DuPont catalyst sample. The crystallite sizes of our samples were much lower than those of DuPont's, and the strain was much higher, Table 5.3. This figure suggests that samples from precursors with a high degree of strain result in a very high value for the *a* cell edge. This strain decreases as the catalyst is used and as catalyst performance decreases.

5.4 Conclusion

The data presented in this chapter suggests that in order to obtain the best catalysts, a very high concentration of H_3PO_4 should be used. The reflux time to prepare the

precursor is not significant as long as it is greater than nine hours. This would effectively increase the available active sites as seen by the broadening of the 200 peak in the X-ray diffraction. Also, there is evidence of organic entrapment within the $V_2P_2O_9 \cdot 2H_2O$ precursor, and using a bulky organic solvent like t-butanol helps increase the final catalyst surface area by decreasing precursor particle size. This in effect increases the amount of strain in the samples.

5.5 References

1. D. Beltran-Porter, A. Beltran-Porter, P. Amoros, R. Ibanez, and E. Maritnez, *Eur. J. Solid Inorg. Chem*, **28**, 131-161, (1991)
2. Nakamura, M. Kawai, K, and Fujiwara, Y., *J. Catalysis*, **34**, 345-355, (1974)
3. B.E. Warren, B.L. Averbach, *J. Applied Physics*, **21**, 595 (1950)
4. B.D. Cullity, *Elements of X-ray Diffraction 2nd Ed.*, pp. 285-292, Addison-Wesley Publishing, (1978)

BIBLIOGRAPHY

1. Sleight, *Catal. Today*, **1**, 237-350 (1987)
2. Sleight, *Solid State Chemistry Compounds*, ed. A.K. Cheetham and P. Day, Oxford Univ. Press, 166-181 (1992)
3. Frazer and P.J. Brown, *Physical Review*, **125**, 1283 (1962)
4. Cullity, *Elements of X-ray Diffraction 2nd Ed.*, pp. 285-292, Addison-Wesley Publishing, (1978)
5. B.E. Warren, B.L. Averbach, *J. Applied Physics*, **21**, 595 (1950)
6. Hodnett, *Catal. Rev. Sci. Eng.*, **27**, 373 (1985)
7. Hodnett, Ph. Permanné, and B. Delmon, *Applied Catalysis*, **6**, 231, (1983)
8. B.S. Schiott, K.A. Jorgensen, and R. Hoffmann, *J. Phys. Chem.*, **95**, 2297, (1991)
9. Toradi and J.C. Calabrese, *Inorg. Chem.*, **23**, 1308 (1984)
10. *Chemical and Engineering News*, November 4 1994
11. Cotton and Wilkinson, *Advance Inorganic Chemistry*, 5th Ed., Wiley and Sons Publishing, pp. 677-678, (1988)
12. *Crystallographic Computing 3rd Ed.*, G. M. Sheldrick, C. Kruger, and R. Goddard, Oxford University Press, 1985, pp. 175-189
13. Beltran-Porter, A. Beltran-Porter, P. Amoros, R. Ibanez, and E. Maritnez, *Eur. J. Solid Inorg. Chem*, **28**, 131-161, (1991)
14. Porter, A.B. Porter, P. Amoros, R. Ibanez, and E. Martinez, *Eur. J. Solid State Inorg. Chem.*, **28**, 131, (1991)

15. Ye, A. Satsuma, T. Hattori, and Y. Murakami, *Applied Catalysis*, **69**, L1, (1991)
16. Bordes and P. Courtine, *Journal of Catalysis*, **57**, 236 (1979)
17. Bordes, P. Courtine, and J.W. Johnson, *J. Solid State Chem.*, **55**, 270, (1984)
18. Bordes, Dissertation, Comiegne, France (1979)
19. Grootendorst, R. Pestman, R.M. Koster, and V. Ponec, *Journal of Catalysis*, **148**, 261 (1994)
20. Cavani, F. Trifiro, *Chemtech*, 16-25, April 1984
21. Rouvet, J.M. Herrmann, and J.C. Volta, *J. Chem. Soc. Faraday. Trans.*, **90**, 1441, (1994)
22. Centi, F. Trifiro, J.R. Ebner, V.M. Franchetti, *Chemical Reviews*, **88**, 55-80 (1988)
23. Bergeret, J.P. Broyer, M. David, P. Gallezot, J.C. Volta, and G.J. Hecquet, *Chem. Soc. Chem. Commune*, 825 (1986)
24. Williamson and W.H. Hall, *Acta Metall.*, **1**, 22 (1953)
25. Horowitz, C.M. Blackstone, A.W. Sleight, and G. Teufer, *Applied Catalysis*, **38**, 193 (1988)
26. Matsuura, A. Mori, and M. Yamazaki, *Chemistry Letters*, 1897-1900 (1987)
27. *International Tables for Crystallography*, Vol A, ed. T. Hahn, D.Reidel Publ, Boston, (1983)
28. Treacy, J.M. Newsam, and M.W. Deen, *Proc. R. Soc. Lond. A*, **433**, 499-520 (1991)
29. Ebner and M.R. Thompson, *Studies in Surface Science and Catalysis*, ed. R.K. Grasselli and A.W. Sleight, Elsevier (1992)
30. Johnson, D.C. Johnston, A.J. Jacobson, and J.F. Brody, *J. Am. Chem. Soc.*, **106**, 8123 (1984)

31. Forni, C. Oliva, A.V. Vixhniakov, A.M. Ezerets, I.E. Mukovozov, F.P. Vatti, and V.N. Zukovskaja, *J. Catalysis*, **145**, 194-203, (1994)
32. Cornaglia, C. Caspani, and E.A. Lombardo, *Applied Catalysis*, **74**, 15 (1991)
33. Granados, J.C. Conesa, and M.F. Garcia, *Journal of Catalysis*, **141**, 671 (1993)
34. Nakamura, K. Kawai, Y. Fujiwara, *Journal of Catalysis*, **34**, 345 (1974)
35. Sananes, A. Tuel, G.J. Hutchings, and J.C. Volta, *J. Catalysis*, **148**, 395-398 (1994)
36. Middlemiss, doctoral dissertation, Dept. of Chemistry, McMaster Univer. Hamilton, Ontario, Canada (1978)
37. Walker, and Stuart, *Acta Cryst.*, **A39**, 158-166, (1983)
38. Amoros, R. Ibanez, A. Beltran, D. Beltran, A. Fuertes, P.G. Romero, E. Hernandez, and J.R. Carvajal, *Chem. Mater.*, **3**, 407, (1991)
39. Gai and K. Kourtakis, *Science*, **267**, 661 (1995)
40. Rylander and W.J. Zimmerscheid, U.S. Patent 2,773,921 (1956)
41. Gopal and C. Calvo, *Journal of Solid State Chemistry*, **5**, 432 (1972)
42. Contractor, and A.W. Sleight, *Catal. Today*, **3**, 175-184 (1988)
43. Contractor, H.E. Bergna, H.S. Horowitz, C.M. Blackstone, B. Malone, C.C. Toradi, B. Griffiths, U. Chowdhry, and A.W. Sleight, *Catalysis Today*, **1**, 49 (1987)
44. Contractor, H.E. Bergna, H.S. Horowitz, C.M. Blackstone, U. Chowdhry, and A.W. Sleight, *Catalysis 1987*, Elsevier, 645-654 (1988)

45. Williams and O. Mullins, *NASA Technical Memorandum 58234*, (1981)
46. De Rossi, M.L. Jacono, M. Gardini, and P. Porta, *J Catalysis*, **146**, 126-135 (1994)
47. TEXSAN, Molecular Structure Corporation, The Woodlands, TX, USA, (1988)
48. Rauchfuss, et. Al., *J. Am. Chem. Soc.*, 105, 6321 (1983)
49. Gorbunova and S.A. Linde, *Sov. Phys. Dokl.*, **24**, 138 (1979)